ABSTRACT

MAGNETORESISTANCE IN NON-MAGNETIC SEMIMETALS AND QUANTUM WELLS

Jing Xu, PhD
Department of Physics
Northern Illinois University, 2019
Dr. Zhili Xiao, Director

Magnetic field induced resistance change is conventionally termed as magnetoresistance (MR), which is usually related to magnetism and plays crucial roles in applications such as sensors and storage devices. In a single-band nonmagnetic material, the semiclassical Boltzmann equation approach gives rise to a magnetic field independent resistivity. With the recent discovery of topological materials, extremely large magnetoresistance (XMR) and negative longitudinal magnetoresistance (NLMR) have been observed in a variety of materials. In this dissertation I investigated XMRs in the rare-earth monopnictides (LaSb and YSb), which are non-saturating with increasing magnetic field, accompanying with a turn-on temperature behavior of the magnetoresistivity. I also observed a saturating XMR behavior as well as a reentrant metallic behavior of the magnetoresistivity at low temperatures in a Weyl semimetal (NbP) of Group V transition-metal monophosphides. My results reveal that the XMR behavior originates from ultrahigh mobility of the charge carriers and nearly perfect compensation of the

electron and hole density. This research shows that Hall factor (κ_H) is the experimental parameter to reveal the important role played by Hall Effect in the XMR phenomenon.

This dissertation research also uncovers a negative longitudinal MR behavior in gallium arsenide quantum wells. Microscopic disorder that causes current path distortion in the high-quality quantum wells is proposed to be the origin of the observed NLMRs. A phenomenological three-resistor model is developed to describe the various magnetoresistance behaviors observed in experiments. The results provide an alternative mechanism to explain NLMRs in other materials such as topological single crystals, in which the NLMRs are considered to be associated with Weyl fermions that have a defined chirality.

NORTHERN ILLINOIS UNIVERSITY
DE KALB, ILLINOIS

MAY 2019

MAGNETORESISTANCE IN NON-MAGNETIC SEMIMETALS AND QUANTUM WELLS

BY

JING XU

A DISSERTATION SUBMITTED TO THE GRADUATE SCHOOL

IN PARTIAL FULFILLMENT OF THE REQUIREMENTS

FOR THE DEGREE

DOCTOR OF PHILOSOPHY

DEPARTMENT OF PHYSICS

Doctoral Director:
Zhili Xiao

ACKNOWLEDGEMENTS

I would like to express my heartfelt gratitude to my advisor Prof. Zhili Xiao for accepting me as his graduate student, supporting my work at Northern Illinois University and Argonne National Laboratory, and mentoring me from career planning to lifestyle. His fantastic physical insight and novel ideas on various projects greatly inspired me during my six years of graduate study. I'm also very grateful to my committee members, Prof. Omar Chmaissem and Prof. Yasuo Ito, for taking the time out of their busy schedules to read this dissertation and serve on the dissertation committee.

I also sincerely appreciate Dr. Wai-Kwong Kwok for accepting me to work as a visiting graduate student in his group in the Material Science Division of Argonne Nation Laboratory and for providing me guidance on both experiments and life. I thank Dr. Yonglei Wang for helping me getting familiar with experimental systems in labs and sharing with me his experience in transport measurements and imaging. I also thank Dr. Ralu Divan and Dr. Leonidas Ocola for training and helping me in the operation of various nanofabrication systems. I thank Dr. Young's group in Argonne and Dr. Pfeiffer's group in Princeton University for providing me samples for the experiments. I thank Dr. Laxman Thoutam for teaching me the method to fabricate samples for transport measurements I also want to thank Mr. Justin Woods and Mr. Yangyang Lyu, who later joined Dr. Kwok's group in Argonne, for their assistance in experiments.

I am immensely indebted to my family who supported me in various ways. My dear grandma, who is a retired middle school teacher, brought me up and kept encouraging me to

work hard. My parents gave me so much love and supported me to pursue my dream to be a physicist. My cousin Juhao introduced Northern Illinois University to me and encouraged me to come to study in the United States. My parents-in-law trusted me unconditionally and gave me the opportunity to take care of their daughter - the most important person in their life, and of course, in my life.

Finally, I dedicate this dissertation to my dear wife Zhangdi. Zhangdi has been making me a better person in every aspect. Without her sleeping on the front passenger seat in my car, I would not be a good driver. Without her desire to the delicious spicy food, my friends would not call me ‘the chef’. Her love, her expectation, and her care make me the person who I am now. Life is amazing, the rendezvous in a physics lab six years ago brought the pretty princess to my life, and finally she helped me get my physics Ph.D.

Table of Contents

List of Tables

List of Figures

1. Introduction

Magnetoresistance (MR), i.e., the change in resistance of a material in response to the applied magnetic field [1], lies at the core of various kinds of magnetic field sensors [2,3] including the read heads in the computer hard drive [4]. In pursuit of higher sensitivity in such devices, scientists have made a lot efforts to find materials with large MR [5-23]. On the other hand, studies on the origin of various MR behaviors, including the anisotropic magnetoresistance (AMR) and negative longitudinal magnetoresistance (NLMR) [16,21,22,24-34], have never been stopped in order to achieve better understanding and application of MR phenomena. Classically, the Lorentz force induced by magnetic field will deviate the electrons in a conductor away from the current path, hence increase their scattering probability, resulting in an enhancement in resistance [1]. This type of MR behavior is known as ordinary magnetoresistance (OMR), whose value is usually small. Besides the giant MR (GMR) [4] and colossal MR (CMR) [35] in magnetic thin films and compounds, extremely large MR (XMR) was observed decades ago in nonmagnetic materials such as bismuth [6] and graphite [7,8]. After theoretical prediction of the quantum spin Hall effect [36] , a lot of topological materials have been discovered [37-39], which often accompany with XMR behavior, triggering more intense research in MR phenomena. Exploring the dynamics of charge carriers and constructing the Fermi surface are very important to uncover the underlying mechanism of the XMR behavior, especially in topological semimetals [15-23], the most distinguishable property of which is having the exotic band structures.

Recently, XMRs were observed in rare-earth monopnictides *LnX* (*Ln* = La, Y, Nd, Ce and *X* = Sb, Bi) [40-56] and Group V transition-metal monophosphides (TaAs, TaP, NbAs, and NbP) [18,21,57-59]. Among them, the XMR behavior in rare-earth monopnictides was mostly reported to be non-saturating in a wide range of temperature, while that in transition-metal monophosphides is saturating at liquid helium temperatures. Since those transition-metal monophosphides were reported to be topological materials, i.e., Weyl semimetals, the XMR behaviors in them were widely attributed to the topological protection [40,60-63]. Another important magnetoresistance behavior – the negative longitudinal magnetoresistance (NLMR), was reported to occur in Weyl semimetals, which is consequently regarded as an evidence for the existence of Weyl fermions with the chiral anomaly [16,21,22,24-28,64]. On the other hand, the NLMR was also observed in non-Weyl materials [31,65-67], resulting in debate on the underlying physics for NLMRs.

In this dissertation, I will present results of systematic magnetotransport measurements on crystals of rare-earth monopnictide (LaSb and YSb) and transition-metal monophosphide (NbP) to study the non-saturating XMR behavior and saturating MR behavior as well as high-quality GaAs quantum wells to understand the NLMR phenomenon. For each of those materials, at least two samples were measured. All the reported properties are based on repeatable or consistent experimental data from different samples.

In chapter 1, I will provide a brief introduction of background knowledge about MR behaviors and relevant concepts. Physical concepts on various types of novel MR behaviors, construction of the Fermi surface, and topological materials will be presented.

In chapter 2, experimental methods on crystal growth and electric contacting as well as measurement procedures will be presented.

In chapter 3, I will show my experimental observation of non-saturating XMR behaviors in rare-earth monopnictides LaSb and YSb. Angle- and temperature-dependent magnetotransport measurements were conducted on LaSb crystals, in which I observed turn-on temperature behavior and angle-dependent Shubnikov de-Hass (SdH) oscillations. I revealed a nearly perfect compensation of the electron and hole concentration in the LaSb sample and used it to explain the XMR behavior. I also conducted transport measurements on another member of rare-earth monoponictide family, YSb, in which an uncompensated electron and hole concentration and non-saturating MRs were reported. My analyses on angle-dependent SdH oscillations do reveal a nearly perfect compensation of electron and hole density, consistent with my finding in LaSb. Thus, my results reveal the same origin of XMR in the those two rare-earth monopnictides.

In chapter 4, I will present the saturating XMR behavior in Weyl semimetal NbP. Experimentally, I conducted angle- and temperature-dependent magnetotransport measurements on NbP crystals and observed a saturating MR behavior and a reentrant metallic behavior of resistivity at low temperature region. I also revealed the role played by Hall effect on the origin of the XMRs and the saturating MR behavior by using an experimentally determinable parameter – the Hall factor.

In chapter 5, I will report my observation of NLMR behavior in gallium arsenide quantum wells. I conducted temperature- and angle-dependent magnetotransport measurements on GaAs

quantum wells. NLMRs were observed mainly at the orientation where the magnetic field is in parallel with the current direction. I revealed the role played by microscopic disorder on the NLMR behavior and explained various MR behaviors at different temperatures with a phenomenological three-resistor model. I will also discuss the relation between NLMR behavior and chiral anomaly of Weyl fermion, which has attracted extensive attention in recent years.

1.1. Magnetoresistance

Magnetoresistance is the change in the electrical resistance induced by the magnetic field, which can be expressed as

$$MR = \frac{\Delta\rho}{\rho} = \frac{\rho(H)-\rho(0)}{\rho(0)} \tag{1.1}$$

where $\rho(H)$ and $\rho(0)$ represent the resistivities with and without the magnetic field respectively. In most materials, the MR is positive, which means the resistance usually becomes larger with increasing magnetic field. The Lorentz force induced by the magnetic field drives the charge carriers to deviate from the global current path, which increases the scattering probability for electrons, resulting in an increasing resistance. The magnitude of this type of MR is usually very small, which is called Ordinary Magnetoresistance (OMR) and can be widely observed in conductors.

As mentioned earlier in this chapter, MR phenomenon has been utilized in the fabrication of magnetic field sensors, which lie at the core of computer hard drives. The novel MR behaviors, such as large MRs and negative longitudinal MRs (NLMR) can enhance the sensitivity of these

devices. The discovery of giant MR (GMR) by Albert Fert and Peter Grunberg in the Fe/Cr alloy [68] kicked off the intense race in searching for large MR materials and uncovering the mechanism of such phenomena. Later on, materials with colossal MR (CMR), whose MR values are orders of magnitude larger than those in GMR materials, were discovered. In recent years, extremely large MR (XMR), with even larger MR values than CMR, was found with the discovery of topological materials [15-23].

1.2. Weyl semimetal

Extremely large magnetoresistances (XMR) were observed decades ago in nonmagnetic materials such as bismuth [6] and graphite [7,8]. However, their origin were still under debate. Recently, XMR was discovered in $PtSn_4$ [9], $PdCoO_2$ [10], $NbSb_2$ [11], and WTe_2 [12-14]. More intriguingly, $PtSn_4$ [38] and WTe_2 [39] were found to be topological semimetals, indicating a possible connection of the XMR behavior with the topological surface states.

Insulators have a finite energy gap between the conduction and valence bands, which results in their non-conducting nature. The strong spin-orbital coupling (SOC) in a topological insulator (TI) [37,69,70] inverses bulk band structure and results in metallic surface states. That is, TIs have gapless surface states along with energy gaps in the bulk band structures. The spin and moment in the surface states are locked-up and a Dirac core [70,71] forms in the surface band structure (see Figure 1.1), which was previously observed in few materials such as graphene [72] and bismuth [73].

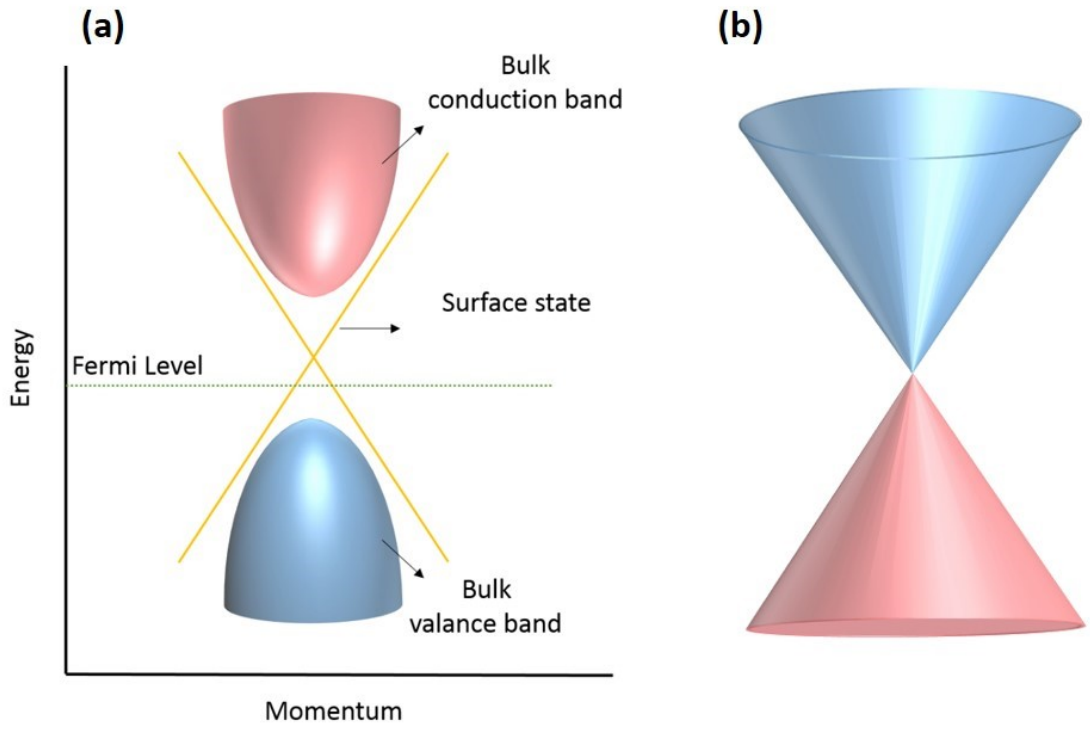

Figure 1.1 | Band structure of a topological insulator. (a) Band crossing on the surface state form a Dirac cone. (b) Schematic of linear crossing of at Dirac cone.

In some exotic semimetals, topological surface states (TSSs) are very similar to those in TIs can exist. Such materials were known as Weyl semimetals [74]. Hermann Weyl solved Dirac equation with a massless spin ½ particle, named Weyl Fermion [75]. Materials with such massless fermion had not been found for many years until some recent reports of the Weyl semimetal [21,76,77]. In Weyl semimetals, gaps lie between the bulk bands in 3D momentum space due to SOC, with linear crossings only at some points that are called Weyl points. Consequently, Weyl semimetals are regarded as spin-polarized '3D graphene' [78].

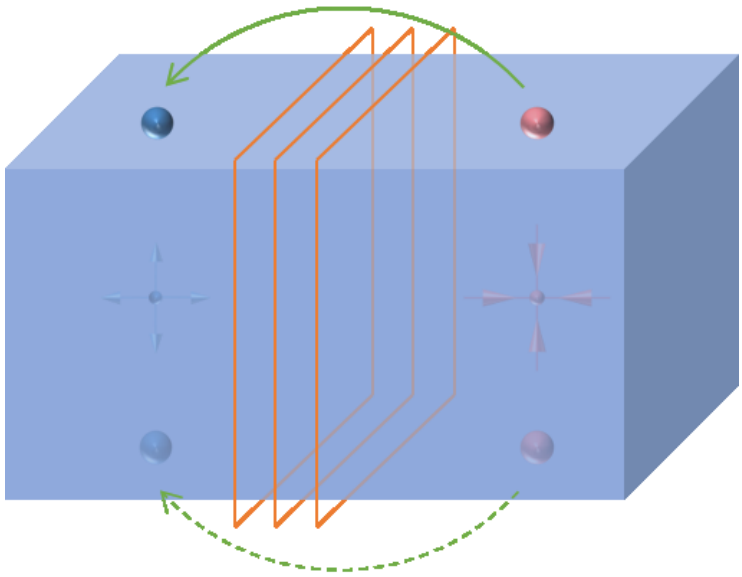

Figure 1.2 | Fermi arcs form on the topological surface state of the Weyl semimetals. A pair of Weyl points with inversed chirality is shown with blue and red color.

Similar to that of in TIs, the bulk band structure of a Weyl semimetal is also reversed, as the surface states appear with Fermi arcs in the band structure, see Figure 1.2. The Weyl points have either positive or negative chirality, and are usually appeared in pairs, acting as monopoles with fixed chirality in the momentum space of a Weyl semimetal [79]. A Weyl semimetal requires the breaking of time-reversal symmetry or inversion symmetry or both of them [77,79].

Exotic magnetotransport behavior, including XMR [18,21] and NLMR [16,21,22,24-28,64] were observed in Weyl semimetals. The origin of such phenomenon was under debate, but has been widely attributed to topological properties such as the chiral anomaly or the Berry curvature

of the band. On the other hand, my experimental results, derived from both Weyl and non-Weyl materials, indicate that the MR behaviors can be explained with a semi-classic transport theory without involving topological protection.

1.3. Fermi surface mapping

To understand the novel MR behaviors, either using a semi-classical transport theory or from the topological aspect, the Fermi surface is always one of the key factors. There are multiple methods to map out the Fermi surface. First principle calculations are the most widely used one to theoretically simulate the shape of the Fermi surface. It is a powerful and convenient tool to help experimental scientists getting a general idea about the band structure of certain materials. Experimentally, angle-resolved photoemission spectroscopy (ARPES) and quantum oscillations can be used to determine the Fermi surface.

1.3.1. Angle-resolved photoemission spectroscopy

The ARPES measurement is based on the famous photo-electric effect, which is experimentally and theoretically found by Hertz and Einstein. The electrons in certain material can absorb the photon energy of the incident light, which is larger than its work function, forming photoelectrons that escape into the vacuum (see Figure 1.3). By collecting the escaped photoelectrons and analyzing their kinetic energy and momentum, the band structure can be extracted. This process can be expressed as

$$E_k = h\nu - E_B - \phi \tag{1.2}$$

where E_k is the kinetic energy of the photoelectron, E_B is the binding energy of the electron, ν is the frequency of indicating light and ϕ is the work function representing the energy required to remove the electron from the sample to the vacuum.

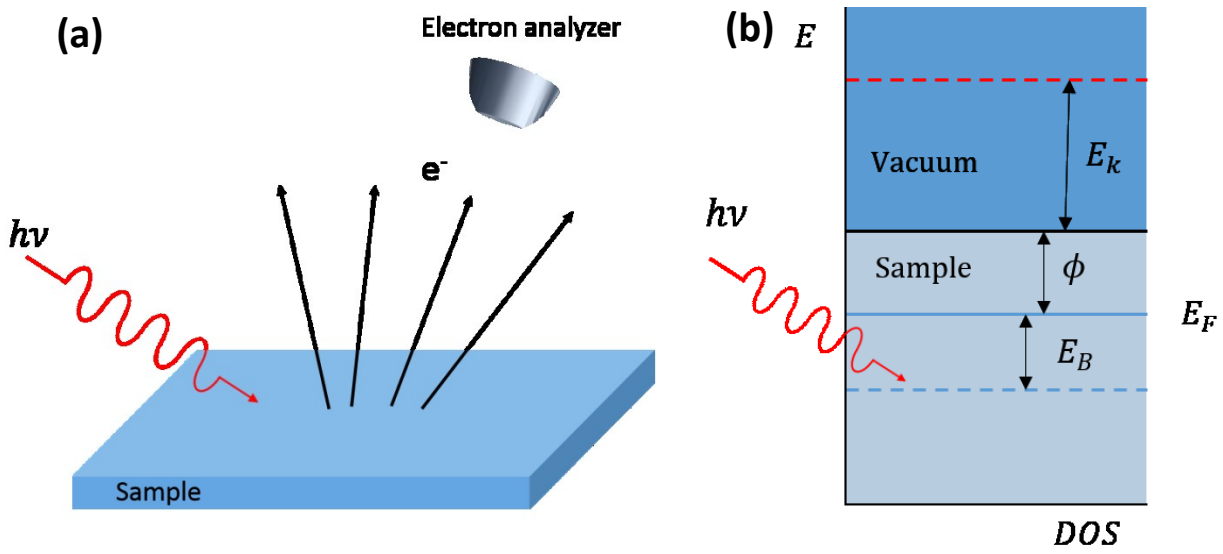

Figure 1.3 | Schematic of ARPES experiment. (a) electron analyzer receive the emitted photoelectron by photoelectric effect. (b) Energy diagram of the photoelectric process. E_k is the kinetic energy of the photoelectron, E_B is the binding energy of the electron, E_F is the Fermi level of the sample, ν is the frequency of indicating light and ϕ is the work function.

1.3.2. Quantum oscillation

Orbit quantization is given by Landau, to describe a charged particle in the magnetic field, as

$$\varepsilon_n = \hbar\omega_c(n + \tfrac{1}{2}) \tag{1.3}$$

where $\omega_c = \frac{eH}{m^*c}$ is the cyclotron frequency. The quantized energy level in magnetic field, as shown in Figure 1.4, has a tubular shape, which is called the Landau tube. With various energy levels, the extremal area between the Landau tubes and the Fermi surface will change. At low temperature and high magnetic fields, the quantum limit of a high quality semimetal will be reached where $\hbar\omega_c > k_B T$.

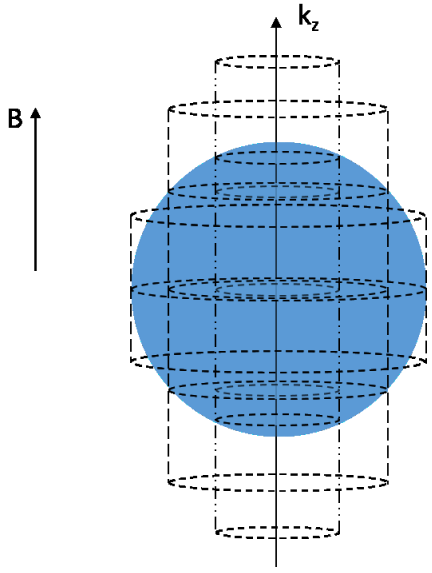

Figure 1.4 | Schematic of Landau tubes in the magnetic field direction.

With the increasing magnetic fields, the higher Landau levels become deoccupied and the electrons in these levels jump into lower levels. In result, the level density has a sharp peak whenever ε is equal to the energy of extremal orbit [80], as shown in Figure 1.5. This mechanism leads to an oscillation of most electronic properties with the change of the magnetic field. Onsager provided a remarkable simple relation of the oscillation phenomenon as

$$\Delta(\frac{1}{H}) = \frac{2\pi e}{\hbar c}\frac{1}{A_e} \tag{1.4}$$

where A_e is any extremal cross-sectional area of the Fermi surface in a plane normal to the magnetic field.

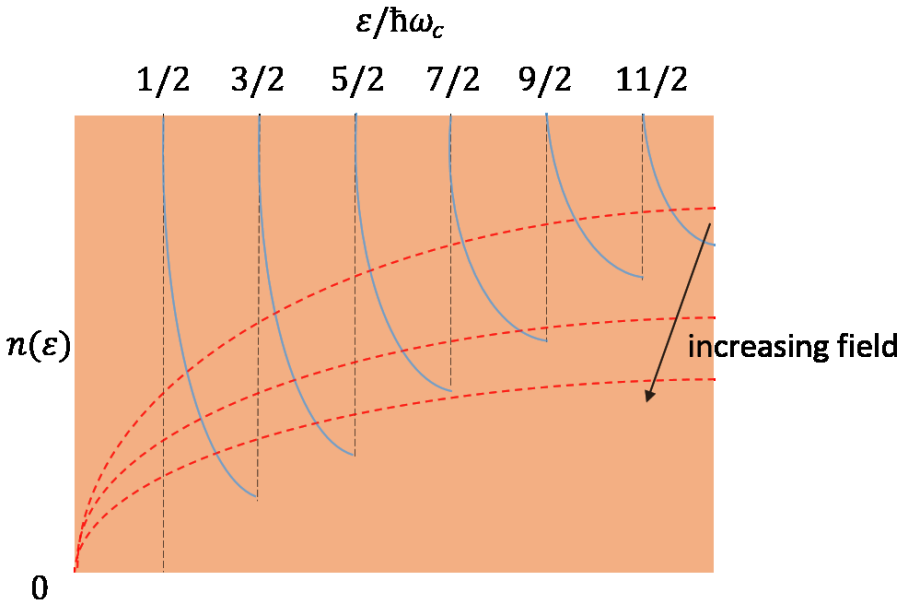

Figure 1.5 | Schematic of the energy levels and density of states.

Experimentally, the angle dependent Shubnikov-de Haas (SdH) and de Haas-van Alphen (dHvA) oscillations, based on the oscillation of resistivity and magnetization, are widely used to determine the Fermi surface. With changing angles between the sample and the external magnetic field, different extremal areas of the Fermi pocket can be probed out (see Figure 1.6).

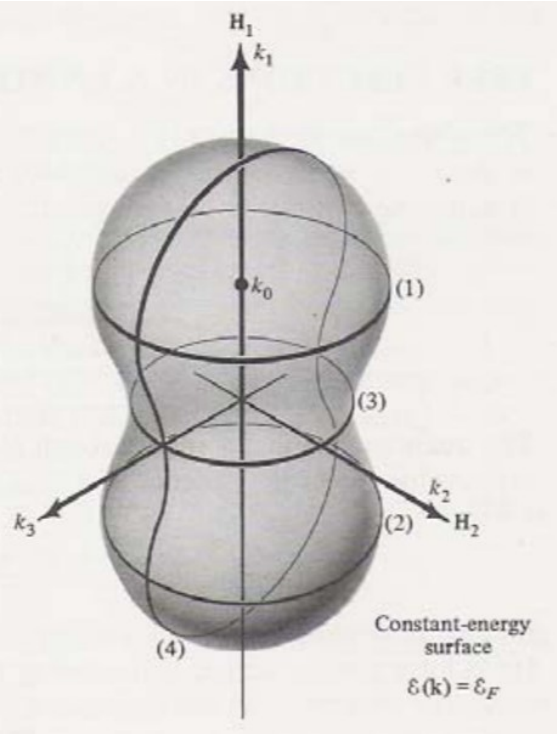

Figure 1.6 | Schematic of a Fermi pocket and the extremal cross-sections. Examples with different orientations of external magnetic field (taken from [80]).

2. Experimental Methodology

2.1. Sample preparation and characterization

LaSb samples. Single crystals of LaSb were grown in tin flux following the procedures in [41]. La powder (Alfa Aesar, 99.9%), Sb spheres (Alfa Aesar, 99.999%), and Sn pieces (Alfa Aesar, 99.999%) were loaded into an aluminum oxide crucible in a molar ratio of 1.5:1:20. The crucible with its top covered by a stainless steel sieve was then sealed in an evacuated silica ampoule. The sealed ampoule was heated to 1050 °C over 10 hours, homogenized at 1050 °C for 12 hours and then cooled to 700 °C at the rate of 2 °C per hour. Once the furnace reached 700 °C, the tin flux was removed from the crystals using a centrifuge. Well-faceted crystals were collected on the stainless steel sieve. The crystal structure of the compound was verified by single crystal x-ray diffraction at room temperature using a STOE IPDS 2T diffractometer using Mo Kα radiation (λ = 0.71073 Å) and operating at 50 kV and 40 mA. The structure was solved by direct methods and refined by full-matrix least squares on F^2 using the SHELXTL program package [53].

The dimensions of the crystals are 223.33 μm (*w*) × 138.78 μm (*d*) × 790 μm (*l*) and 273.37 μm (*w*) × 218.93 μm (*d*) × 600 μm (*l*) for samples A and B, respectively. The electric contacts were made by attaching 50 μm diameter gold wires using silver epoxy, followed with baking at 120 °C for 20 minutes. In order to avoid sample degradation, the contacting operation was carried out in a glovebox filled with inert Ar gas.

YSb samples. Single crystals of YSb were grown in Sb self flux. Y and Sb pieces were loaded in a 2 ml aluminum oxide crucible in a molar ratio of 1 : 15. The crucible was then sealed in a fused silica ampule under vacuum. The sealed ampoule was heated to 1175 °C over 10 h, homogenized at 1175 °C for 12 h and then cooled to 800 °C at the rate of 2 °C/h. Once the furnace reached 800 °C, the excessive flux was decanted from the crystals using a centrifuge.

I measured two YSb crystals with the dimensions of 473.6 μm (*w*) × 85 μm (*d*) × 493.5 μm (*l*) and 950 μm (*w*) × 180 μm (*d*) × 982.5 μm (*l*) for samples I and II, respectively.

NbP samples. High-quality single crystals of NbP were grown via a chemical vapor transport reaction using iodine as a transport agent, following the procedure outlined in [18]. Initially, a polycrystalline powder of NbP was synthesized by a direct reaction of niobium and red phosphorus kept in an evacuated fused silica tube for 48 h at 800 °C. Starting from this microcrystalline powder, single crystals of NbP were synthesized by chemical vapor transport in a temperature gradient starting from 850 °C (source) to 950 °C (sink) and a transport agent with a concentration of 13.5 mg cm^{-3} iodine.

GaAs quantum well samples. The measured samples were 40-nm wide GaAs quantum well grown by molecular beam epitaxy. They were fabricated by Dr. Pfeiffer's group using the same method as ref [81]. The quantum well was buried 180 nm deep under the surface, and separated by 150 nm $Al_{0.24}Ga_{0.76}As$ thick barriers on both sides from the δ-doped silicon impurities with densities of 1.18×10^{12} cm^{-2} and 3.92×10^{12} cm^{-2} for the layers under and above the quantum well, respectively. The samples were fabricated into Hall bars with width of L_y = 50 μm and voltage

lead distance of L_x = 100 μm using photolithography. Contacts to the quantum well were made by annealing InSn at 420 °C for 4 minutes. The electron densities of the measured quantum wells at 3 K range from 7.91 to 8.83 (10^{10}cm^{-2}) (see Table 5.1).

2.2. Resistivity measurements

I conducted DC resistivity measurements on our samples in a Quantum Design PPMS-9 using constant current mode. Angular dependence of the resistance was obtained by placing the sample on a precision, stepper-controlled rotator with an angular resolution of 0.05°.

When I measured the LaSb, YSb, and NbP crystals, the magnetic field $H(\theta)$ was rotated in the (100) plane and the current I flowed along the [100] direction(as shown in Figure 2.1a, such that the magnetic field was always perpendicular to the applied current I (4mA was applied for measuring crystals).

In the measurement of the gallium arsenide quantum wells, the geometry was showed in the Figure 2.1b where the angle θ between the magnetic field B and the current I can be varied. The measurement results were found to be current-independent (as shown in Figure 2.2), and the reported data were taken with I = 0.5 μA for all samples. Figure 2.3 shows the experimental determination of θ = 0°, i.e. the orientation of magnetic field at B//I. In the experiments I measured $R(H)$ curves at various fixed temperatures and angles.

The resistivity versus temperature $\rho(T)$ curves at various magnetic fields were constructed by measuring $\rho(H)$ at various fixed temperatures. The magnetoresistance is defined as $MR = [R(H) - R_0)]/R_0$ where $R(H)$ and R_0 are the resistance at a fixed temperature with and without the presence of a magnetic field, respectively.

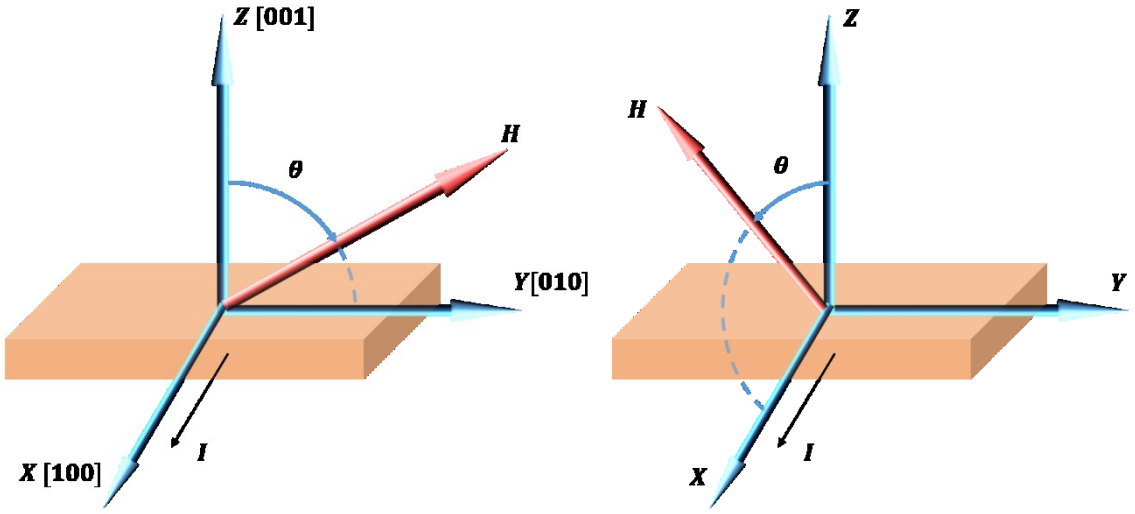

Figure 2.1 | Geometry of transport measurements. a. Magnetic field is rotated in the Y-Z plane and always be perpendicular with current direction. b. Magnetic field is rotated in the X-Z plane, the angle between the current and the magnetic field can be changed.

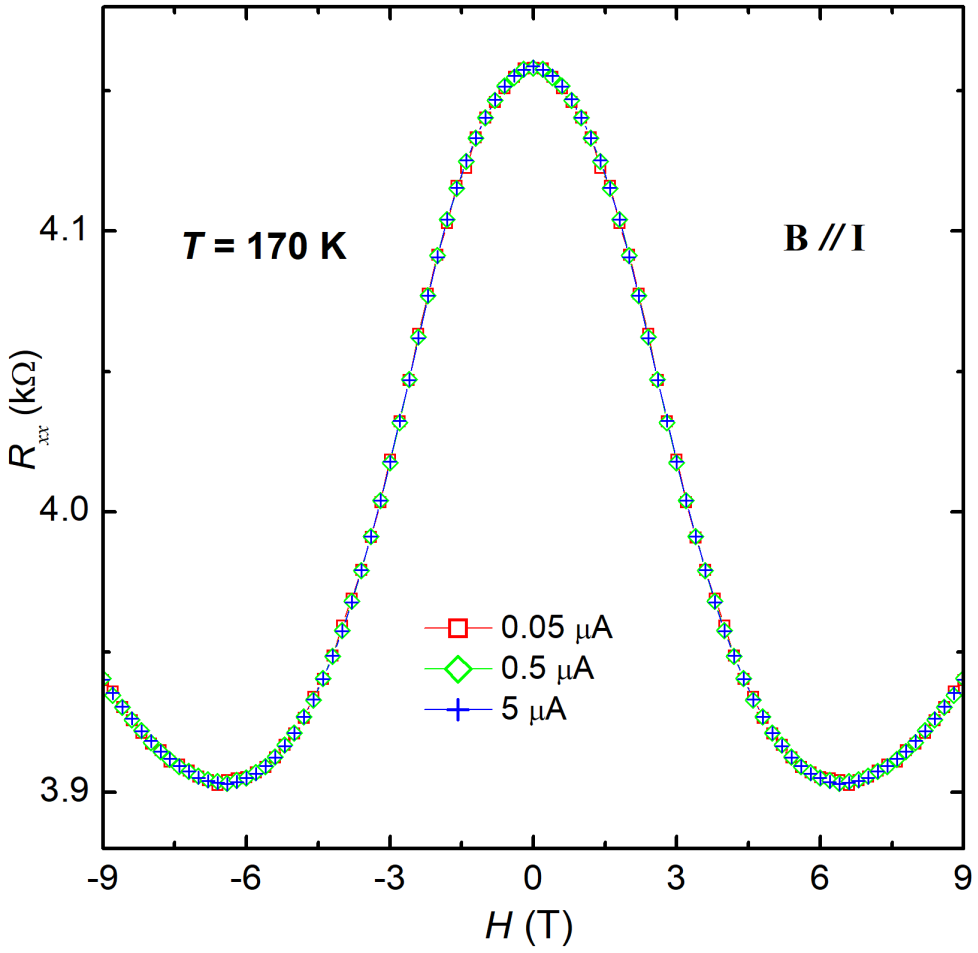

Figure 2.2 | Current independence of the NLMR in a quantum well sample. Data were taken at $T = 170$ K.

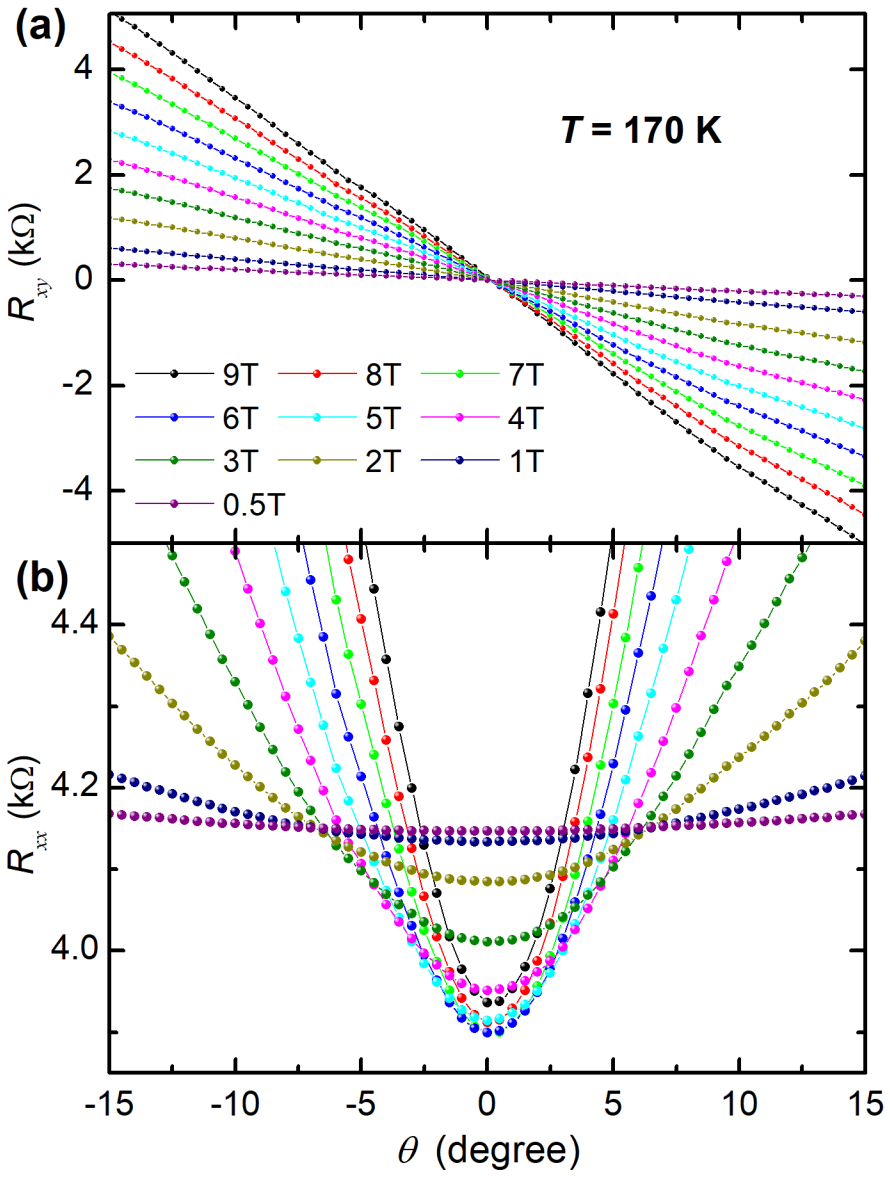

Figure 2.3 | Experimental determination of $\theta = 0°$. At $H//I$, R_{xy} is expected to be 0 and R_{xx} should be at minimum. To determine this orientation, I measured the angle dependence of (**a**) R_{xy} and (**b**) R_{xx} at various magnetic fields.

3. Non-Saturating XMR In Rare-Earth Monopnictides

3.1. Rare-earth monopnictides

Recently, the rare-earth monopnictides LnX (Ln = La/Y and X = Sb/Bi) [40-56] were added to the family of XMR materials. These materials have a rock-salt cubic crystal lattice, as shown in the Figure 3.1(a). Thus their electronic structures are identical along the k_x, k_y and k_z directions of the Brillouin zone. The bulk electronic band structure and Fermi surface of rare-earth monopnictides LnX were investigated more than three decades ago [82-84] and also reported in recent publications [40,41,49]. The bulk FS consists of electron pockets centered at *X* and elongated along the *Γ*–*X* direction in addition to two hole pockets centered at *Γ* [40,43,50]. As revealed by ARPES [53], the Fermi surface structure of LaSb has three (α, β and γ) bands. The electron band, α, has three orthogonally arranged ellipsoidal Fermi pockets ($\alpha_1, \alpha_2,$ and α_3) while the hole bands β and γ Fermi pockets are nearly spherical.

I conducted magnetoresistance measurements to rare-earth monopnictides LaSb and YSb crystals and observed XMR in both materials. Since some rare-earth monopnictides were predicted to be topological insulators, the origin of XMR was attributed to surface states. Previous magnetotransport and ARPES experiments on rare-earth monopnictides also raised a possible role of surface states in observed XMR. I will address the surface verses bulk contribution issue in the magnetoresistance of the LaSb crystals I measured. I will demonstrate that the resistivity plateau at low temperatures, which was considered a signature of surface

states [41], can be explained as a natural consequence of the Kohler's rule scaling [85]. I will show that the Fermi surfaces derived from our Shubnikov–de Haas (SdH) quantum oscillation measurements are in fact bulk Fermi pockets instead of surface ones. Furthermore, these materials have ellipsoidal electron Fermi pockets elongated along the $\Gamma - X$ direction [40,41,43], which can result in an angle-dependent magnetoresistance [43,44,51,52] due to the anisotropic effective mass that governs the mobility of the charge carriers. Hence a quantitative analysis of the angle dependence of the magnetoresistance enables me to reveal the role of each Fermi pocket on the XMR. I demonstrate here that all Fermi pockets play important roles in the observed XMR and electron-hole (*e*-*h*) compensation is a key factor of XMR.

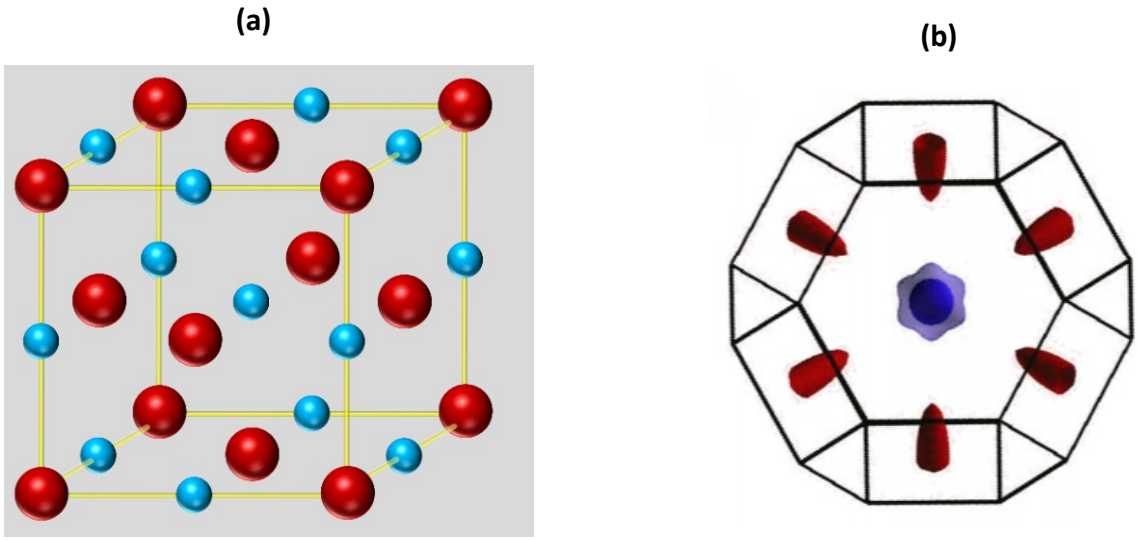

Figure 3.1 | Crystal and Fermi pockets structure of rare-earth monopnictides LnX. (a) Crystal structure. (b) The calculated Fermi pockets.

On the other hand, previous APRES experiments on another rare-earth monopnicide YSb indicated that this XMR material has a ratio of 0.81 for the electron-hole concentration [53]. According to the semiclassical two-band model, however, such a large imbalance in the charge carriers' densities should have resulted in a saturating MR behavior. In order to get a better understanding on the mechanism of XMR in YSb, I measured angle-dependent Shubnikov–de Haas (SdH) oscillation of YSb crystals to determine the shape and volume of the Fermi surface. Like in ARPES, our measurements show anisotropic electron pockets and nearly isotropic hole pockets. However, in contrast to the ARPES results, our quantum oscillations data suggest a nearly perfect compensation of the electron-hole densities with a ratio $n_e/n_h \approx 0.95$ in YSb. More importantly, I will show that a semiclassical theory can quantitatively describe both the transverse MR and Hall resistance when contributions from both the anisotropic (electron) and isotropic (hole) Fermi pockets are included.

3.2. Surface and bulk transport

3.2.1. Kohler's rule scaling

A signature of the XMR phenomenon is the so-called turn-on temperature behavior: When the applied magnetic field is above a certain value, the resistivity versus temperature $\rho(T)$ curve shows a minimum at a field-dependent temperature T_m. For $T > T_m$, it has a metallic temperature dependence similar to that in zero field while becoming insulator-like at $T < T_m$. As presented in Figure 3.2, the magnetoresistance of LaSb crystals displays the same temperature behavior: The $\rho(T)$ curve obtained at $\mu_0 H = 1$ T or higher shows a dip at a field-dependent temperature. At

very low temperatures ($T < 15$ K) the resistivity begins to saturate, forming a plateau in the $\rho(T)$ curve, as clearly shown in Figure 3.2 where the resistivity is plotted in a logarithmic scale.

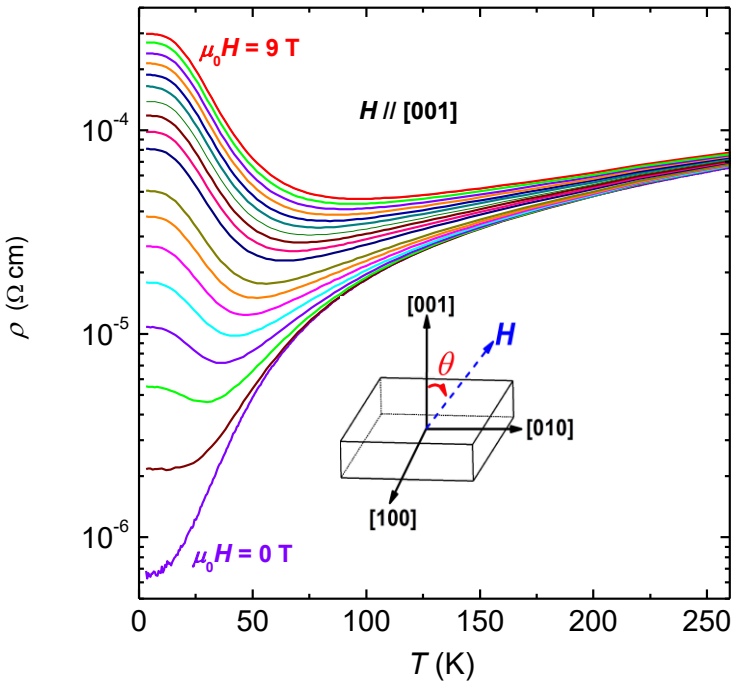

Figure 3.2 | Temperature dependence of the resistivity $\rho(T)$ of LaSb sample. Magnetic fields change from $H = 0$ T to $H = 9$ T at intervals of 0.5 T. Inset: schematic showing the definition of the angle θ for the magnetic field orientation. The magnetic field is rotated in the (100) plane while the current flows in the [100] direction, i.e. they are always perpendicular to each other.

Since magnetic-field-induced metal to insulator transition (MIT) has been considered as a possible origin for the XMR in graphite [86], Tafti et al. [41] attributed the turn-on temperature

behavior in LaSb to a MIT. This MIT interpretation was adopted by other groups to account for the XMR in both rare-earth monopnictide [50] and other materials, including $NbAs_2$, $TaAs_2$, $TaSb_2$, and ZrSiS [87-89]. Below I use Kohler's rule scaling approach, which was successfully employed in WTe_2 by Wang et al. [90], to reveal the origin for both the turn-on temperature behavior and the resistivity plateau.

According to Wang et al., $\rho(T)$ curves obtained for different magnetic fields follow Kohler's rule scaling $\mathrm{MR} = c(\mathrm{H}/\rho_0)^m$, where c and m are sample-dependent constants. I found that Kohler's rule scaling can account for the $\rho(T)$ relationship in LaSb, with $c = 2.5 \times 10^{-10}$ ($\Omega\mathrm{cm/T}$) and $m = 1.71$, as shown in Figure 3.3. I can also rewrite the Kohler's rule scaling as [85]

$$\rho(\mathrm{T},\mathrm{H}) = \rho_0 + c\mathrm{H}^m/\rho_0^{m-1} \tag{3.1}$$

The second term is the magnetic-field-induced resistivity $\Delta\rho$. That is, the resistivity of a sample in a magnetic field consists of two components, ρ_0 and $\Delta\rho$. Since $\Delta\rho \sim 1/\rho_0^{m-1}$, it has a temperature dependence opposite to that of the first term, ρ_0. The competition of ρ_0 and $\Delta\rho$ with changing temperature results in a possible minimum at T_m in the total resistivity $\rho(T,H)$

Figure 3.4 showcases how Eq. (3.1) can lead to the observed turn-on temperature behavior, where the resistivity at $\mu_0 H = 0$ T and $\mu_0 H = 9$ T as well as its difference $\Delta\rho = \rho(T, 9\mathrm{T}) - \rho_0$ are presented.

As demonstrated by Wang et al. [90] for WTe_2, one can conveniently use Kohler's rule scaling to elucidate other turn-on temperature behavior related features such as the magnetic-field dependence of T_m and the temperature dependence of the resistivity minima (ρ_m). Here, I show that Kohler's rule scaling can also describe the resistivity plateau, whose origin was previously considered within a two-band model by Guo et al. [42] and Sun et al. [45]. As presented in Figure 3.3, the experimental data at $\mu_0 H = 9$ T, including the resistivity plateau, can be fitted well by Eq. (3.1) with derived values of *c* and *m* from Kohler's scaling and the experimentally obtained ρ_0. Since ρ_0 is the only temperature-dependent variable in Eq. (3.1), the nearly perfect fits in Figure 3.3 indicate that the resistivity plateau originates from the temperature dependence of ρ_0. Following Eq. (3.1), at low temperatures $\Delta\rho >> \rho_0$; thus $\rho(\mathrm{T,H}) \approx \Delta\rho \sim 1/\rho_0^{m-1}$. Since ρ_0 is insensitive to temperature in the low-temperature regime, a plateau is expected in the total resistivity. Hence the resistivity plateau at high magnetic fields originates from the temperature-insensitive resistivity at the zero field. Since both the resistivity plateau and the turn-on temperature behavior can be derived using the same Kohler's rule scaling, they should represent behavior originating from the same region of the crystal, i.e., either the bulk or the surface states. This excludes the possibility that the turn-on behavior and the resistivity plateau [40,41] separately arise from the bulk and surface states of the crystal, respectively. Thus I can confidently conclude that the resistivity plateau in LaSb at low temperatures is a bulk property only.

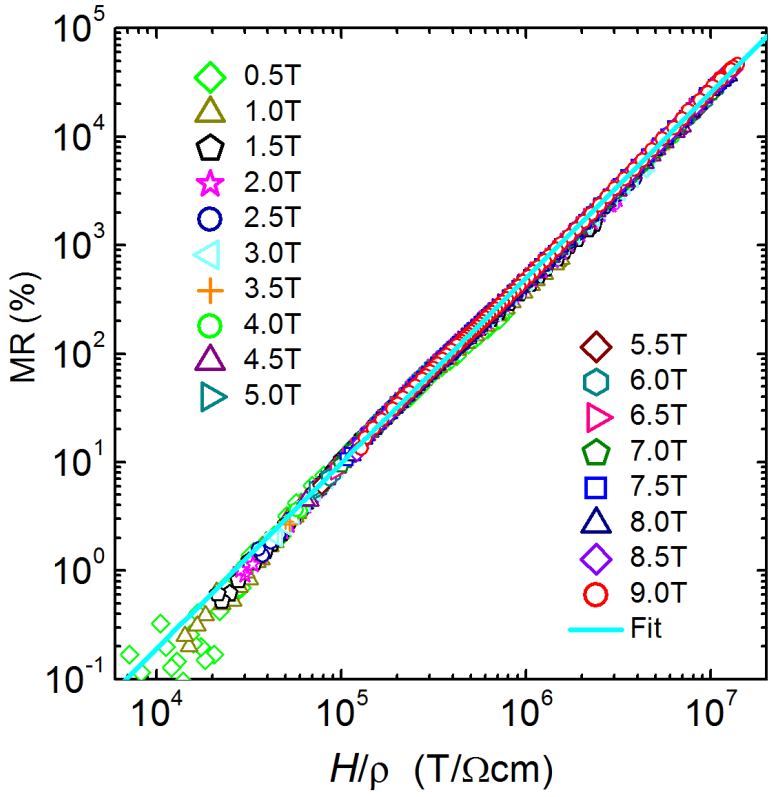

Figure 3.3 | Kohler's rule scaling of resistivity. The solid line represents the fit of $MR = c(H/\rho_0)^m$, to the $\rho(T)$ curves in Figure 3.2, with $c = 2.5 \times 10^{-10}$ $(\Omega\text{cm/T})^{1.71}$ and $m = 1.71$.

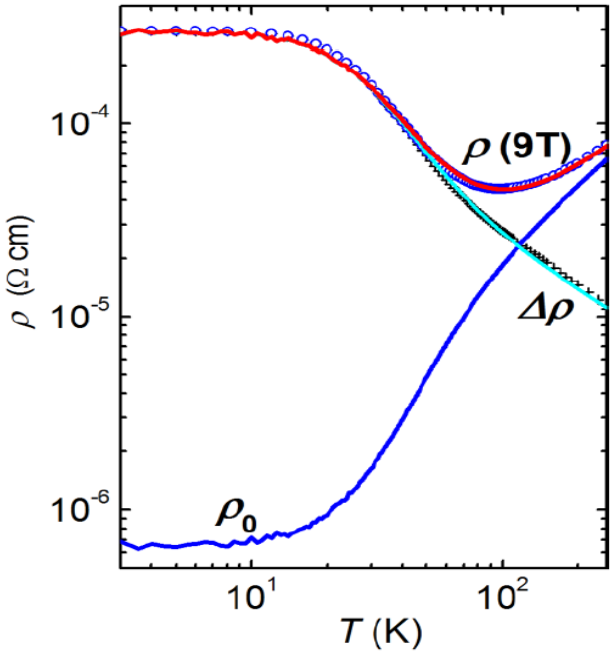

Figure 3.4 | Temperature dependence of the resistivity. $\mu_0 H = 0$ T, $\mu_0 H = 9$ T and their differences. The solid lines are fits to Eq. (3.1) with $c = 2.5 \times 10^{-10}$ [Ω cm/T] and $m = 1.71$.

3.2.2. Shubnikov-de Haas oscillation

Although theory predicts that the rare-earth monopnictides can be topological insulators or semimetals [91], ARPES experiments from various groups have reached differing conclusions: multiple Dirac-like surface states near the Fermi level were observed in LaSb [46] and LaBi [46,47] and their odd number suggests these are topological materials, with Niu et al. [46] concluding that the surface and near-surface bulk bands likely contribute strongly to the XMR in

these two materials. However, Wu et al. [48] found that the dispersion of the surface states resembles a Dirac cone with a linear dispersion for the upper band, separated by an energy gap from the lower band that follows roughly a parabolic dispersion instead. On the other hand, other ARPES results reveal that both LaSb [49] and YSb [53] are topologically trivial, as they did not observe surface states, with a bulk band structure consistent with band theory. For a topological material, its surfaces could be very conductive, and its electrical conductance could come from both the bulk and the surface states.

I conducted both angle-dependent SdH oscillations measurements and first-principles calculations on LaSb. In previous SdH oscillation experiments on LaSb [40,41] and LaBi [43], the current flowed in the rotation plane of the magnetic field. Such a configuration may lead to ambiguity in determining the oscillation feature when the field direction is near or parallel to that of the current, where the Lorentz force is weak or diminishes. To mitigate this effect, in this experiments the current flow is perpendicular to the field rotation plane as shown by the schematic in the inset of Figure 3.2, hence the Lorentz force and the orbital magnetic field remain unchanged under varying magnetic-field orientation [54].

Figure 3.5 shows a typical $\rho(H)$ curve at a low temperature (T = 2.5 K) and at a specific magnetic-field orientation (θ = 121°). SdH oscillations can be seen at high fields. The inset of Figure 3.5 shows the oscillations after subtracting a smooth background from the $\rho(H)$ curve. The amplitude of the oscillations does not decrease monotonically with decreasing field as demonstrated in Figure 3.5. Instead, the observed beating behavior indicates that the oscillations contain more than one frequencies.

If the oscillations originated from the surface states, I would expect to see up to two frequencies in case the side surfaces of the crystal do not have exactly the same states as those of the top/bottom surfaces. However, the fast Fourier transform (FFT) analysis shown in Figure 3.6 reveals more than two frequencies. Furthermore, FFT results presented in Figure 3.7 over a wide range of field orientations show more frequencies than those that can be described by the angle dependence of the SdH oscillation frequency of 2D Fermi surfaces, $F \sim 1/\cos(\theta - n\pi/2)$ [40,41,43]. Thus I need to include the contributions from the bulk.

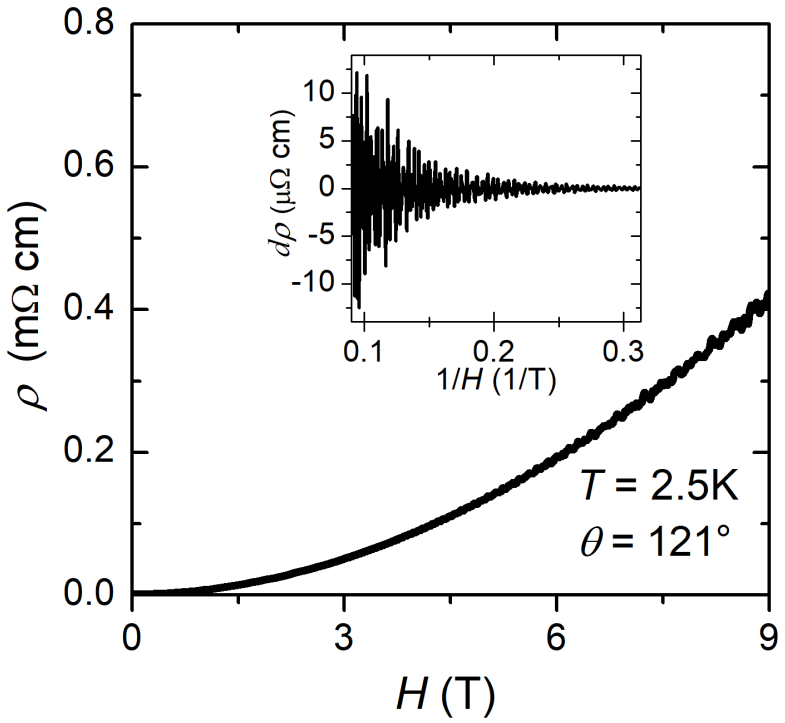

Figure 3.5 | A typical resistivity versus magnetic field curve. Data for sample A at T=2.5 K, which shows SdH oscillations at high magnetic fields. The inset is the oscillatory component after subtracting a smooth background.

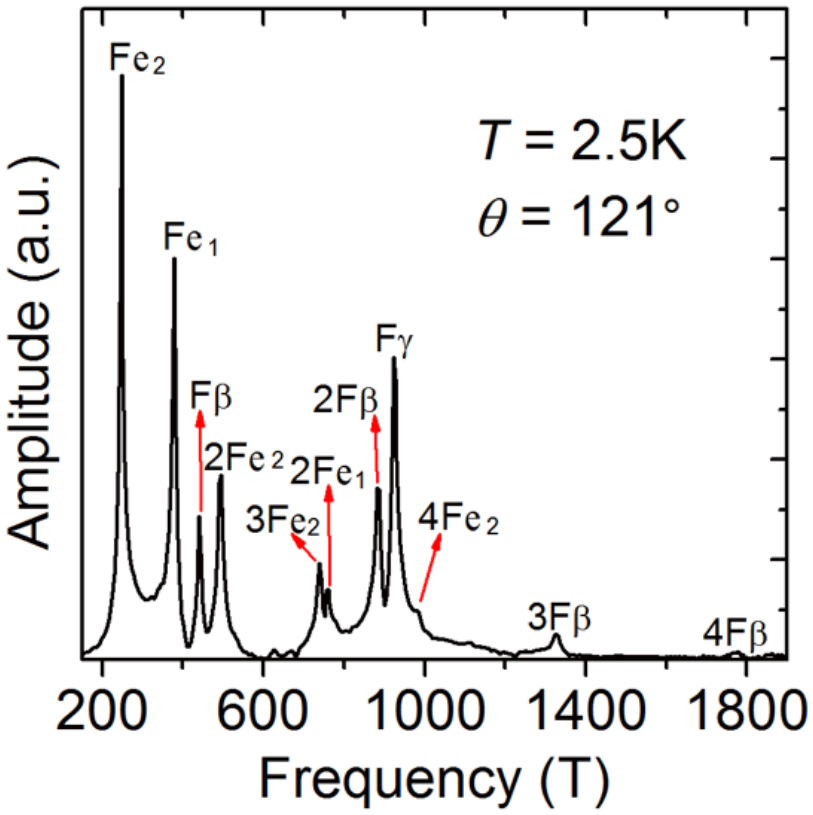

Figure 3.6 | Fast Fourier transform (FFT) analysis of the SdH oscillation. The original data were shown in the inset of Figure 3.5.

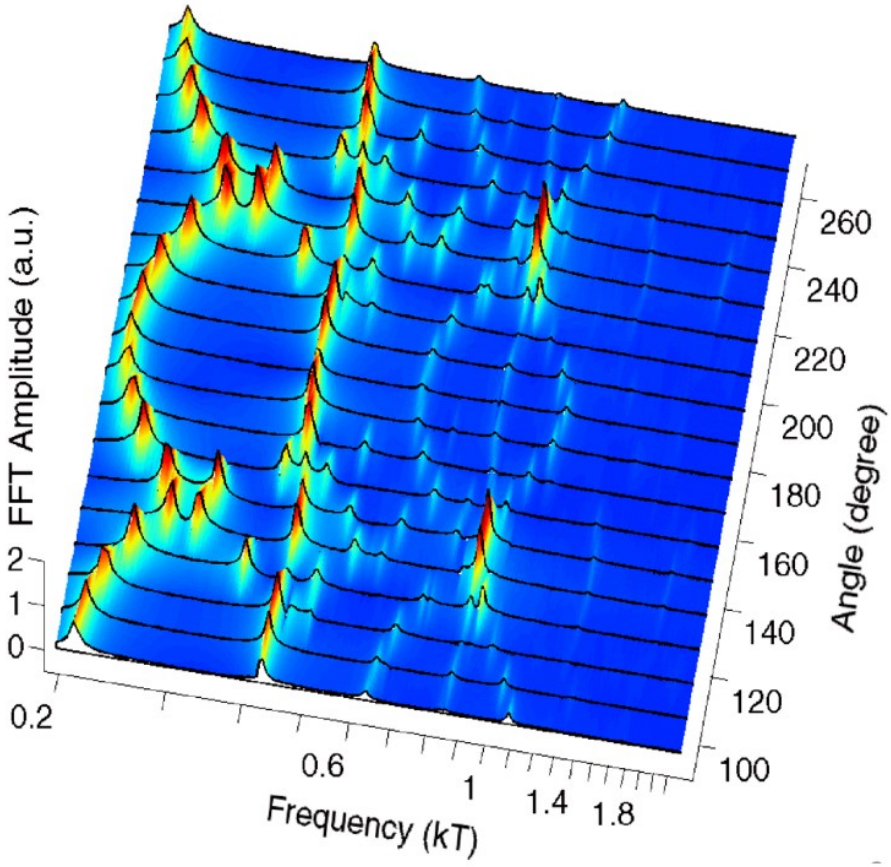

Figure 3.7 | FFT amplitude versus frequency curves. Magnetic field orientations various at angles from $\theta = 91°$ to 271° in step sizes of 10°.

The bulk electronic band structure and Fermi surface of LaSb were investigated more than three decades ago [82-84] and also reported in recent publications [40,41,49]. As shown in the projection on the k_y - k_z plane in Figure 3.8 and in the three-dimensional (3D) plot in Figure 3.1(b), the bulk Fermi surface consists of electron pockets centered at *X* and elongated along the

$\Gamma - X$ direction in addition to two hole pockets centered at Γ. I could observe up to five fundamental frequencies from the bulk Fermi surface with the current–magnetic field configuration given in the inset of Figure 3.2. In Figure 3.6, I can indeed identify four fundamental frequencies and their higher harmonics. Applying the same analysis procedure to the frequencies of the SdH oscillations obtained at other angles, I derive the angle dependences of the four fundamental frequencies. The results are presented as dark blue, green, red, and purple solid circles in Figure 3.9 and labeled as $F_{\alpha 1}$, $F_{\alpha 2}$, F_{β}, and F_{γ} (where α denotes the electron surfaces and β, γ, the hole surfaces). Their higher harmonics are presented with the same symbols but with lighter colors.

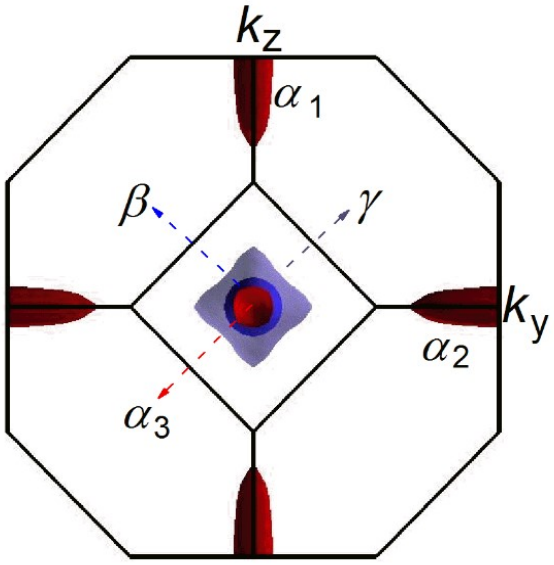

Figure 3.8 | Projection of the calculated Fermi pockets in the magnetic field rotation plane. Corresponding to the (100) plane in the experiment.

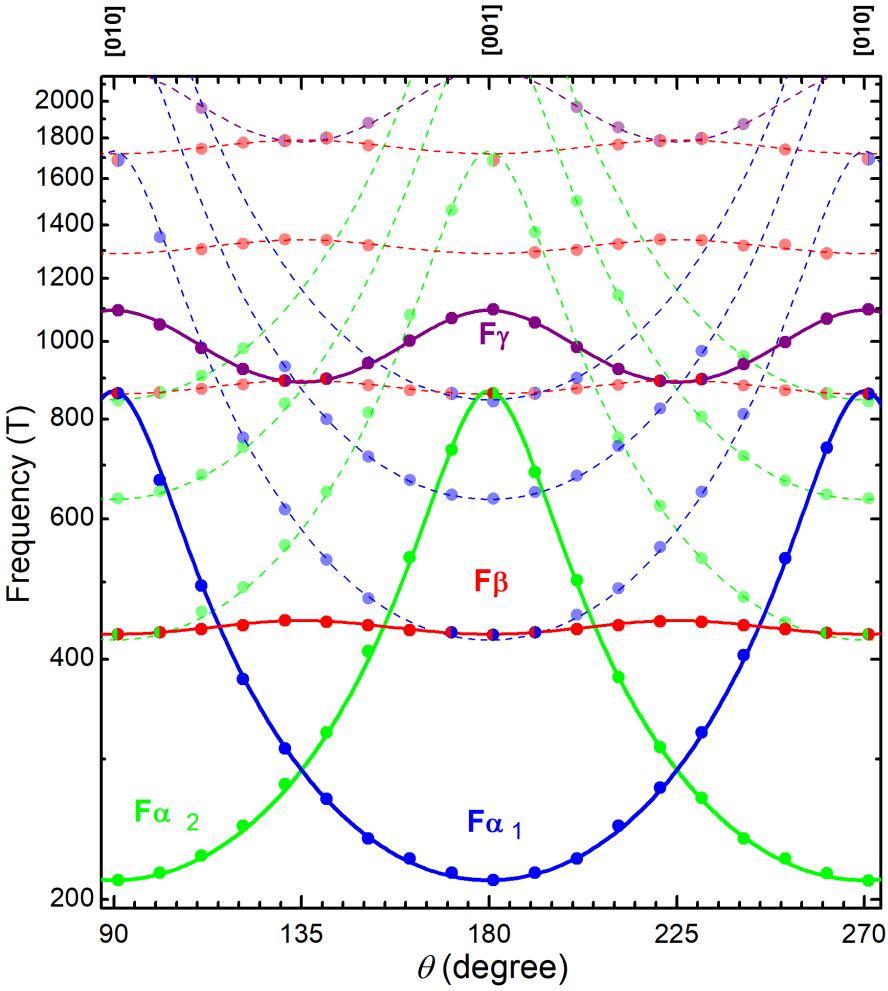

Figure 3.9 | Angle dependence of the SdH oscillation frequencies. The darker symbols and lines represent the fundamental frequencies and the lighter symbols and the dashed lines are their corresponding higher harmonics. The bi-colored symbols represent frequencies that could result from two different Fermi pockets: For $F_{\alpha 1}$, $F_{\alpha 2}$ I have $F_\alpha = F_0/\sqrt{cos^2[\theta-(n-1)\pi/2] + \lambda_\mu^{-2} sin^2[\theta-(n-1)\pi/2]}$, with F_0 = 211.5 Tesla, $\lambda_\mu = \alpha/\beta = 4.1$ and n = 1, 2 for the α_1 and α_2 Fermi pockets. For β and γ bands I have $F_\beta = 430/\sqrt{cos^2 2\theta + 1.04^{-2} sin^2 2\theta}$ and $F_\gamma = 890/\sqrt{cos^2(2\theta-\pi/2) + 1.23^{-2} sin^2(2\theta-\pi/2)}$.

Although I obtained exactly the same frequency of 212 T for H // [001] and H// [010] as previously reported ones [40,41], the large anisotropy of ~4 for $F_{\alpha 1}$, $F_{\alpha 2}$ and the observation of F_{β} and F_{γ} exclude 2D surface states to be (solely) responsible for the observed SdH oscillations. On the other hand, the anisotropy for $F_{\alpha 1}$, $F_{\alpha 2}$ is nearly the same as that of the bulk electron pockets revealed by ARPES [49] and de Haas–van Alphen (dHvA) oscillation [82,83] experiments.

In order to better understand the data in Figure 3.9, I calculated the angle dependence of the SdH oscillation frequencies from the band theory for the bulk Fermi pockets. As presented in Figure 3.10(a) and (b), the α_1 and α_2 electron pockets and the β and γ hole pockets produce SdH oscillations with angle dependences very close to those in Figure 3.10(c): I obtained an anisotropy of 4.25 and a minimum frequency of 225 T for the electron pockets. The calculated angle dependences for all the α_1, α_2, β, and γ pockets agree well with experimental data, as shown in Figure 3.10(c), where the calculated frequencies are multiplied with a scaling factor close to 1, indicating a slight deficiency of the DFT-derived Fermi surface.

I note that the frequencies expected for the electron pocket α_3 in Figure 3.10(a) could not be identified from the experimental data in Figure 3.10(c), similar to that found in the dHvA data [82,83]. One interpretation for this absence is that the frequencies for the electron pocket α_3 in LaSb are about twice that of the hole pocket β, hence hidden by the second harmonic of the latter. On the other hand, recent work on YSb revealed an alternative explanation [54]: The current flows along the long axis of the elliptical α_3 Fermi pocket, thus the mobility of the associated electrons, is very low. Since the oscillation amplitude depends exponentially on the

mobility, $\delta\rho \sim e^{-1/\mu H}$, the SdH quantum oscillations from the α_3 Fermi pocket could be below the measurement sensitivity level associated with our maximum magnetic field of 9 T.

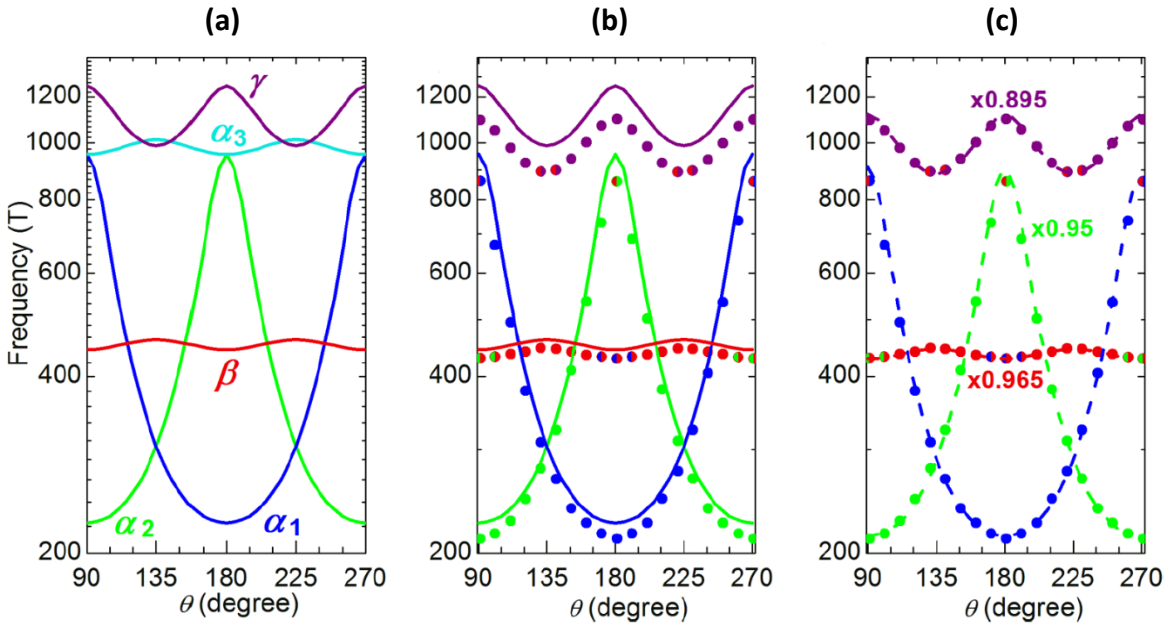

Figure 3.10 | Calculated angle dependence of the SdH oscillation frequencies. (**a**) in the (100) plane for all five Fermi pockets. (**b**,**c**) Comparison of the experimental (symbols) and the calculated values. In (**c**) the calculated curves are scaled by the factor listed and presented as dashed lines to show that their angle dependences are the same as those of the experimental data.

Based on the above discussions, I can confidently conclude that the SdH oscillations observed in our LaSb crystals are solely from the 3D bulk Fermi surfaces, with $F_{\alpha 1}$, $F_{\alpha 2}$, F_{β}, and F_{γ} from the electron pockets α_1 and α_2 and hole pockets β and γ. In Figure 3.10(c) all the detectable frequencies from the FFT analysis can be assigned to these four fundamental frequencies and their higher harmonics. The experimental data presented in Figure 3.10(c) yield a complete picture of the anisotropy of the bulk Fermi surface in LaSb: the electron pockets are highly anisotropic while the hole pockets are nearly isotropic. Quantitatively, the angle dependence of $F_{\alpha 1}$, $F_{\alpha 2}$ can be fitted with

$$F_\alpha = F_0 / \sqrt{cos^2[\theta - (n-1)\pi/2] + \lambda_\mu^{-2} sin^2[\theta - (n-1)\pi/2]} \tag{3.2}$$

where $F_0 = 211.5$ T, $\lambda_\mu = 4.1$, and n = 1, 2 for the α_1, α_2 pockets, respectively.

Since the oscillation frequency F is proportional to the extremal orbit area

$$A = \pi (K_F^S)^2 \sqrt{cos^2\theta + {\lambda_\mu}^2 sin^2\theta} \tag{3.3}$$

with $\lambda_\mu = K_F^L / K_F^S$, where K_F^L and K_F^S being the semimajor and semiminor axes of the elliptic Fermi pocket. Using the Onsager relation $F = (\frac{\phi_0}{2\pi^2})A$, with ϕ_0 being the flux quantum[40], I obtain the short Fermi vector $K_F^S = \sqrt{\frac{2\pi F_0}{\phi_0}} = 8.02 \times 10^6$ cm^{-1} and the long Fermi vector $K_F^L = K_F^S \cdot \lambda_\mu = 3.288 \times 10^7$ cm^{-1} for the electron ellipsoid, corresponding to a density of $7.134 \times$

10^{19} cm^{-3}for each electron pocket and a total electron density of 2.14×10^{20} cm^{-3}. This value is significantly larger than the previously reported one (1.6×10^{20} cm^{-3}) [40], although the values of their F_0 and the short Fermi vector K_F are nearly the same as ours. Note that I used $n = (K_F^S)^2 K_F^L/3\pi^2$ to calculate the density rather than the typically used $n = K_F^3/3\pi^2$ for a spherical Fermi surface [15].

The frequencies for the two hole pockets show a slight angle dependence with a fourfold symmetry. Mathematically, I can fit the data for the β and γ pockets, respectively, with

$$F_\beta = 430/\sqrt{cos^2 2\theta + 1.04^{-2} sin^2 2\theta} \quad (3.4)$$

and

$$F_\gamma = 890/\sqrt{cos^2(2\theta - \pi/2) + 1.23^{-2} \sin^2(2\theta - \pi/2)} \quad (3.5)$$

The "anisotropy" of 1.04 and 1.23 for the β and γ pockets is much smaller than the value (4.1) of the α pockets. In that case, when calculating the hole density, I can easily treat both β and γ pockets as spheres with the average frequencies of 438 and 995 T, corresponding to hole densities of 5.186×10^{19} cm^{-3}and 1.774×10^{20} cm^{-3}, respectively. Thus the total hole density is 2.29×10^{20} cm^{-3}, which is ~6% higher than the electron density, indicating that LaSb is indeed a compensated semimetal, consistent with the ARPES finding on the electron-hole ratio [49].

However, the results of previous ARPES measurement on crystals of another rare-earth monopnictide YSb, indicate that the YSb has a ratio of 0.81 for the electron-hole concentration, preventing me from concluding e-h compensation to the origin of XMR phenomenon on all the rare-earth monopnictides. To better understand the role played in XMR phenomenon by the electron and hole concentration, I conducted magnetotransport measurements on YSb crystals. Angle-dependent SdH oscillations were measured to determine the volume of Fermi pockets and to obtain the charge carriers density as well as the mobility anisotropy.

Figure 3.11 shows a typical $\rho_{xx}(H)$ curve at $T=$ 2.5 K and $\theta=$139.5°. SdH oscillations can be seen at high fields, as evidently shown by the oscillation data in the inset after subtracting a smooth background. FFT analysis result is given in Figure 3.12. Similar to what I observed in the LaSb measurement, four fundamental frequencies and their higher harmonics can be identified. The frequencies can be indexed to $\alpha_1, \alpha_2, \beta$ and γ Fermi pockets shown in the inset.

Applying the same analyzing procedure to the SdH oscillations obtained at various angles, I derived the angle dependences of the frequency *F* for the three bands, as shown in Figure 3.12. Again, the angle dependence of $F_{\alpha 1}, F_{\alpha 2}$ can be quantitatively fitted with Eq. (3.2), which gives F_0 = 355 Tesla, λ_μ = 3.26, and n = 1, 2 for the α_1, α_2 pockets, respectively.

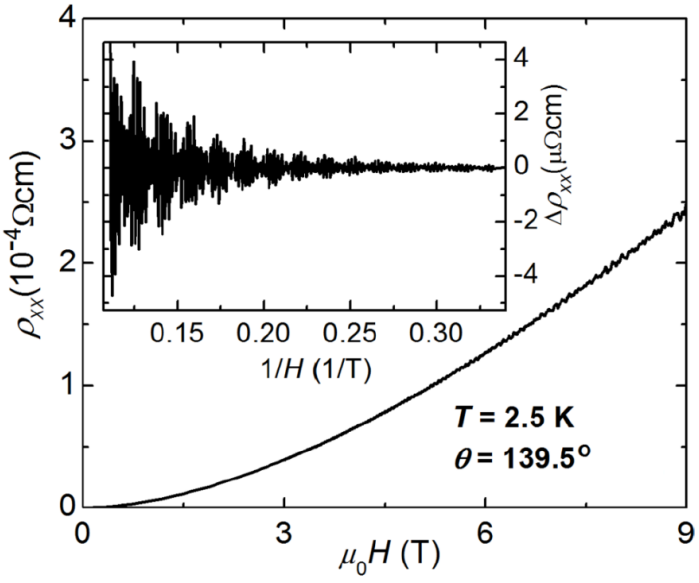

Figure 3.11 | $\rho_{xx}(H)$ curve at $T = 2.5$K and $\theta = 139.5°$. The inset gives the Shubnikov-de Haas (SdH) quantum oscillation data after subtracting a smooth background.

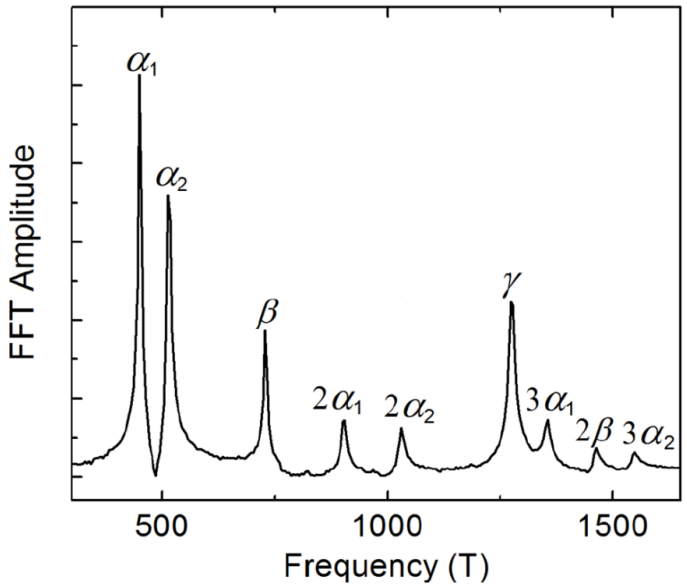

Figure 3.12 | Fast Fourier transform (FFT) analysis of the SdH results.

Correspondingly, I extracted the short Fermi vector $k_F^S = 1.0386\times10^7\ \mathrm{cm}^{-1}$ and the long Fermi vector $k_F^L = \lambda_\mu k_F^S = 3.3858\times10^7\ \mathrm{cm}^{-1}$ for the electron ellipsoid, which led to a density of $n_e^\alpha = 1.2335\times10^{20}\ \mathrm{cm}^{-3}$ for α_1 and α_2 each. Based on the crystal symmetric, the α_3 pocket should have the same density with α_1 and α_2 pockets, which leads to the total electron density being $n_e = 3.7006\times10^{20}\ \mathrm{cm}^{-3}$.

Also, the data for the β and γ pockets can be fitted respectively with

$$F_\beta = 728/\sqrt{cos^2 2\theta + 1.015^{-2} sin^2 2\theta}$$

and $$F_\gamma = 1277/\sqrt{cos^2(2\theta - \pi/2) + 1.115^{-2} sin^2(2\theta - \pi/2)}$$

Due to the nearly negligible 'anisotropy' of 1.015 and 1.115 for the β and γ pockets, I treat both β and γ Fermi pockets as spheres with the mean frequencies of F_β = 732 T and F_γ = 1351 T, corresponding to hole densities of $n_h^\beta = 1.1204\times10^{20}\ \mathrm{cm}^{-3}$ and $n_h^\gamma = 2.8091\times10^{20}\mathrm{cm}^{-3}$, respectively. This results in a total hole density of $n_h = 3.9295\times10^{20}\mathrm{cm}^{-3}$. Thus, I obtained an electron-hole ratio of $n_e/n_h = 0.942$ for sample I. The SdH results for sample II are presented in Figure 3.13, revealing $n_e/n_h = 0.949$. That is, both samples give consistent results and reveal that YSb is a compensated semimetal.

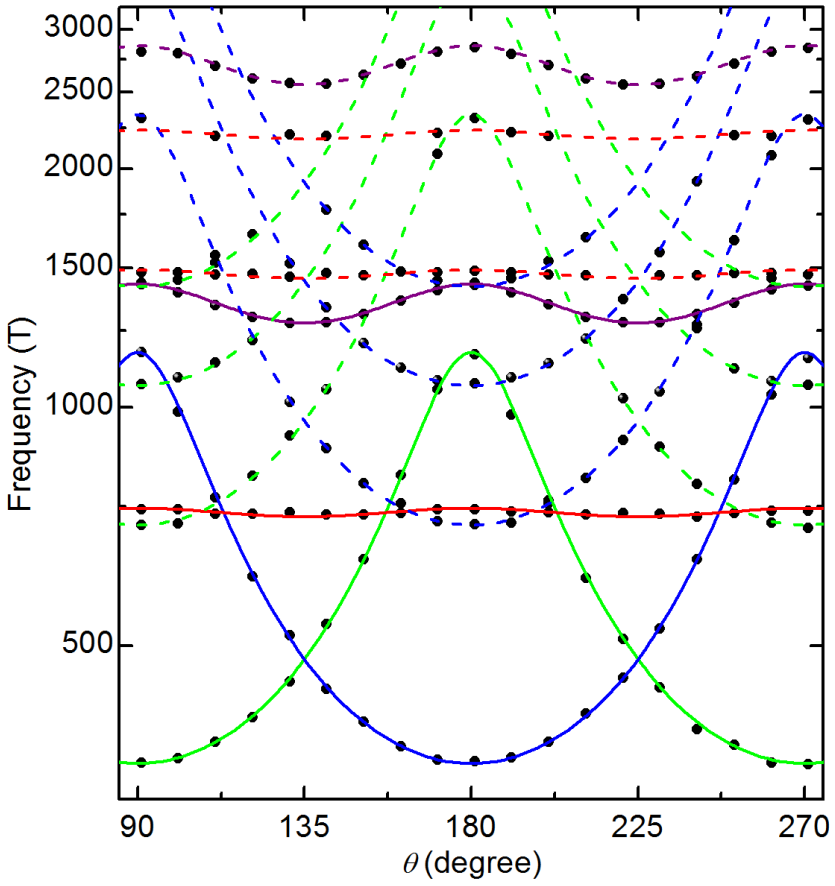

Figure 3.13 | Angle dependence of the SdH oscillation frequencies for a YSb sample. The darker symbols and lines represent the fundamental frequencies and the lighter symbols and the dashed lines are their corresponding higher harmonics. For $F_{\alpha 1}$, $F_{\alpha 2}$ I have $F_\alpha = F_0/\sqrt{cos^2[\theta-(n-1)\pi/2] + \lambda_\mu^{-2} sin^2[\theta-(n-1)\pi/2]}$, with F_0 = 355 Tesla, λ_μ = 3.3 and n = 1, 2 for the α_1 and α_2 Fermi pockets. For β and γ bands I have $F_\beta = 727/\sqrt{cos^2 2\theta + 1.025^{-2} sin^2 2\theta}$, $F_\gamma = 1277/\sqrt{cos^2(2\theta-\pi/2) + 1.12^{-2} sin^2(2\theta-\pi/2)}$.

$n_e^\alpha = 1.24866 \times 10^{20}$ cm^{-3}, i.e., $n_e = 3.74597 \times 10^{20}$ cm^{-3}; $n_h^\beta = 1.12954 \times 10^{20}$ cm^{-3}, $n_h^\gamma = 2.8169 \times 10^{20}$ cm^{-3}, i.e., $n_h = 3.94646 \times 10^{20}$ cm^{-3}, resulting in a ratio of $n_e/n_h = 0.949$.

The experimental results from measurements on both the YSb and LaSb samples clearly indicate that the rare-earth monopnictides exhibiting XMR have compensated electron and hole concentration.

3.3. Separation of electron and hole dynamics

Figure 3.14(a) presents the magnetic-field dependence of the sample resistivity $\rho(H)$ at T = 3 K and H // [001]. As shown in the inset, this sample has a large MR of 4.45×10^4% at $\mu_0 H = 9$ T. At high magnetic fields, $\rho(H)$ follows a power-law dependence with an exponent of 2, consistent with that reported in other XMR materials [12,90]. Such a quadratic relationship that implies a non-saturating magnetoresistance can be derived from the isotropic two-band model with e-h compensation [12], which has become the most prevalent explanation for the origin of the XMR [12,40,41,43,44]. Indeed, ARPES experiments [49] and our SdH oscillation measurements reveal a nearly perfect *e-h* compensation in LaSb. I can also use the isotropic two-band model to fit ρ(H) of our LaSb crystal, with the derived physical parameters ($n_e = 9.03 \times 10^{19}$ cm^{-3}; $n_h = 8.77 \times 10^{19}$ cm^{-3}; $\mu_e = 0.673$ m^2 V^{-1} s^{-1}; $\mu_h = 0.639$ m^2 V^{-1} s^{-1}) very close to those reported in Ref.[40]. Although the n_e/n_h ratio does indicate a nearly compensated nature, the absolute values of the n_e and n_h are less than half of those determined by our SdH experiments. Furthermore, the isotropic two-band mode cannot account for the fourfold angle dependence of the resistivity $\rho(\theta)$, as delineated in Figure 3.14(b). Although the surface states of a topological material such as SmB_6 could induce a similar fourfold angular magnetoresistance [92,93], the anisotropy in Figure 3.14(b) shows that nearly perfect fourfold symmetry should not

arise from the crystal surfaces, since the crystal's width (223.33 μm) is much larger than its thickness (138.78 μm). ARPES experiments [49] have revealed that LaSb is topologically trivial. Also, analysis on the resistivity plateau and quantum oscillations I did clearly revealed their bulk origin.

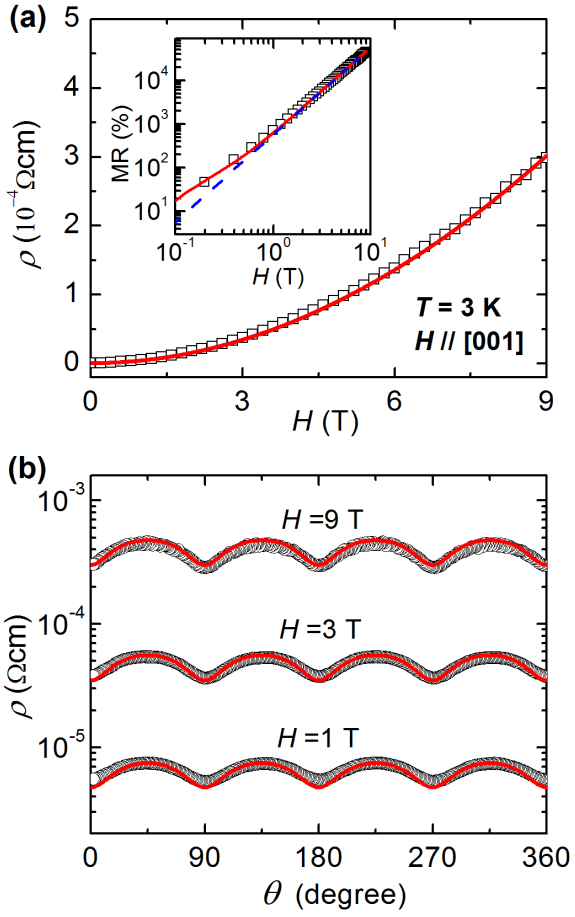

Figure 3.14 | Temperature (a) and angle (b) dependences of the resistivity of sample. Data were taken at $T = 3$ K. Symbols are the experimental data and solid lines are fits to Eq. (3.12). Inset of (a) shows the *MR*, with the dashed line presenting a quadratic field dependence.

The magnetoresistance of a material with a bulk anisotropic Fermi surface can also vary with magnetic-field orientation due to the anisotropic mobility [73,94]. Strong anisotropy in the magnetoresistance was observed in XMR materials such as bismuth [73,94] and graphite [95] as well as in WTe_2 [85]. As presented in Figure 3.8, which shows the projection of the calculated Fermi pockets in the magnetic-field rotation plane, LaSb has two pairs of elongated electron Fermi pockets α_1 and α_2 in the k_y -k_z plane, and hence an anisotropic magnetoresistance is expected when the magnetic field is rotated in this plane. In order to correctly describe the magnetoresistance anisotropy, I need to consider the effects of the elongated Fermi pockets.

According to Abeles and Meiboom [96], Aubrey [97] the current density and the charge conduction by a Fermi pocket with a carrier concentration n in the presence of electric and magnetic fields is given by:

$$\vec{j} = \hat{\sigma} \cdot \vec{E} = ne\hat{\mu}\vec{E} + \hat{\mu}\vec{j} \times \vec{B} \tag{3.6}$$

and

$$\hat{\sigma} = ne\left(\hat{\mu}^{-1} + \hat{B}\right)^{-1} \tag{3.7}$$

where n is the electron density. For a non-topological material with a bulk ellipsoidal electron Fermi surface, and current flowing along the third axis, the mobility tensor and magnetic field tensor is given as following:

$$\hat{\mu} = \begin{pmatrix} \mu_1 & 0 & 0 \\ 0 & \mu_2 & 0 \\ 0 & 0 & \mu_3 \end{pmatrix} \tag{3.8}$$

and $$\hat{B} = \begin{pmatrix} 0 & 0 & B\sin\theta \\ 0 & 0 & -B\cos\theta \\ -B\sin\theta & B\cos\theta & 0 \end{pmatrix} \quad (3.9)$$

Here μ_1, μ_2, and μ_3 are the mobilities along the three axes of the ellipsoid. The magnetic field rotates in the 1-2 plane and θ is the angle of the magnetic field tilted away from the first axis. Therefore, I get the conductivity given as

$$\hat{\sigma} = ne\left(\hat{\mu}^{-1} + \hat{B}\right)^{-1} = ne\begin{pmatrix} \frac{1}{\mu_1} & 0 & B\,sin\,\theta \\ 0 & \frac{1}{\mu_2} & -B\,cos\,\theta \\ -B\,sin\,\theta & B\,cos\,\theta & \frac{1}{\mu_3} \end{pmatrix}^{-1} \quad (3.6)$$ which

corresponding to

$$\hat{\sigma} = \frac{ne\mu_1\mu_2\mu_3}{1+B^2\mu_3(\mu_2 cos^2\theta+\mu_1 sin^2\theta)} \times \begin{pmatrix} \frac{1}{\mu_2\mu_3} + B^2\cos^2\theta & B^2\sin\theta\cos\theta & \frac{B\,sin\,\theta}{\mu_2} \\ B^2\sin\theta\cos\theta & \frac{1}{\mu_1\mu_3} + B^2\sin^2\theta & -\frac{B\,cos\,\theta}{\mu_1} \\ -\frac{B\,sin\,\theta}{\mu_2} & \frac{B\,cos\,\theta}{\mu_1} & \frac{1}{\mu_1\mu_2} \end{pmatrix} \quad (3.7)$$

Equations (3.7) – (3.11) are applicable to an ellipsoidal hole pocket by changing the sign of both the charge *e* and the mobility. They can also be implemented for the case of a spherical Fermi pocket by assuming $\mu_1 = \mu_2 = \mu_3$. Eq. (3.11) indicates that the magnetoconductivity of each Fermi pocket is hence determined by four parameters (n, μ_1, μ_2, and μ_3).

LaSb has one electron band α with three orthogonal Fermi pockets (α_1, α_2, and α_3) and two hole bands β and γ [see Figure 3.1(b) and Figure 3.8]. In order to account for the measured

magnetoresistivity, I need to include contributions from all five Fermi pockets in Eq. (3.12) with $\sigma_{ij}^{T} = \Sigma_k \sigma_{ij}^{k}$, where $k = \alpha_1, \alpha_2, \alpha_3, \beta$, and γ . An anisotropic Fermi pocket can be regarded as an ellipsoid, as shown in Figure 3.15. Once the ratio of the ellipsoid's semimajor and semiminor axes $K_F^L$and K_F^S is known, the relationship of the mobility along the long axis $\mu_{\parallel}$ and the short axis $\mu_{\perp}$ can be described as $\mu_{\perp}/\mu_{\parallel} = m_{\parallel}/m_{\perp} = (K_F^L/K_F^S)^2 = \lambda_{\mu}^2$, where $m_{\parallel}$ and $m_{\perp}$ are the effective masses along the long and short axes [95]. That is, only one of the three mobilities is an independent fitting parameter.

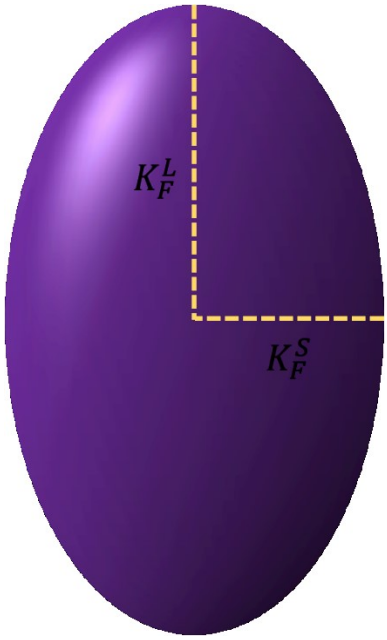

Figure 3.15 | Schematic of an isotropic Fermi pocket. The semimajor and semiminor axes $K_F^L$and K_F^S represent the long and short Fermi vectors.

For example, I can rewrite the longitudinal magnetoconductivity for the α_1, α_2, and α_3 Fermi pockets as $\sigma_{33}^{e1} = ne_1\mu_\perp/[1+\mu_\perp^2H^2(\cos^2\theta+\sin^2\theta/\lambda_\mu^2)]$, $\sigma_{33}^{e2} = ne_2\mu_\perp/[1+\mu_\perp^2H^2(\cos^2\theta/\lambda_\mu^2+\sin^2\theta)]$, $\sigma_{33}^{e3} = ne_1\mu_\parallel/[1+\mu_\perp^2H^2/\lambda_\mu^2]$. λ_μ can be determined through Shubnikov–de Haas (SdH) quantum oscillation measurements, with $\lambda_\mu = 4.1$ for sample A. Due to the crystalline symmetry, α_1, α_2, and α_3 are exactly the same Fermi pocket but oriented differently. Thus they have the same electron density, i.e., $ne1 = ne2 = ne3$. Considering the zero field conductivity for the α_1, α_2, and α_3 Fermi pockets, I have $\sigma_{33}^{10} = \sigma_{33}^{20} = \sigma_{33}^{e0} = ne_1\mu_\perp$ and $\sigma_{33}^{30} = \sigma_{33}^{30}/\lambda_\mu^2$. That is, I have only two independent fitting parameters (σ_{33}^{e0} and $\mu_\perp$) for the three electron Fermi pockets. For simplification I combine the two spherical hole bands into one with an isotropic mobility of μ_H and a zero-field conductivity of σ_{33}^{h0} . With these two parameters I can obtain σ_{ij} for the combined hole bands, e.g., $\sigma_{xx} = \sigma_{xx}^{h0}/[1+\mu_h^2H^2]$ and $\sigma_{xy} = \sigma_{xx}^{h0}\mu_hH/[1+\mu_h^2H^2]$.

Considering the magnetotransport measurement I did on the LaSb and YSb sample, after taking all the 5 Fermi pocket into account, I obtain the magnetoresitivity tensor:

$$\hat{\rho} = \begin{pmatrix} \rho_{xx} & \rho_{yx} \\ \rho_{xy} & \rho_{yy} \end{pmatrix} = \widehat{\sigma^T}^{-1} \tag{3.8}$$

with $\sigma_{ij}^T = \Sigma_k\sigma_{ij}^k$, where $k = \alpha_1$, α_2, α_3, β, and γ .

As presented in Figure 3.14, Eq. (3.12) can quantitatively describe the measured $\rho(H)$ and $\rho(\theta)$ with $\sigma_{33}^{e0} = 6.05 \times 10^5 \text{S cm}^{-1}$, $\sigma_{33}^{h0} = 3.0 \times 10^5 \text{S cm}^{-1}$, $\mu_\perp = 9.27\ \text{m}^2\text{V}^{-1}\text{s}^{-1}$ ($\mu_\parallel = \mu_\perp/\lambda_\mu^2 = 0.552\ \text{m}^2\ \text{V}^{-1}\ \text{s}^{-1}$), and $\mu_H = 1.5\ \text{m}^2\ \text{V}^{-1}\ \text{s}^{-1}$. Interestingly, the above hole mobility is not far away from that ($\mu_h = 0.964\ \text{m}^2\ \text{V}^{-1}\ \text{s}^{-1}$) derived using the isotropic two-band model that gives an electron mobility ($\mu_e = 1.118\ \text{m}^2\ \text{V}^{-1}\ \text{s}^{-1}$) differing significantly from the values of $\mu_\perp$ and $\mu_\parallel$.

These analyses provide another approach to calculate the electron and hole density in the YSb crystal, and hence to explore if there is *e-h* compensation in the system. I found that the fit of Eq. (3.12) to the experimental data is very sensitive to the values of the carrier density. I was unable to achieve reasonable fits to both $\rho_{xx}(H)$ and $\rho_{xy}(H)$ by applying the experimental n_e^α, n_h^β and n_h^γ. Since first principles calculations give a more complicated γ Fermi pocket than the one I determined from its projection on the (100) plane, our estimated concentration n_h^γ could have significant deviation. In the analysis I treat n_h^γ as a free variable.

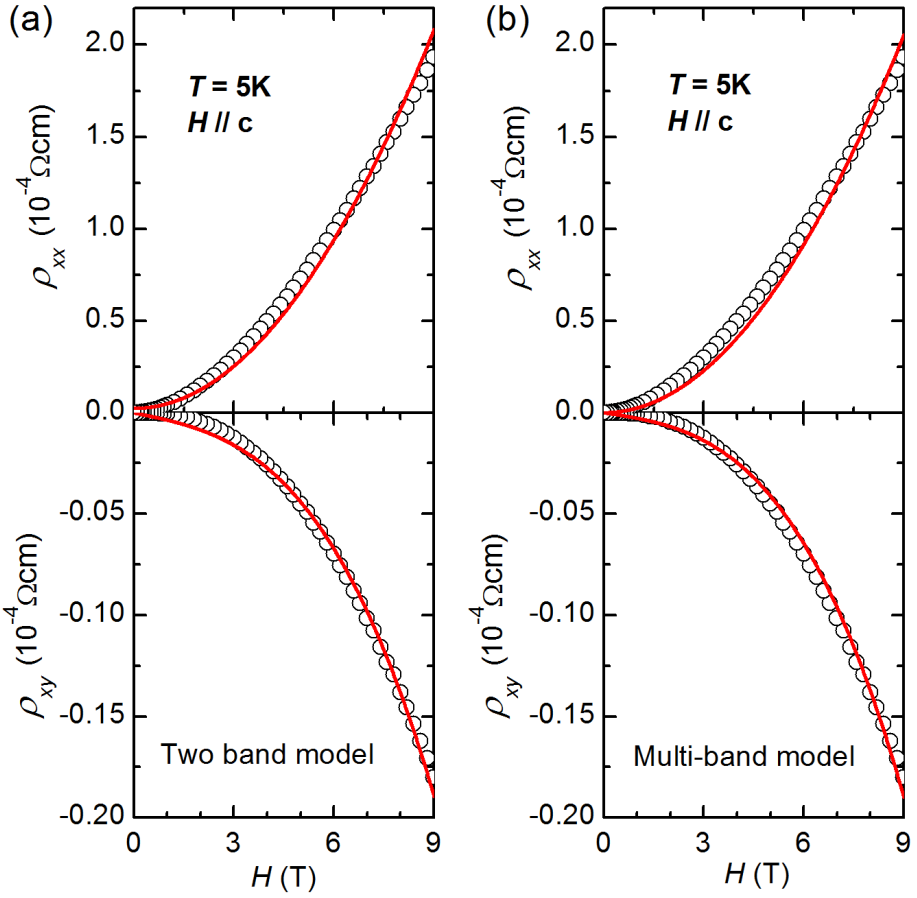

Figure 3.16 | Analysis of the Hall and longitudinal magnetoresistivities. Data were taken for sample I at $T = 5$ K and H //c: (a) with the isotropic two-band model using $n_e = 1.202 \times 10^{20}$ cm^{-3}, $n_h = 1.22 \times 10^{20}$cm^{-3}, $\mu_e = 0.935$ m^{2}V^{-1}s^{-1} and $\mu_h = 1.056$ m^{2}V^{-1}s^{-1}, (b) with the anisotropic multi-band model Eq. (3.12) using n_e^{α} and n_h^{β} determined through SdH measurements and $n_h^{\gamma} = 2.558 \times 10^{20}$cm^{-3}, $\mu_{\perp}^{\alpha} = 11.96$ m^{2}V^{-1}s^{-1}, $\mu_h^{\beta} = 9.64$ m^{2}V^{-1}s^{-1} and $\mu_h^{\gamma} = 2.482$ m^{2}V^{-1}s^{-1}. Symbols are experimental data and solid lines are the fits.

Using the experimentally determined n_e^{α}, n_h^{β}, I can use Eq. (3.13) to quantitatively describe both $\rho_{xx}(H)$ and $\rho_{xy}(H)$, as shown in Figure 3.16. It gives $n_h^{\gamma} = 2.558 \times 10^{20}\text{cm}^{-3}$, $\mu_{\perp}^{\alpha} = 11.96$ m^{2}V^{-1}s^{-1}, $\mu_h^{\beta} = 9.64$ m^{2}V^{-1}s^{-1}, $\mu_h^{\gamma} = 2.482$ m^{2}V^{-1}s^{-1}, where $\mu_{\perp}^{\alpha}$ is the mobility along the short axis of the electron Fermi pocket. These mobility values differ significantly from the μ_e and μ_h derived using the isotropic two-band model, demonstrating the need to include the anisotropy and multi-band nature of the material in a quantitative MR analysis. For comparison, I present in Table 3.1 a summary of the density and mobility of the charge carriers derived from the SdH measurements, the isotropic two-band model and anisotropic multi-band model. I note that the derived $n_h^{\gamma} = 2.558 \times 10^{20}\text{cm}^{-3}$ obtained through analysis with Eq. (3.13) is ~9% smaller than that (2.8091×10^{20} cm^{-3}) from SdH measurements, resulting in n_e/n_h = 1.006. This indicates that YSb may indeed be a perfect compensated system.

Table.3.1 | Summary of the derived density and mobility of YSb sample.

	Density	**Density ratio**
SdH quantum oscillations	$n_e = 3.7006\times10^{20}$ cm^{-3} $n_h = 3.9295\times10^{20}$ cm^{-3}	n_e/n_h = 0.942
Isotropic two-band model	$n_e = 1.202 \times 10^{20}$ cm^{-3} $n_h = 1.223 \times 10^{20}$ cm^{-3}	n_e/n_h = 0.982

To further demonstrate the role played by the compensated multi-bands in the occurrence of XMR, I show in Figure 3.17 the calculated ρ_{xx} and ρ_{xy} for a single Fermi pocket and combinations thereof using the parameters obtained from above analysis using Eq. (3.13). If only the Fermi pocket α_1 were present, I find a field independent ρ_{xx} and hence the absence of a MR. However, the addition of pockets α_2 and α_3 results in a magnetic field-dependent ρ_{xx} with a *MR* ≈ 300% at $H = 9$ T. ρ_{xx} is further enhanced by adding the hole pockets, resulting in ρ_{xx} to reach an extremely large value of 1.3×10^5 %.

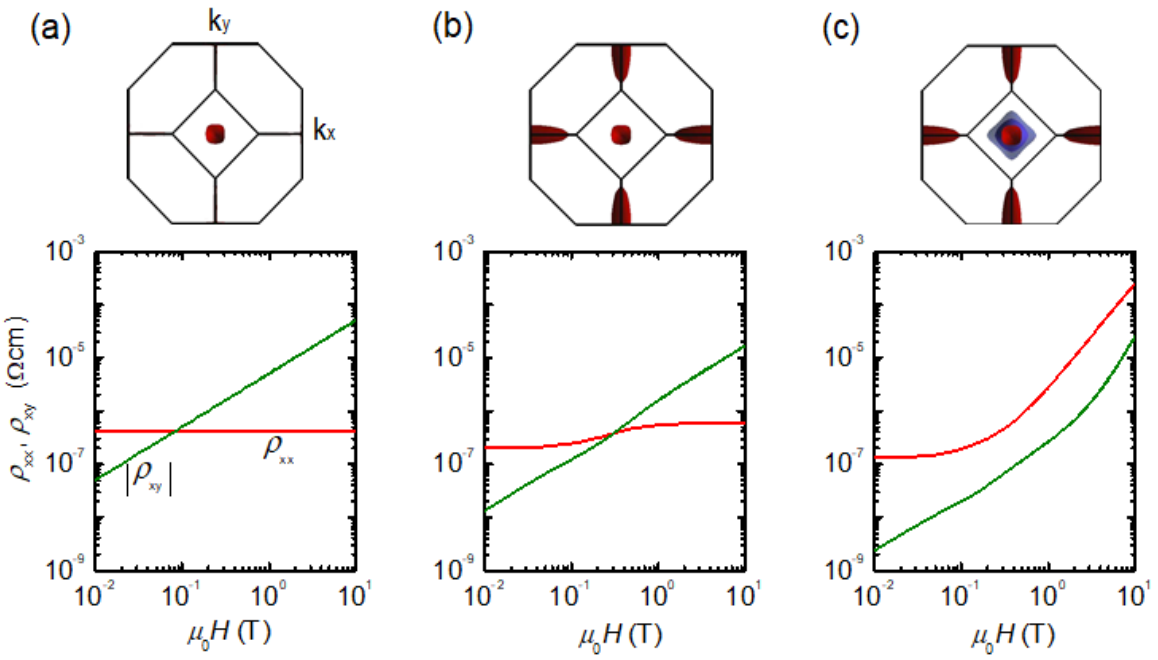

Figure 3.17 | Calculated ρ_{xx} and ρ_{xy}. Eq. (3.12) was used with parameters derived from the analysis of data in Figure 3.16. (a) Single Fermi pocket α_1, (b) multiple Fermi pockets $\sum_{i=1}^{3}\alpha_i$, and (c) all five electron and hole Fermi pockets. The top panel is the projection of the corresponding Fermi pockets in the orbital (001) plane.

3.4. Discussion and conclusion

In this part of the dissertation research, I succeeded in the separation of electron and hole dynamics in rare-earth monopnictides LnX (LaSb and YSb) by investigating the anisotropic magnetoresistance and demonstrated that the XMR in them originates solely from the bulk. I used Kohler's rule scaling to understand the observed resistivity plateau without having to invoke topological protection. I conducted Shubnikov–de Haas oscillation experiments and found that the results agree well with our analysis of the bulk Fermi surfaces, excluding a possible surface origin.

I further showed that both the magnetic-field and angle dependences of the sample resistivity can be quantitatively described with a semiclassical theory that accounts for the anisotropic mobility of the ellipsoidal electron Fermi pockets. The analysis indicates that both the electrons and holes have high mobility and the multiband nature results in a diminishing Hall effect. The high mobility together with diminishing Hall effect lead to the observed XMR in LnX: The high mobility produces a strong field-dependent longitudinal magnetoconductivity. With diminishing Hall effect, the measured magnetoresistivity becomes the inverse of the longitudinal magnetoconductivity, leading to the emergence of XMR behavior. Both the electrons and holes are found to play important roles in the observed XMR and their relative contributions vary with the strength and orientation of the magnetic field. I demonstrated that investigations of the anisotropic magnetoresistance provide a convenient way to separate the dynamics of charge carriers and to uncover the origin of the XMR in multiband materials with

anisotropic Fermi surfaces. The high mobility with diminishing Hall effect can also explain XMR behavior in other materials.

In the next chapter, I will present another type of magnetoresistance behavior in semimetals, which is the large saturating magnetoresistance. I observed this behavior in the crystals of NbP, and I will discuss how it can be understood by defining an experimentally determinable parameter – the Hall factor.

4. Saturating XMR In Transition-Metal Monophosphides

4.1. Weyl semimetal NbP

Weyl semimetals of the transition-metal monophosphides TaAs, TaP, NbAs, and NbP [18,21,24,29,57-59,74,76-78,98-107] are new exotic topological quantum materials that have recently attracted extensive attention. They host Weyl fermions in the bulk and feature Fermi arcs on the surfaces [98]. Their bulk and surface band structures have been directly revealed through APRES [21,74,77,78,98-103]. Experiments on electronic transport, which is crucial for potential applications in electronic devices, have uncovered novel properties such as ultrahigh mobility [18,57], extremely large magnetoresistance (XMR) [18,57], and chiral-anomaly induced negative magnetoresistance [21,24,29,59].

Analogous to topological insulators [108-111], the surface states of Weyl semimetals could exhibit unusual quantum phenomena such as weak antilocalization induced by quantum interference [60]. Furthermore, weak antilocalization and localization [60] could arise from Weyl fermions in the bulk [21,24,60,61,76], highlighting the likely prospects for these materials as platforms for exploring novel phenomena. Indeed, saturating magnetoresistances (MRs), which typically do not occur in non-Weyl XMR materials, have recently been observed in NbAs [59] and NbP [18,58] crystals at liquid-helium temperatures. They could be an indication of contributions from the topological surfaces that could have a saturating MR due to weak antilocalization and/or from the disordered bulk, which could have both weak antilocalization

and localization and could induce a negative MR [60]. The temperature dependence of the MR in TaAs crystals [21] shows a reentrant metallic behavior similar to that observed in graphite [7], which has been attributed to the magnetic field induced occurrence of local superconductivity. Recently, tip induced superconductivity was reported in TaAs [112] and surface superconductivity in NbAs through selective ion sputtering [113].

4.2. Reentrant metallic behavior

In the previous chapter, I discussed the temperature turn-on behavior in the rare-earth monopnictides, which is widely thought to be a key feature of XMR materials. However, in this chapter, I will show a very different magnetoresistivity versus temperature behavior, which is called reentrant metallic behavior, in the transition-metal monophosphide NbP.

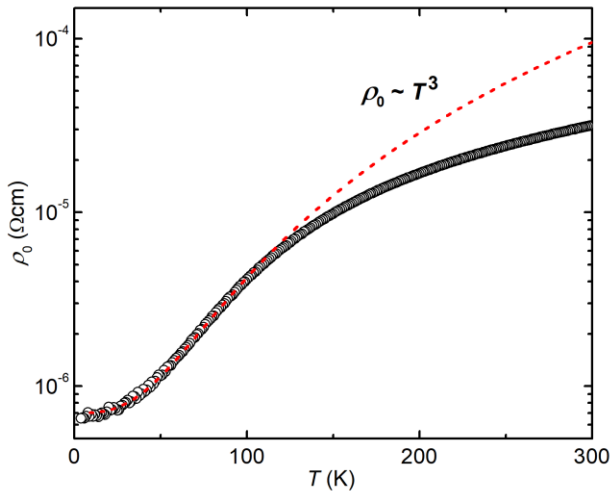

Figure 4.1 | Temperature dependence of the zero-field resistivity $\rho_0(T)$.

As expected for a semimetal, the zero-field resistivity ρ_0 given in Figure 4.1 for NbP decreases when the temperature is lowered. However, in the presence of an external magnetic field *H*, the temperature dependence of the resistivity becomes complicated, as presented in Figure 4.2. At $H \leq 1$T, the temperature dependence of the magnetoresistivity $\rho_{xx}(T)$ at $T < 100$ K can become semiconductor-like, i.e., a magnetic field induced suppression of the metallic behavior occurs. At larger fields, the metallic temperature dependence reappears following the semiconductor-like behavior, leading to a clearly defined peak in all $\rho_{xx}(T)$ curves above $H =$ 1.5 T. The magnetic field induced reentrant metallic behavior in $\rho_{xx}(T)$ is reminiscent of similar response first observed in graphite [7]. Likewise, as shown in Figure 4.3, the magnetic field dependence of the peak temperature $T_p(H)$ also follows a power-law relationship $T_p \sim (H - Hc)^{1/\nu}$, with $\nu = 3$, similar to that reported for graphite ($\nu \approx 2 - 4$) [7,114,115]. Since its discovery in graphite in 2003, the reentrant metallic behavior has been observed both in non-topological semimetals including Bi [115] and Sb [116] as well as recently in topological semimetals $Bi_{0.96}Sb_{0.04}$ [117], TaAs [21,118], and WP_2 [119]. In the first report in graphite [7], this phenomenon was attributed to the occurrence of local superconductivity induced by quantum Hall effect in the quantum limit. However, this mechanism cannot account for the reentrant metallic behavior observed in other materials mentioned above, the quantum limits of which were not reached in the reported experiments. Recently, the claim on "hidden superconductivity" in graphite was questioned by Forgan [120], although he could not give alternative explanation. Thus, the reentrant metallic behavior in topological and non-topological semimetals remains an unsolved puzzle.

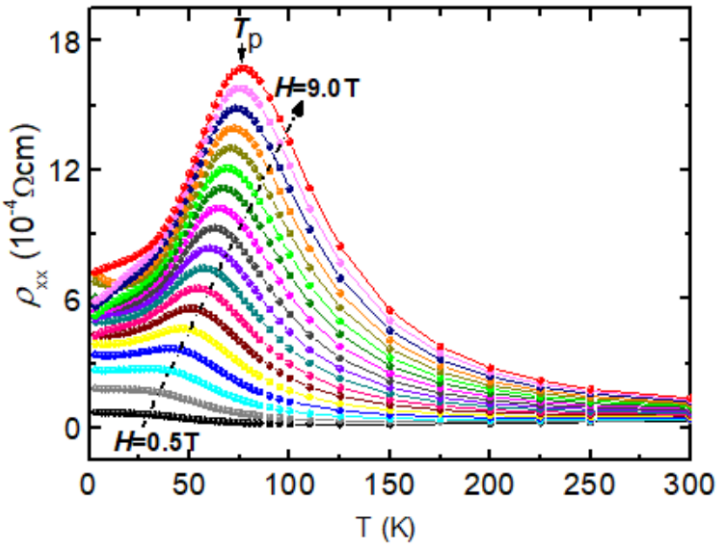

Figure 4.2 | Temperature dependence of the magnetoresistivity $\boldsymbol{\rho_{xx}(T)}$. Data were taken at H = 0.5 to 9 T with intervals of 0.5 T.

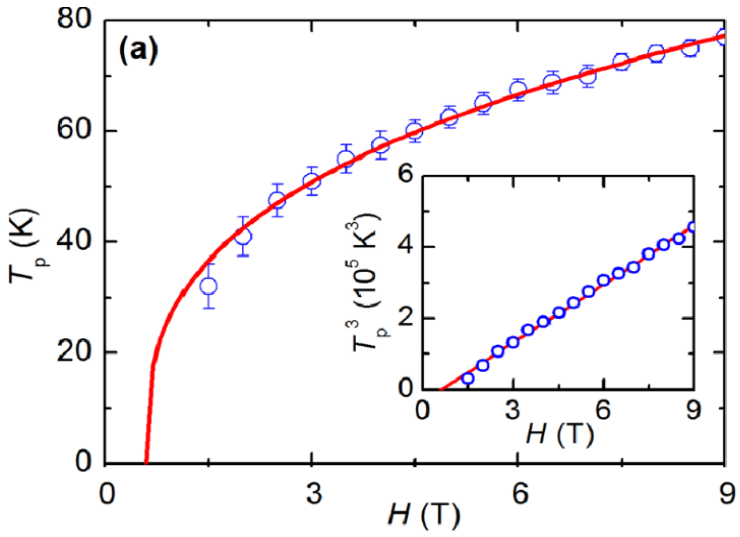

Figure 4.3 | The magnetic field dependence of the peak temperature (T_p). The symbols are experimental data and the line represents $T_p \sim (H - Hc)^{1/3}$. The inset presents the $T_p(H)$ data as $T^3 \sim H$ to directly show the power-law dependence.

4.3. Hall factor

In a semiclassical theory, for a magnetic field *H* applied in the *z* direction and current flowing along the *x* axis, the magnetoresistivity tensor is given as [54]

$$\hat{\rho} = \begin{pmatrix} \rho_{xx} & \rho_{yx} \\ \rho_{xy} & \rho_{yy} \end{pmatrix} \tag{4.1}$$

while the magentoconductivity tensor as

$$\hat{\sigma} = \begin{pmatrix} \sigma_{xx} & \sigma_{yx} \\ \sigma_{xy} & \sigma_{yy} \end{pmatrix} \tag{4.2}$$

Since these two tensors are the inverse of each other, I have $\rho_{\mathrm{xx}} = \sigma_{yy}\,/[\sigma_{xx}\sigma_{yy} + (\sigma_{xy})^2]$, $\rho_{\mathrm{yy}} = \sigma_{xx}/[\sigma_{xx}\sigma_{yy} + (\sigma_{xy})^2]$ and $\rho_{\mathrm{yx}} = -\rho_{\mathrm{xy}} = \sigma_{xy}\,/[\sigma_{xx}\sigma_{yy} + (\sigma_{xy})^2]$. And for the electron pocket $\sigma_{xx} = ne\mu_x/(1 + \mu_x\mu_y H^2)$, $\sigma_{yy} = ne\mu_y/(1 + \mu_x\mu_y H^2)$, and $\sigma_{yx} = -\sigma_{xy} = ne\mu_x\mu_y H/(1 + \mu_x\mu_y H^2)$. Here *n* is the electron density, and μ_x and μ_y are the respective mobilities along the *x* and *y* axes. For a hole pocket, σ_{ij} can be obtained by changing the sign of both the charge *e* and the mobility. It can also be implemented for the isotropic case by assuming $\mu_x = \mu_y$.

NbP has four Fermi pockets with two pairs for the electrons and holes, respectively [58]. To calculate its magnetoresistivity, σ_{ij} in Eq. (4.2) needs to be replaced with $\sigma_{ij} = \Sigma_p \sigma_{ij}^p$ where p represents all the Fermi pockets. Since σ_{ij} for each Fermi pocket has three free variables (n, μ_x, μ_y), it is nearly impossible to conduct a quantitative analysis of the magnetoresistivity for

NbP by directly using Eq. (4.1). Currently, the popular analysis approach is to adopt an isotropic two-band model [18,21,57], i.e., Eq. (4.1) is simplified by assuming that the densities of electrons and holes are compensated, all Fermi pockets are spherical, and the electrons and holes from different Fermi pockets have the same mobility μ_e and μ_h, respectively. As demonstrated in the previous chapter, the outcome of such an analysis for a multiband material could be unreliable.

I can reformulate Eq. (4.1) to avoid the need of detailed information on individual Fermi pockets by utilizing experimentally accessible parameters. The crystal symmetry in NbP and the magnetic field symmetry during measurement lead to $\sigma_{xx} = \sigma_{yy}$, and $\sigma_{yx} = -\sigma_{xy}$, thus $\rho_{xx} = \rho_{yy}$and $\sigma_{xx} = \rho_{yy}/(\rho_{xx}^2 + \rho_{xy}^2)$. Then, the relationship for ρxx and σxx can be written as

$$\rho_{xx} = 1/(\sigma_{xx} + \kappa_H \sigma_{xx}) \tag{4.3}$$

with $\kappa_H = \left(\rho_{xy}/\rho_{xx}\right)^2$, which I term as the Hall factor. Eq. (4.3) shows that the measured magnetoresistivity ρ_{xx} is determined by the magnetoconductivity σ_{xx} together with an additional term $\Delta\sigma_{xx} = \kappa_H \sigma_{xx}$ contributed by the Hall effect. Since $\kappa_H \geq 0$, thus $\rho_{xx} \leq 1/\sigma_{xx}$. Furthermore, σ_{xy} and ρ_{xy} have opposite signs for electrons and holes, as given in Eqs. (4.1) and (4.2). Thus, the values of σ_{xy} and ρ_{xy} could decrease with the addition of a Fermi pocket. In the extreme case where the σ_{xy} and ρ_{xy} of electrons and holes compensate each other, $\kappa_H \approx 0$ and ρ_{xx} reaches its maximum $\rho_{xx}^M = 1/\sigma_{xx}$. When $\kappa_H \neq 0$, Eq. (4.2) indicates that its temperature

and magnetic field dependences will affect those of ρ_{xx}. That is, κ_H can be the determining factor for the temperature behavior of ρ_{xx}.

Experimentally, κ_H can be conveniently obtained by simultaneously measuring ρ_{xx} and ρ_{xy} . In Figure 4.4, I presented the temperature dependence of $\kappa_H(T)$ obtained at various magnetic fields with the corresponding ρ_{xy} given in the inset. Clearly, the reentrant metallic behavior in ρ_{xx} is accompanied by a rapidly increasing κ_H with decreasing temperature.

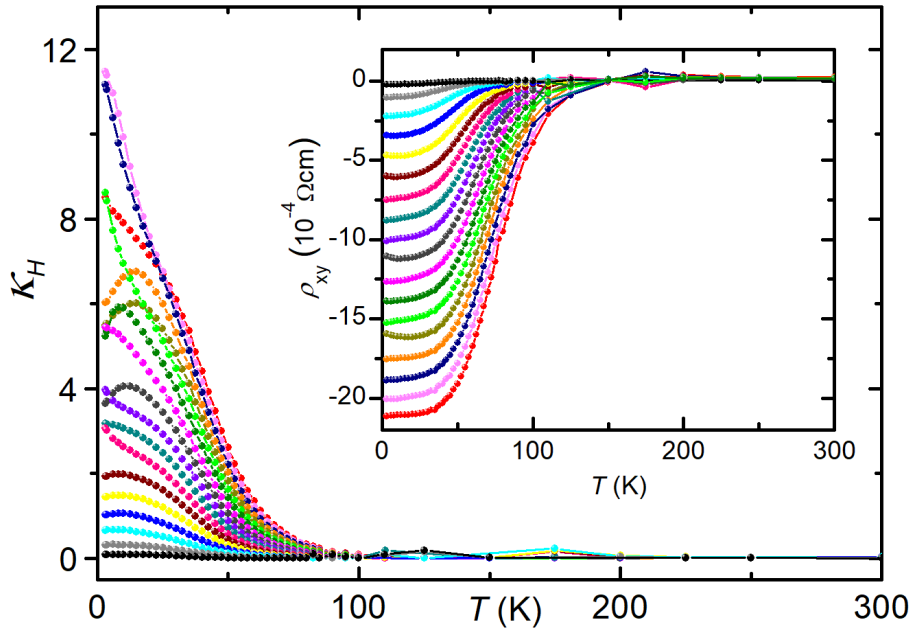

Figure 4.4 | Temperature dependence of the Hall factor. $\kappa_H = (\rho_{xy}/\rho_{xx})^2$, with the Hall magnetoresistivity $\rho_{xy}(T)$ given in the inset. The symbols are the same with that in Figure 4.2.

In Figure 4.5, I use the $\rho_{xx}(T)$ curve obtained at $H = 9$ T to elucidate the role of κ_H on the reentrant metallic behavior. In Figure 4.6 I present the calculated σ_{xx} , $\kappa_H\sigma_{xx}$, and their sum $\sigma_{xx}+\kappa_H\sigma_{xx}$. It shows that σ_{xx} decreases monotonically as the temperature is lowered and its sum with the Hall effect induced magnetoconductivity, $\kappa_H\sigma_{xx}$, also follows the same behavior when the value of κ_H is small at high temperatures. At lower temperatures (T < 100 K), however, the temperature response of σ_{xx} and $\kappa_H\sigma_{xx}$ diverges because of the rapid increase of κ_H with decreasing temperature, resulting in a dip in the $\sigma_{xx}+\kappa_H\sigma_{xx}$ curve. This corresponds to the observed peak in $\rho_{xx}(T)$, which is the inverse of $\sigma_{xx}+\kappa_H\sigma_{xx}$. The upper limit (ρ_{xx}^M) of $\rho_{xx}(T)$ in the absence of the Hall contribution, i.e., $\kappa_H = 0$, is also presented in Figure 4.5 with a dashed green curve. It indicates that the reentrant metallic behavior occurs only when $\rho_{xx}(T)$ deviates significantly from ρ_{xx}^M . In fact, I can rewrite Eq. (4.3) as $\rho_{xx} = \rho_{xx}^M/(1 + \kappa_H)$. That is, κ_H is a direct measure of the deviation of $\rho_{xx}(T)$ from its upper limit. Its sufficiently large value as well as fast change with temperature give rise to this intriguing reentrant behavior.

In order to directly demonstrate the correlations between $\kappa_H(T)$ and the reentrant metallic behavior, I plot $\kappa_H(T)$ and normalized $\rho_{xx}(T)$ curves obtained at the same fields in the inset of Figure 4.7. It shows that the peak in $\rho_{xx}(T)$ occurs nearly at the same κ_H, independent of the magnetic fields. Data in the main panel of Figure 4.7 give $\kappa_H \approx 0.4$ at T_p for all given magnetic fields.

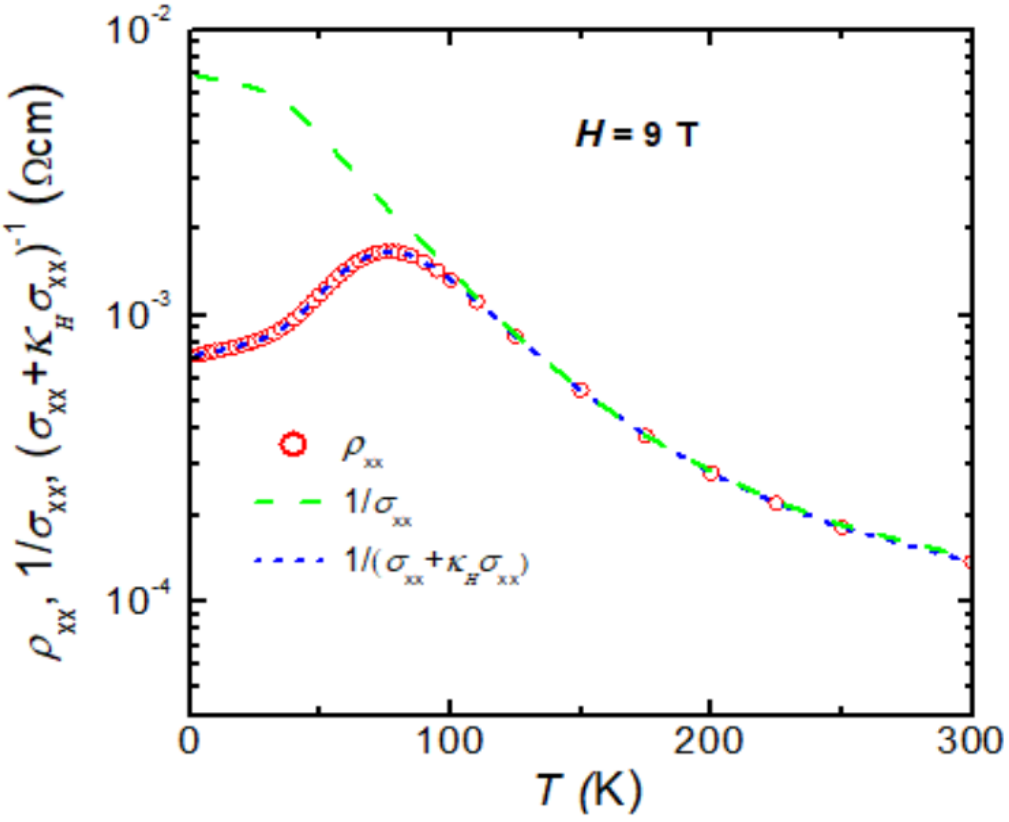

Figure 4.5 | Temperature dependence of the magnetoresistivity. Curves show the measured ρ_{xx} at H = 9T and the calculated magnetoresistivity ($1/\sigma_{xx}$) without the contribution ($\Delta\sigma_{xx} = \kappa_H\sigma_{xx}$) from the Hall field.

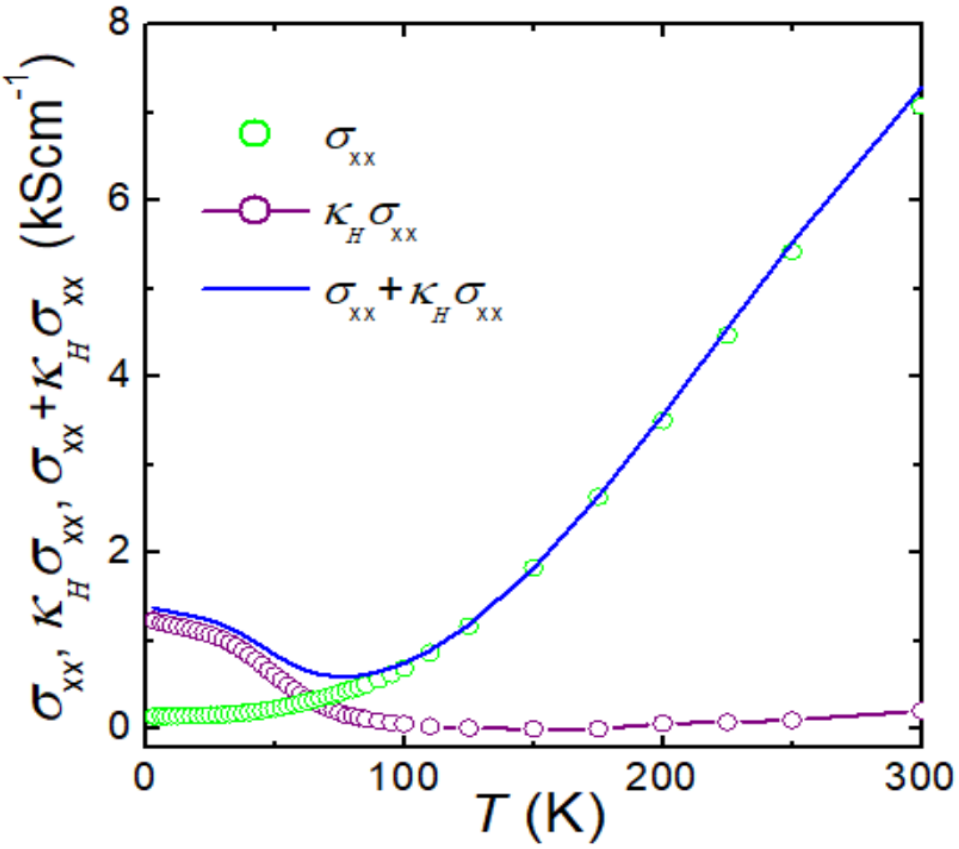

Figure 4.6 | Temperature dependence of the magnetoconductivity. Curves of the measured magnetoconductivity σ_{xx} , the calculated Hall-field induced component $\kappa_H\sigma_{xx}$, and their sum $\sigma_{xx} + \kappa_H\sigma_{xx}$, demonstrating the competition of σ_{xx} and $\kappa_H\sigma_{xx}$ in their temperature dependence and the occurrence of a dip in their sum $\sigma_{xx} + \kappa_H\sigma_{xx}$.

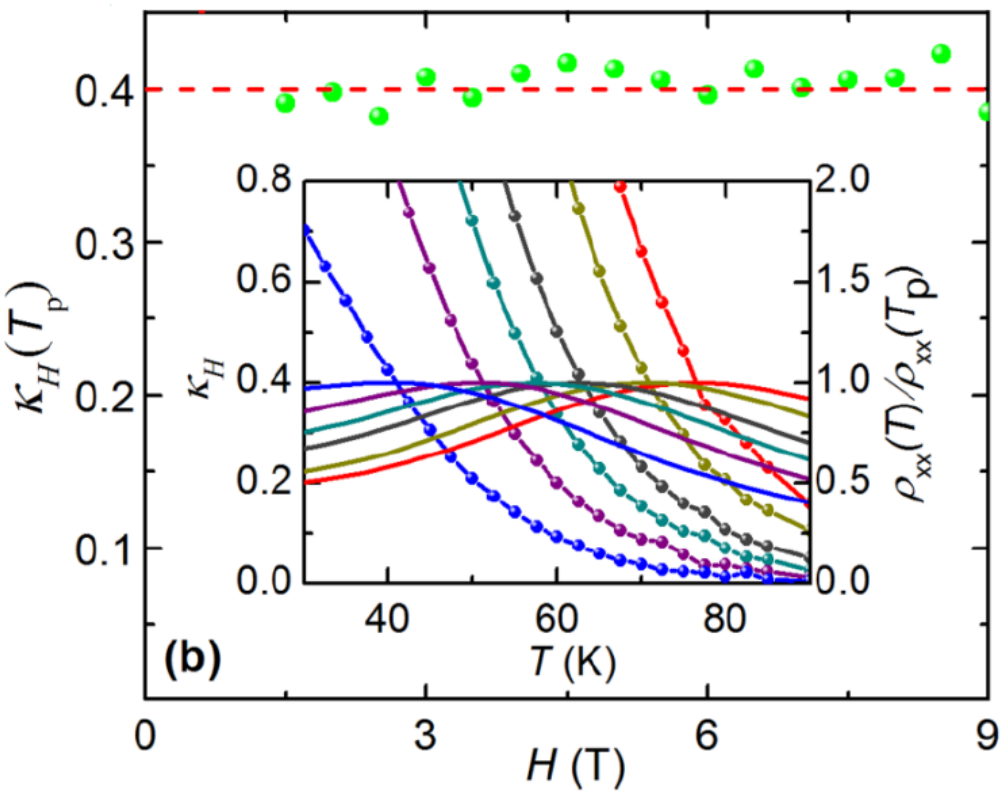

Figure 4.7 | The magnetic field dependence of the Hall factor κ_H at peak temperature T_p. The inset contains data of $\kappa_H(T)$ (symbols) and the associated normalized magnetoresistivity (lines) at H = 2,3,4,5,7, and 9 T, demonstrating that the Hall factor is nearly the same at the peak temperature for $\rho_{xx}(T)$ curves obtained in different magnetic fields.

Without knowing the temperature dependence of the density and mobility of the charge carriers in each Fermi pocket in this multiband material, one is unable to analytically derive the temperature dependence of the Hall factor κ_H and its value at T_p. Our experimental finding of field independence of κ_H at T_p, however, could be useful in understanding the T_p versus H relationship, which was used as evidence for supporting the magnetic field induced "superconductivity" interpretation of the reentrant metallic behavior in graphite [7]. In the case of graphite, which can be described with an anisotropic two-band model, I obtain $\kappa_H = [(n_e - n_h)\,\mu_y H/(n_e + n_h)]^2$ using Eqs. (4.1) – (4.3) by assuming $\mu_x^e = \mu_x^h = \mu_x$ and $\mu_y^e = \mu_y^h = \mu_y$, where *e* and *h* in the subscript and superscript stand for electron and hole, respectively. If n_e and n_h are independent of temperature or have similar temperature dependence, a constant $\kappa_H(T_p)$ implies that $\mu_y H$ is the same at different T_p, i.e., $\mu_y H$ = const. Since μ_y should behave the same as μ_x, the temperature dependence of the mobility μ_y can be inferred from that of the zero-field resistivity $\rho_0(T) = 1/[(n_e + n_h)e\mu_x]$. This leads to $\mu_y(T) \sim 1/\rho_0(T)$. Thus, I have $H \sim 1/\mu_y(T_p) \sim \rho_0(T_p)$. For a Fermi liquid with $\rho_0(T) = a + bT^2$ I can deduce a power-law relationship for $T_p \sim (H - H_c)^{1/2}$ with H_c related to a. This is exactly what was observed by Kopelevich et al. in graphite and bismuth [115]. The situation in a multiband system should be more complicated. In our NbP, however, $T_p(H)$ also seems to correlate strongly with $\rho_0(T)$. Data in the Figure 4.1 for our NbP crystal at T < 100 K indicate $\rho_0(T) = a + bT^\nu$ with $\nu = 3$, which is the same exponent derived from the power-law relationship of $T_p(H)$, as discussed above and shown in Figure 4.3. In general, $\rho_0(T)$ at low temperatures can be described as $\rho_0(T) = a + bT^\nu$ with $\nu = 2$ for electron-electron scattering (in Fermi liquid) and $\nu = 3$ and 4 for electron-phonon scattering in the pure and dirty limit, respectively [121,122]. In

XMR materials, v is often found to be 2 [43,90,123] while $v = 3$ [45,89] and 4 [40] are also reported. Thus, I can conclude that a power-law dependence may be a general behavior of $T_p(H)$, with the exponent that can be estimated from $\rho_0(T) = a + bT^v$. In fact, $T_p \sim (H - H_c)^{1/v}$ with $v = 4$ was also reported for graphite [114], although it was attributed to spin-orbit interactions. Thus, no exotic mechanism such as magnetic field induced local superconductivity is needed to account for the observed power-law behavior of $T_p(H)$.

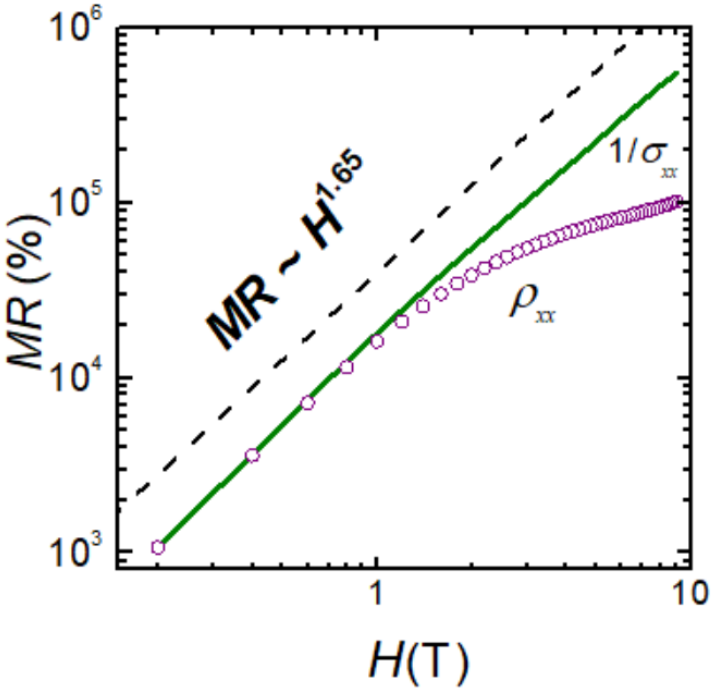

Figure 4.8 | Measured magnetoresistance at different fields. The dashed line indicates a power-law relationship, in the absence of Hall contribution, with an exponent of 1.65.

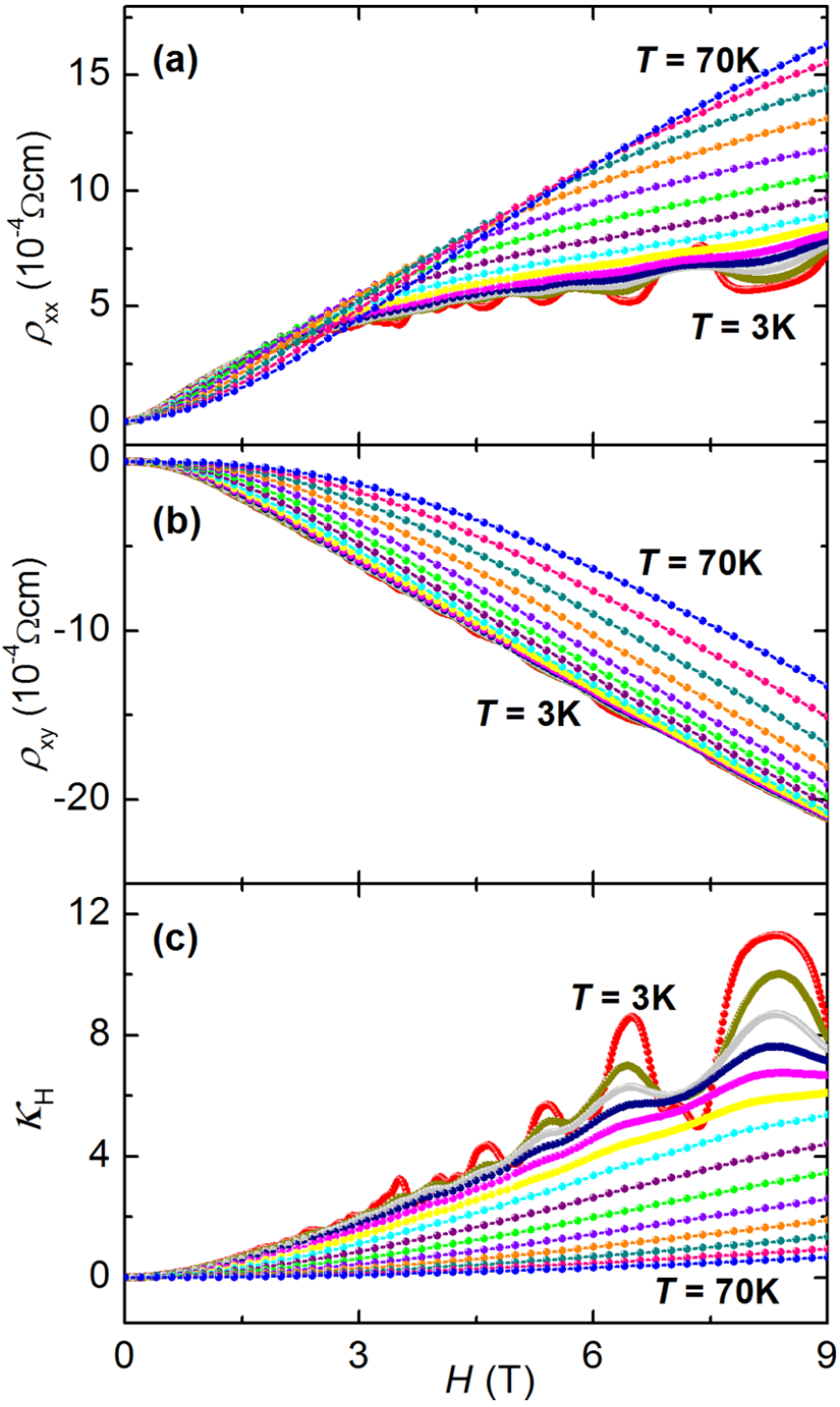

Figure 4.9 | Magnetic field dependence of resistivity and the Hall factor. (a) the transverse magnetoresistivity $\rho_{xx}(H)$, (b) the Hall magnetoresistivity $\rho_{xy}(H)$, and (c) the Hall factor $\kappa_H = \left(\rho_{xy}/\rho_{xx}\right)^2$ at temperatures $T = 3$ and $10 - 70$K at intervals of 5 K.

Accompanying the reentrant metallic temperature behavior I also observed significant variation in $\rho_{xx}(H)$, ranging from unsaturated at high temperature ($T > 70\ K$) to saturation at liquid-helium temperatures, as shown in Figure 4.9. In a Weyl semimetal, quantum interference could induce weak antilocalization on the surface and both weak antilocalization and localization in the bulk [60]. Combined with the orbital magnetoresistivity, this could result in a complicated $\rho_{xx}(H)$ behavior, as demonstrated by the multivariable fitting of the saturating magnetoresistivity in $Bi_{0.97}Sb_{0.03}$ [60]. As shown in Figure 4.8, however, the MR of our NbP crystal is larger than 10^5% even at 40 K, excluding the possibility of (anti)localization behavior in the crystal. In Figure 4.10, I demonstrate that the variation in $\rho_{xx}(H)$ is due to the magnetic field dependence of the Hall factor $\kappa_H(H)$. Applying the same procedure used in the analysis of $\rho_{xx}(T)$ in Figure 4.5, I show the calculated $\sigma_{xx}(H)$, $\kappa_H\sigma_{xx}$, and their sum $\sigma_{xx} + \kappa_H\sigma_{xx}$ in Figure 4.10(b). It indicates that at low fields the Hall effect plays a negligible role and the total magnetoconductivity ($\sigma_{xx} + \kappa_H\sigma_{xx}$) is nearly equal to σ_{xx} , while at high fields it saturates to a value determined by the Hall effect ($\kappa_H\sigma_{xx}$). I also plot $\kappa_H(H)$ in Figure 4.10(b). It indicates that a noticeable deviation of $\sigma_{xx} + \kappa_H\sigma_{xx}$ from σ_{xx} occurs at κ_H larger than 0.4, the value determined at T_p [see inset of Figure 4.3]. Comparison of $\rho_{xx}(H)$ with its upper limit ρ_{xx}^M in Figure 4.10(a) shows that the measured magnetoresistivity is only a fraction (~1/5 at H = 9 T) of its potential MR. The plot in the Figure 4.8 also indicates that MR in the absence of the Hall contribution follows a power-law behavior with an exponent (=1.65) close to but less than 2, consistent with that observed in non-Weyl materials showing nonsaturating XMR [54,85,124].

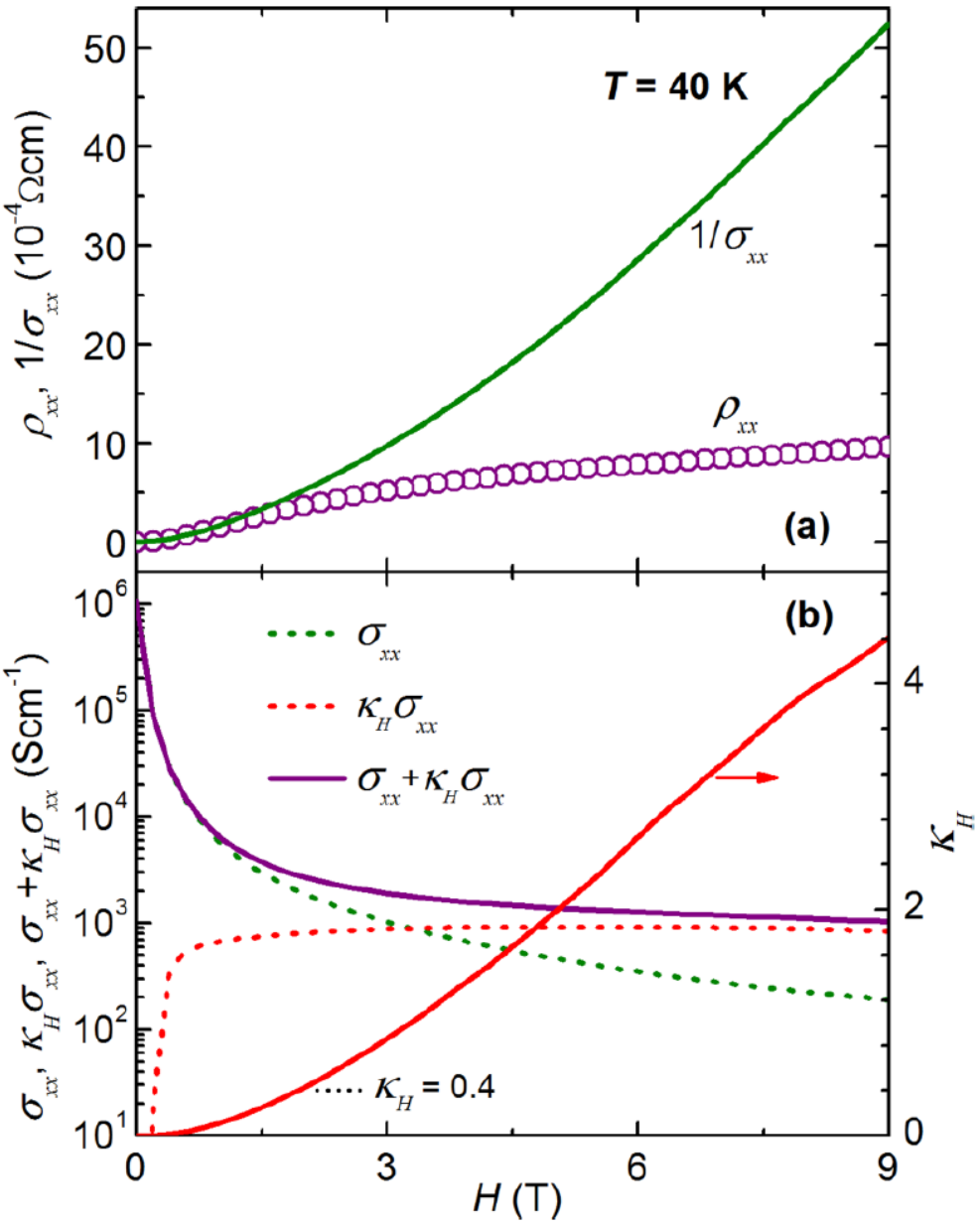

Figure 4.10 | Magnetoresistance influenced by Hall effect. (a) Comparison of the measured $\rho_{xx}(H)$ (symbols) and its upper limit $1/\sigma_{xx}(H)$ at $T = 40$ K. (b)Magnetic-field dependence of the calculated magnetoconductivity σ_{xx}, the additional component $\Delta\sigma_{xx} = \kappa_H\sigma_{xx}$ contributed by the Hall field and their sum. $\kappa_H(H)$ is also plotted in (b), which indicates that the deviation of $\rho_{xx}(H)$ to $1/\sigma_{xx}(H)$ becomes noticeable at $\kappa_H > 0.4$.

4.4. Discussion and conclusion

In this experiment, I observed reentrant metallic temperature behavior accompanied with saturating large magnetoresistivity in the Weyl semimetal NbP. I quantitatively described these phenomena with a semiclassical theory and revealed that they originate from the temperature and magnetic field dependence of the Hall factor.

Eq.(4.3) indicates the upper limit of longitudinal resistivity for a material could be reached only if the Hall factor was close to zero. Correspondingly, based on my calculation, the Hall factors of the typical XMR materials reported in literature, are all very small. While those materials, in which the magnetoresistance are saturating, have large Hall factors. Those experimental observation and theoretical calculations gave me a clear picture on the origin of XMR, which is a combination of high mobility charge carriers, a compensating electron-hole density, and a diminishing Hall effect.

In the next chapter, I will present another type of novel magnetoresistance behavior, i.e., negative longitudinal magnetoresistance (NLMR), which attracted intensive attention in recent years. I will show the observation of this behavior in GaAs quantum wells and reveal its mechanism.

5. Negative Longitudinal Magnetoresistance In GaAs Quantum Wells

With the recent discovery of topological materials, the MR phenomenon has been attracting extensive attention [12,15,16,18,21,22,24-34,41,64]. Two of the most remarkable findings are the extremely large MRs for $H \perp I$ [12,15,18,41] and the negative longitudinal MRs (NLMRs) for $H // I$ [16,21,22,24-34,64]. As discussed in the previous chapters, I attributed the former behavior to electron-hole compensation and high mobility of charge carriers in the presence of diminishing Hall factor [12,124]. The origin of the NLMR, however, is currently under debate. In disordered systems such as films of topological insulator Bi_2Se_3 [32] and Dirac semimetal Cd_3As_2 [33], the NLMR is attributed to distorted current paths due to conductivity fluctuations induced by macroscopic disorder as revealed in computer simulations for polycrystalline $Ag_{2\pm x}Se$ samples [125,126]. In contrast, the NLMR in single crystals of these materials [16,21,22,24-28,64] is often considered as a manifestation of Weyl fermions due to the chirality imbalance in the presence of parallel magnetic and electric fields [62,63]. Recently, theories with topological [127,128] and trivial [128-130] states have been developed to understand the observed NLMR without invoking chiral anomaly. However, some puzzling concerns have been raised on NLMR experiments [131]. For example, numerous non-Weyl materials exhibit NLMRs [31,65-67]. Even within the class of Weyl semimetals, NLMRs are not consistently observed in the same material [14,132]. Furthermore, the reported NLMRs show unpredicted features such as non-monotonic magnetic field behavior [16,21,27]. More disturbingly, it has

been demonstrated that NLMRs can be artificially induced by non-uniform current injection [131,133].

5.1. Negative longitudinal magnetoresistance

I conducted magnetotransport measurements on GaAs quantum wells, in which microscopic disorder induces novel phenomena such as quantum Hall plateaus [134] and linear magnetoresistance [135]. I observed NLMRs with both monotonic and non-monotonic magnetic field dependence similar to those reported in topological materials. Furthermore, the NLMRs in our quantum wells exhibit an intriguing temperature behavior: they occur at temperatures below 5 K, disappear at intermediate temperatures (> 5 K), and re-appear at high temperatures (T > 130 K and up to 300 K). The NLMR is most pronounced at 160 – 180 K. After excluding experimental artifacts and accounting for the various features in their magnetic field dependence using a simple three-resistor model, I attribute the observed NLMRs to microscopic disorder including impurity and interface roughness or randomly distributed dopants.

I measured four samples in standard Hall-bar geometry, defined through photolithographic patterning. Three of them are Hall bars on the same wafer and connected to each other, sharing the same applied current and denoted as Samples 1a, 1b and 1c in Figure 5.1. The fourth sample (sample 2) is the same Hall bar structure fabricated on a separate wafer. All the samples behave qualitatively the same (see Table 5.1 for a summary of the characteristic parameters including the low-temperature electron densities for all four samples). Here I focus on results of Sample 1b, with additional data from other samples if comparison is needed.

Figure 5.1 | Photograph of the GaAs quantum well wafer with fabricated Hall bar samples. Dashed rectangles highlight the three measured Hall bars. Indium was used to make the Ohmic contacts. Gold wires of 50 μm in diameter were used for electrical connections. The expanded view shows the current and voltage connections for sample 1.

Table.5.1 | Summary of parameters for the measured samples.

Parameters / Samples	$R_0(\Omega)$ at 300K	n (10^{10}cm^{-2}) at 3K	T_p (K)	T_M (K)	Maximal NLMR	N_0 (10^{12}cm^{-2})	E_A (meV)
Sample W1a	3451	8.16	150.5	180	-4.16%	3.45	38.8
Sample W1b	2420	8.72	145	165	-6.14%	3.05	34.1
Sample W1c	1366	8.83	144	165	-7.68%	2.25	31.9
Sample W2	4002	7.91	154	190	-3.85%	2.23	35.3

T_p is the temperature at which the R_0 (T) curve has a peak (see Figure 5.7a); T_M is the temperature at which maximal NLMR occurs for that sample; N_0 and E_A are derived from the fit of $n(T)$ curve at high temperatures using $n = N_0\exp(-E_A/k_BT)$ (see Figure 5.7b).

I obtained data on the magnetic field dependence of the sample resistance $R(H)$ at fixed temperatures and angles between the magnetic field and the current. At temperatures below 5 K, I observed negative MRs for both $H\ //I$ ($\theta = 0°$) (Figure 5.2 and Figure 5.3) and $H \perp I$ ($\theta = 90°$) (see Figure 5.2). At $T > 5\ K$ MRs become entirely positive for both magnetic-field orientations (see Figure 5.2). With further increase in temperature, the MRs for $H\ //I$ begin to display non-monotonic behavior, and NLMR behavior re-emerges at the medium magnetic fields (see Figure 5.3 for MRs at 133 K). At $T > 145\ K$ and up to room temperature, the MRs become

purely negative, although they are non-monotonic at temperatures between 145 K and 210 K. From the $R(H)$ curves obtained at various temperatures, I construct the temperature dependence of MR. The Cartesian plots of the results for Sample 1b is presented in Figure 5.4. Color maps that can show both the *MR*'s temperature and magnetic field dependences are given in Figure 5.5 for all four samples. These plots and maps clearly show that all samples exhibit similar NLMRs, with some quantitative variation from sample to sample, e.g., the maximum NLMR changes from -3.85% in Sample 2 at 190 K to -7.68% in Sample 1c at 165 K (see Table 5.1 for results of other samples). The variations, particularly those in samples patterned on the same wafer, i.e., Samples 1a, 1b and 1c, suggest that the NLMR may originate from local properties such as microscopic disorder, consistent with what I propose below.

The features including both the monotonic and non-monotonic magnetic field dependences in the $R(H)$ curves shown in Figure 5.3 are akin to those reported in crystals [16,21,25,27,28] and films [32,33] of topological materials. The $R(H)$ curves presented in Figure 5.6 for Sample 1b at 170 K and various angles indicate that negative MRs only occur when the magnetic field is aligned within a few degrees to the current flowing direction and become most pronounced at $H\ //I$, akin to those attributed to chiral anomaly [16,21]. However, the temperature dependence of the NLMR in our quantum wells, as shown in Figure 5.4 for Sample 1b, differs significantly from those reported in literature, where NLMR diminishes monotonically with increasing temperature [16,21,32,33]. In contrast, the NLMR in our GaAs quantum wells shows a non-monotonic temperature behavior and becomes most pronounced at ~170 K. As discussed below, this difference can be understood with the existence of two types of microscopic disorders in quantum wells. In addition to the conventional microscopic disorder due to impurity and lattice

defects that is relevant at low temperatures, the interface roughness of a quantum well or the random distribution of the Si dopants may also induce NLMRs at high temperatures.

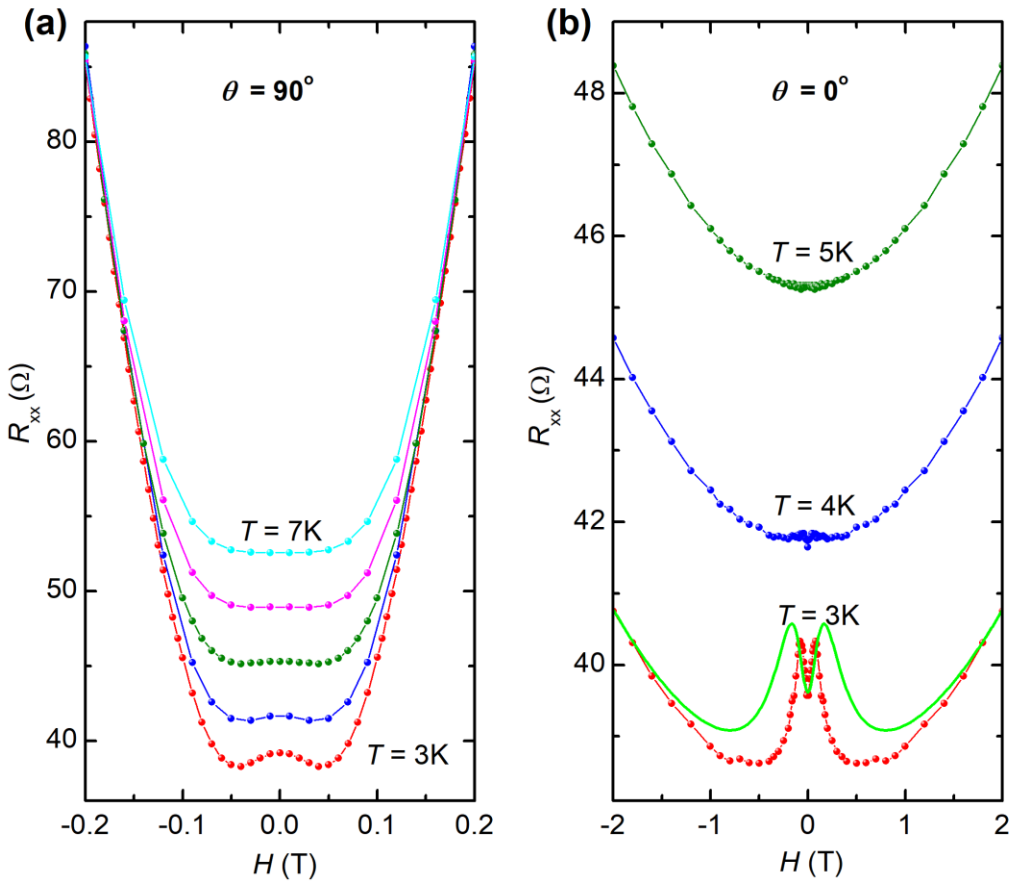

Figure 5.2 | Negative magnetoresistances in Sample 1b at liquid helium temperatures. (a), at $H \perp I$, **(b)**, at $H // I$. The green and purple curves in (**b**) are derived from Eq. (5.2) and Eq. (5.3), respectively.

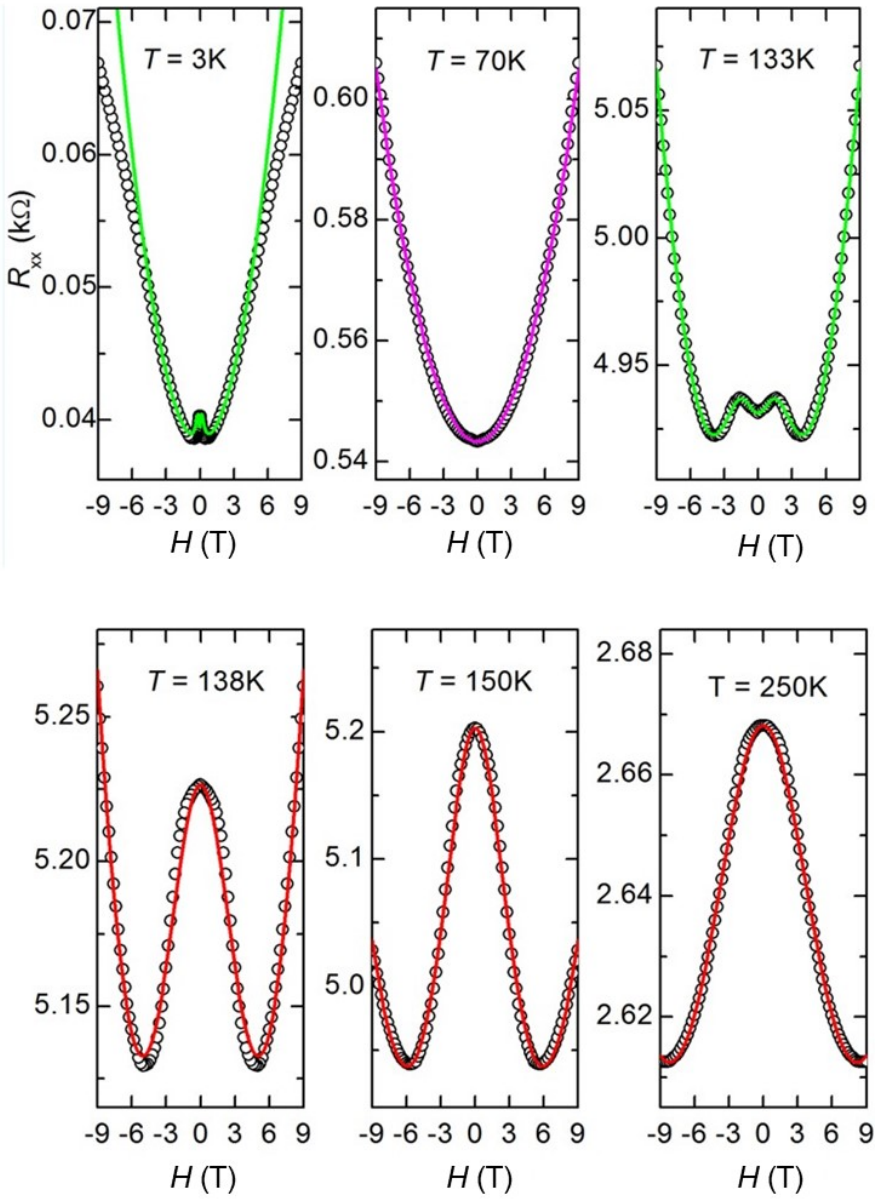

Figure 5.3 | Representative *R*(*H*) curves showing evolution of the MR feature with temperature. Symbols are experimental data; green lines are fits to the data at T = 133 K and 3 K using Eq. (5.2) with values of the five variables of $\varepsilon_d = 0.727$, $\gamma_d = 0.295$, $\alpha = 0.148$ T^{-2}, $\beta^s = 6.83\times10^{-4}$ T^{-2}, and $\beta^p = 0.12$ T^{-2} and $\varepsilon_d = 0.818$, $\gamma_d = 0.21$, $\alpha = 20$ T^{-2}, $\beta^s = 0.016$ T^{-2}, and $\beta^p = 35$ T^{-2}, respectively; red lines (for T = 250 K, 150 K and 138 K) are fits with the reduced form of Eq. (5.2) for the serial scenario, with fitting parameters presented in Figure 5.13, and the magenta line (for T = 70 K) describes a quadratic magnetic field dependence $R(H) = R_0(1+\beta H^2)$ with $\beta = 1.4\times10^{-3}$ T^{-2} and the measured $R_0 = 543.4$ Ω.

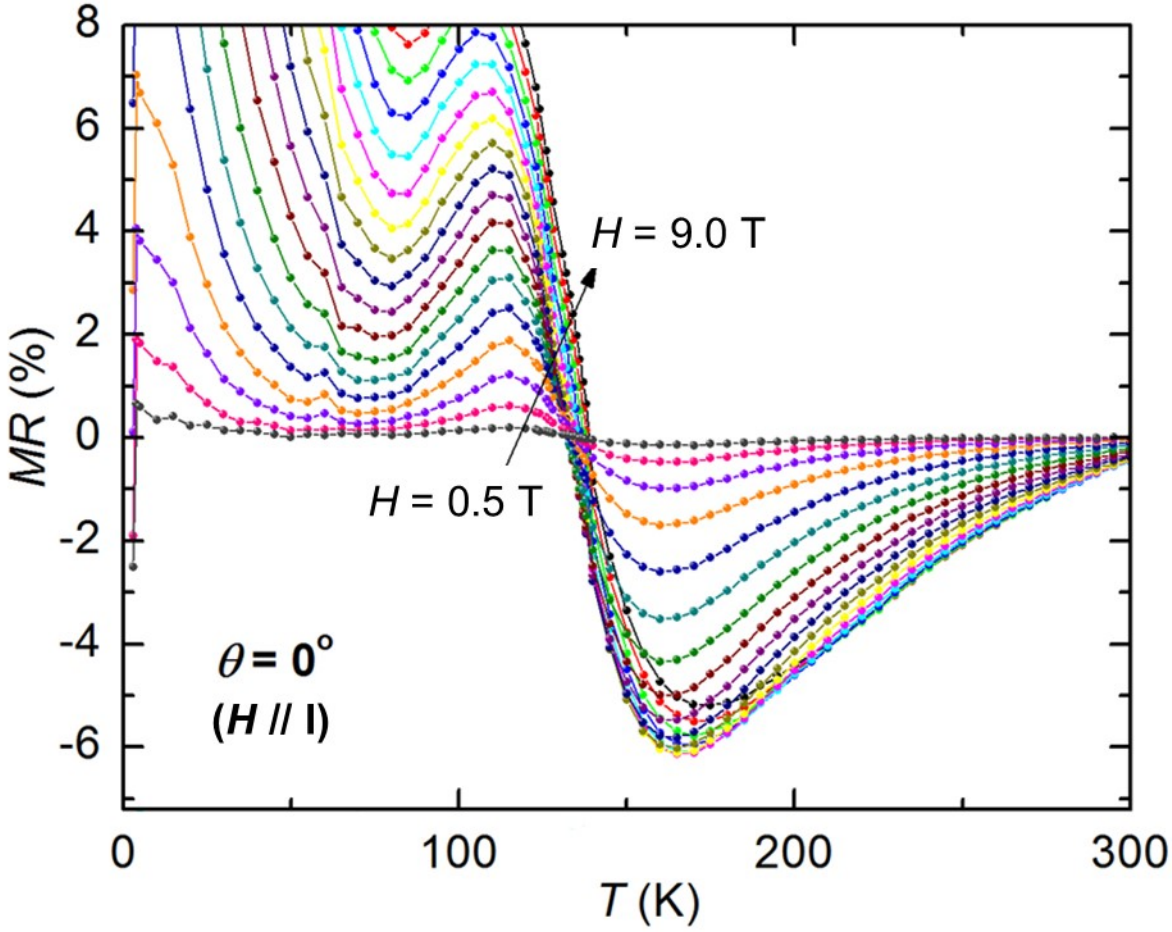

Figure 5.4 | Temperature dependence of the magnetoresistance. Magnetic fields change from $H = 0.5$ T to $H = 9.0$ T at intervals of 0.5 T at H //I, where $MR = [R(H)\text{-}R_0]/R_0$ with R_0 being the longitudinal resistance R_{xx} at zero field.

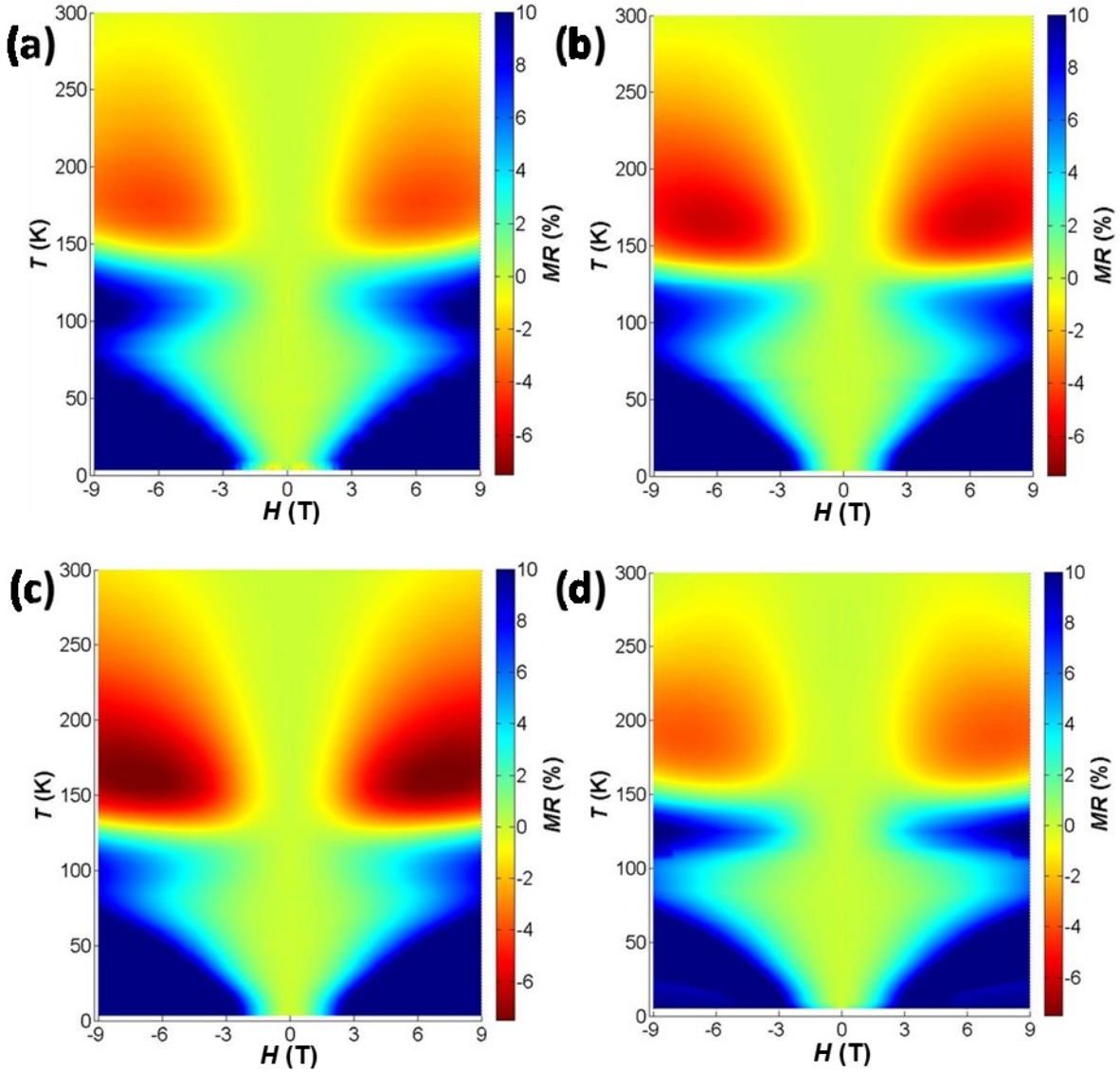

Figure 5.5 | Color maps for the longitudinal magnetoresistances in all four samples. (**a**) Sample 1a, (**b**), Sample 1b, (**c**), and Sample 1c, and (**d**) Sample 2.

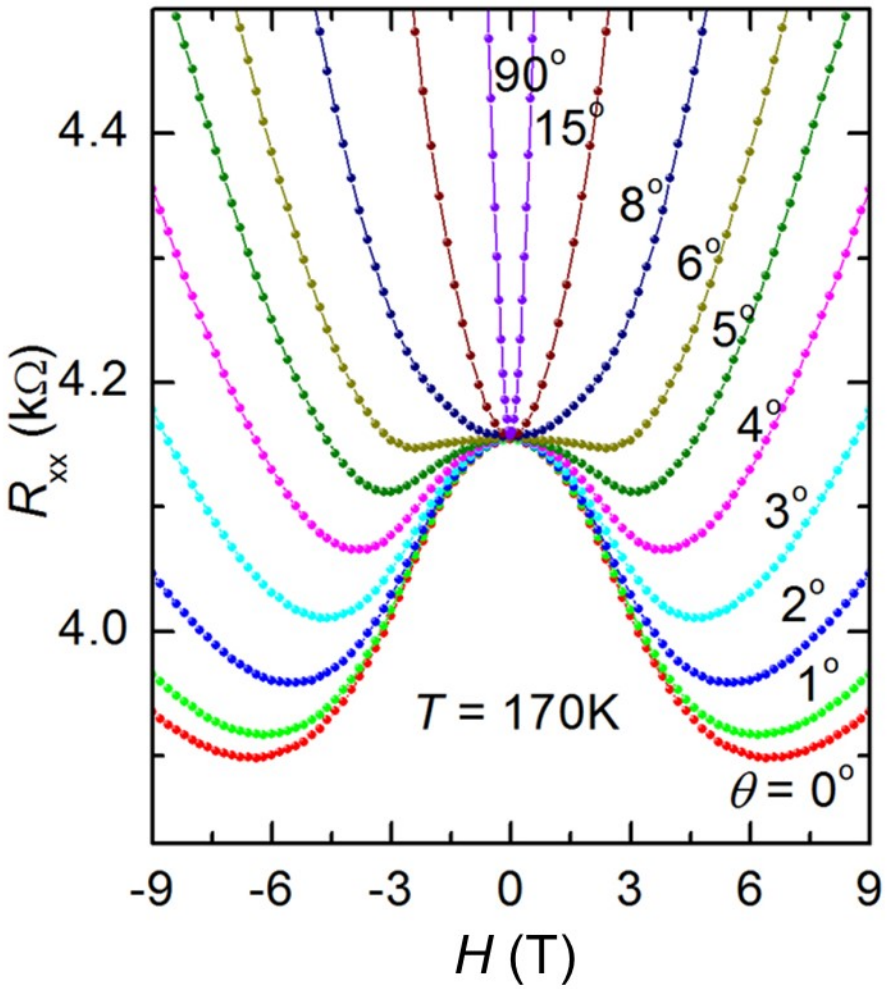

Figure 5.6 | Magnetic field dependence of the resistance *R*(*H*) at various field orientations. Negative magnetoresistance can be clearly seen at $\theta \leq 6°$.

5.2. Microscopic disorder

Since the samples are in a standard Hall-bar geometry defined through photolithographic patterning and the current contacts are far away from the voltage probes, the NLMRs observed here are unlikely to be artifacts arising from non-uniform current injection [131,133]. In general, artifacts become more pronounced with increasing mobility and thus can be excluded with the non-monotonic temperature behavior of the observed NLMRs, which differs from the monotonic temperature dependence of the mobility (see Figure 5.7b and Figure 5.8d). The quantum wells are of very high quality, as demonstrated by the Shubnikov-de Haas quantum oscillations at T = 3 K (see Figure 5.9). Their mobility can be larger than 3×10^6 $cm^2V^{-1}s^{-1}$ at T = 3 K and reach as high as 1.4×10^4 $cm^2V^{-1}s^{-1}$ even at room temperature (see Figure 5.8d). Therefore, macroscopic defects such as exotic phases and grain boundaries cannot be the origin of NLMRs in the quantum wells.

Computer simulations for polycrystalline $Ag_{2\pm x}Se$ samples [125,126] have demonstrated that macroscopic disorder such as microscale clusters of excessive Ag induces distorted current paths, resulting in NLMRs. Similarly, the current paths in areas with microscopic disorder are expected to be distorted due to local conductivity fluctuation. Thus, I postulate that the disordered areas where the current paths are distorted in quantum wells have positive (negative) longitudinal magnetoconductances (magnetoresistances). Considering that a quadratic field dependence of the magnetoconductance is the most common relationship revealed by experiments and theories to describe NLMRs, I assume that the magnetotransport behavior of the disordered areas to be $R_d(H) = R_{d0}/(1 + \alpha H^2)$, where R_{d0} is the resistance of the disordered

areas at zero magnetic field. For the magnetoresistance of the clean areas where the current paths are not distorted, I take the conventional Drude form $R_c(H) = R_{c0}(1 + \beta H^2)$ [62]. Figure 5.10b presents schematics for the expected *R*(H) relationship for these two scenarios.

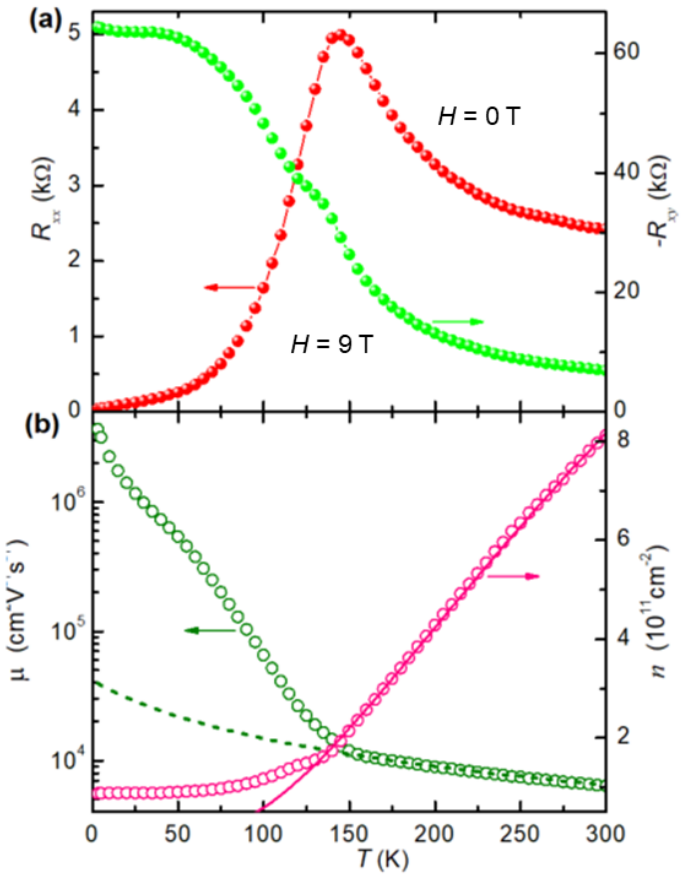

Figure 5.7 | Electron density and mobility of Sample 1b. (**a**), Temperature dependence of the zero-field resistance and the Hall resistance at H = 9 T and θ = 90°. (**b**), Corresponding electron density and mobility. The electron densities n in (**b**) are calculated from the Hall resistances R_{xy} in (**a**) through the relationship $R_{xy} = H/ne$. The mobilities μ in (**b**) are derived from the zero-field resistances $\rho_0 = R_{xx}(0T)L_y/L_x$ in (**a**) and the electron densities in (**b**) through the relationship $\rho_0 = 1/ne\mu$. The solid red line in (**b**) is a fit of $n \sim \exp(-E_A/k_BT)$, with k_B the Boltzmann constant and E_A = 34.05 meV. The dotted olive line in (**b**) describes a temperature dependence of the electron mobility $\mu = 2.3\times10^6/(55+T)$ ($cm^2V^{-1}s^{-1}$).

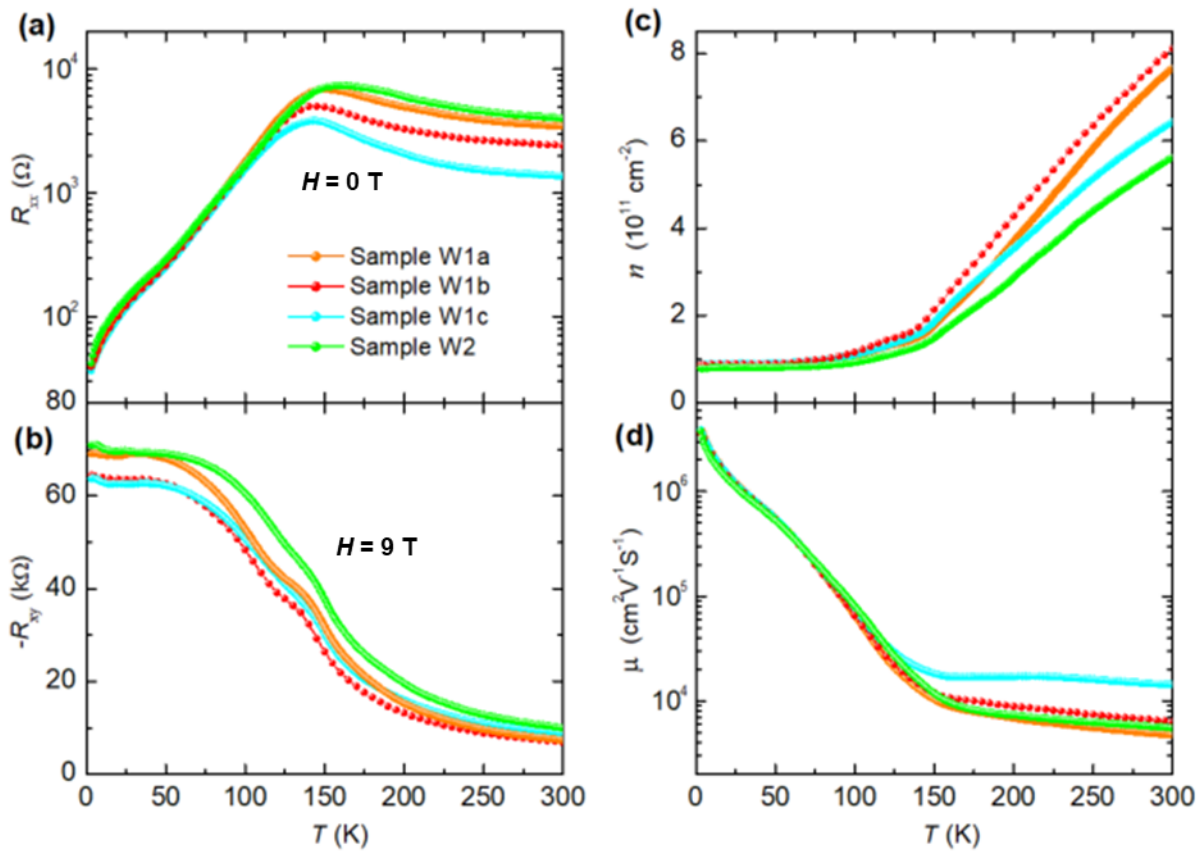

Figure 5.8 | Basic characterizations of the measured samples. (**a**), (**b**), (**c**), and (**d**) show the temperature dependence of the zero-field resistance, the Hall resistance at $H = 9$ T, the electron density and mobility respectively. The electron densities n in (**c**) is calculated from the Hall resistances R_{xy} in (**b**) through the relationship $R_{xy} = H/ne$. The mobility μ in (**d**) is derived from the zero-field resistances $R_{xx}(0T)$ in (**a**) and the electron densities in (**c**) through the relationship $R_{xx}(0T) = 1/ne\mu$.

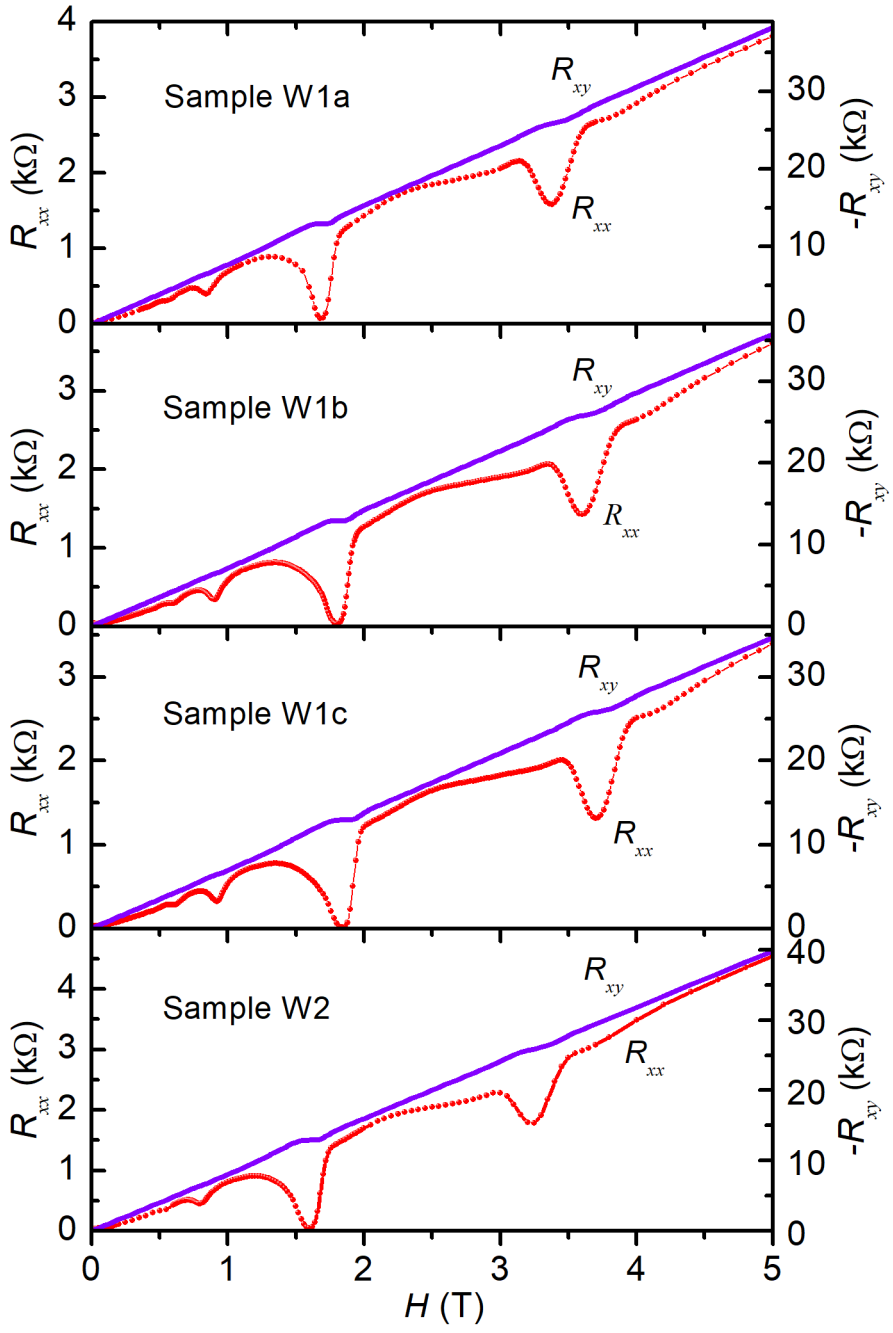

Figure 5.9 | Shubnikov-de Haas quantum oscillations and quantum Hall effect. Data were taken at $T = 3$ K and in magnetic fields perpendicular to the quantum well plane. For clarity data only up to $H = 5$ T are presented in the figure.

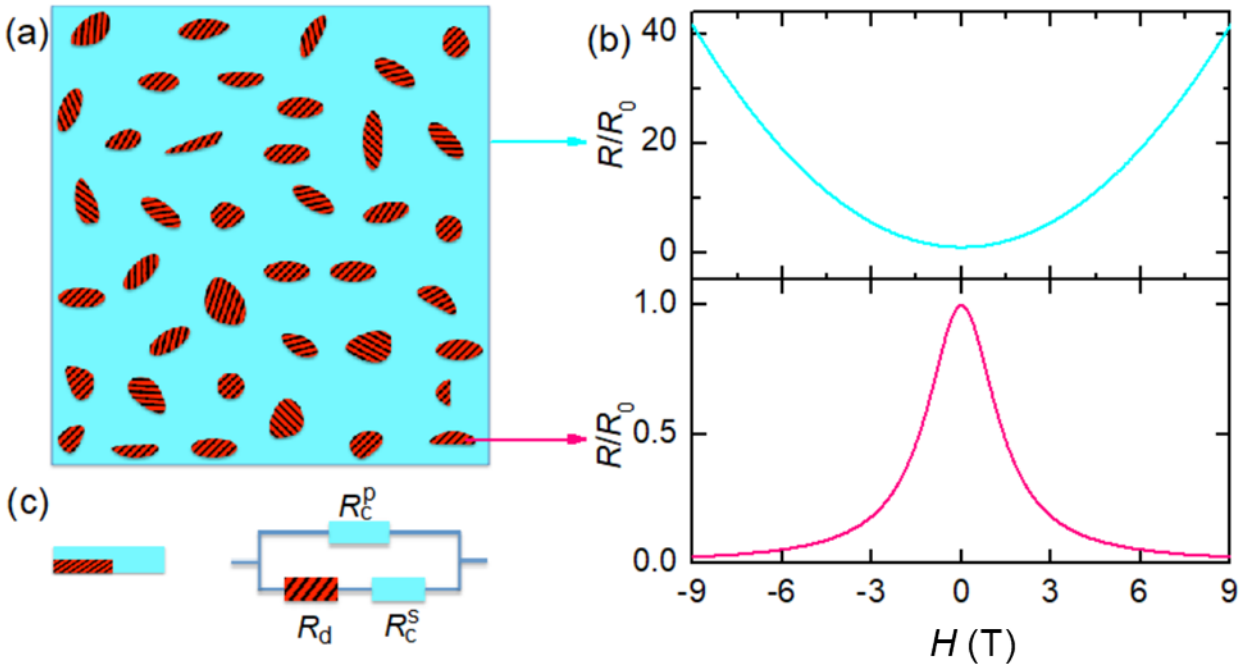

Figure 5.10 | Phenomenological three-resistor model. (**a**), Schematic describing a sample containing areas (red and shaded) where the current paths are distorted and clean areas (cyan) where the current paths are not distorted. (**b**), Hypothesized magnetic field dependences of the resistance for the clean (upper panel, $R/R_0 = 1+\alpha H^2$) and disordered regions (lower panel, $R/R_0 = 1/(1+\beta H^2)$ where $\alpha = \beta = 0.5$ T^{-2} are used for the calculations. **c,** Simplified picture for electrotransport in the sample (left panel) and the equivalent circuit (right panel).

5.2.1. Linear magnetoresistance and quantum Hall plateaus

Both experiments [125,126] and simulations [125,126,136] reveal that (quasi-)linear MRs at H⊥I can appear in polycrystalline materials where NLMRs are detected. As presented in Figure 5.11a for sample 1b at T = 170 K and various magnetic field orientations, our quantum wells also exhibit (quasi-)linear MRs at $H \perp I$ and NLMRs at $H \,//I$. Furthermore, the linearity of the MRs for $H \perp I$ becomes more pronounced as the NLMRs for $H \,//I$ increase, as demonstrated by the $R(H)$ curves obtained at various temperatures shown in Figure 5.11b. The observation of (quasi-)linear MR at $H \perp I$ further attests to the role of disorder on the magnetotransport of our quantum wells. On the other hand, it is known that microscopic disorder plays a crucial role in the occurrence of quantum Hall plateaus [134], which is observed in all of our quantum wells (see Figure 5.9). That is, areas with microscopic disorder exist in the quantum wells alongside with clean areas (see Figure 5.10a for a schematic).

I note that the co-existence of disordered and clean areas may not necessarily lead to NLMRs. As demonstrated in Figure 5.5c for the R(H) curves obtained at T = 105 K, the MR at $H \,//I$ can be positive and even quasi-linear. In this case, (quasi-)linear MRs may occur for all field orientations.

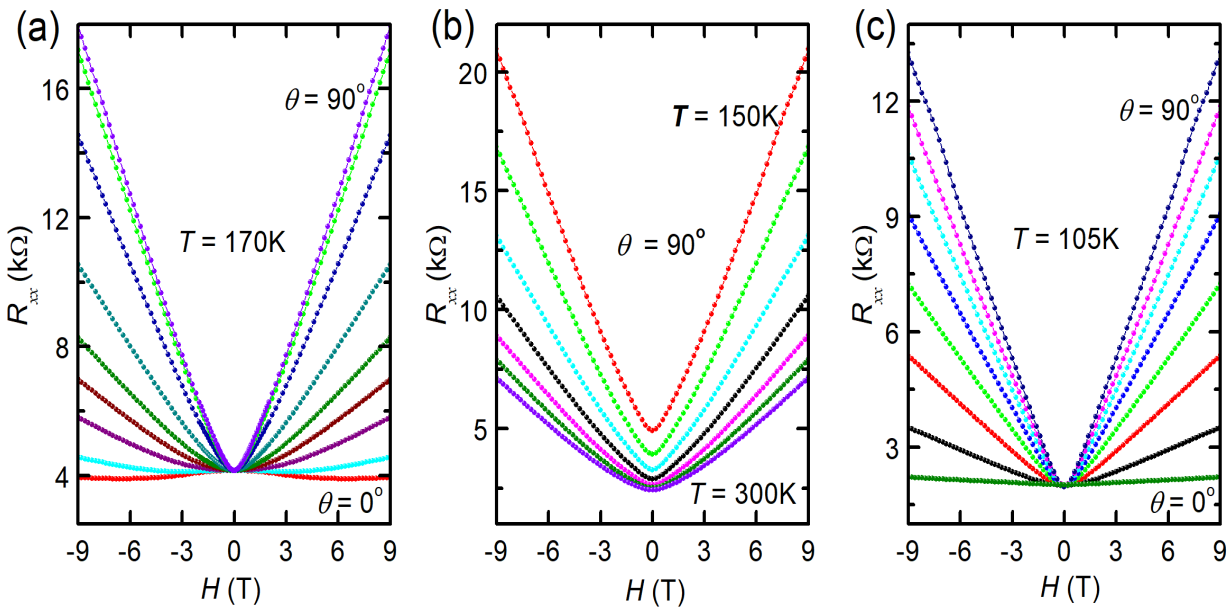

Figure 5.11 | Linear magnetoresistances (MR) due to distorted current paths. (**a**), $R(H)$ curves at $T = 170$ K and various magnetic field orientations. Quasi-linear MRs can be seen at high angles. (**b**), $R(H)$ curves at $\theta = 90°$ ($H \perp I$) and temperatures from 150 K to 300K at intervals of 25 K. Linearity of the MRs becomes more pronounced with decreasing temperatures at which NLMRs are larger. (**c**), $R(H)$ curves at $T = 105$ K and various angles, showing linear MRs in all magnetic field orientations.

5.2.2. Three-resistor model

The above observed quantum Hall plateaus and (quasi-) linear magnetoresistance ensured the microscopic disorder exist in the quantum wells alongside with clean areas, which allow me to use a phenomenological three-resistor model to qualitatively account for the various magnetic field behaviors of the observed NLMRs. For a sample with disordered areas mostly surrounded by clean areas (see a schematic in Figure 5.10a), its R(H) behavior can be evaluated using a simplified equivalent circuit consisting of three resistors (see Figure 5.10c), i.e., a resistor R_c^p with positive MR (representing the clean areas) in parallel with two resistors R_d and R_c^s that are in series and have opposite MRs, where R_d and R_c^s are the resistances of the disordered and clean areas, respectively. The superscripts *s* and *p* denote the cases of the clean area in serial with and in parallel to the disordered area. In this case the $R(H)$ behavior can be described as

$$R(\mathrm{H}) = [1/(R_d + R_c^s) + 1/R_c^p]^{-1} \tag{5.1}$$

Since each of $R_d, R_c^s,$ and R_c^p has two variables, Eq. (5.1) has six free parameters. In order to improve the reliability of the analysis, I can take advantage of the measured zero-field resistance by rewriting Eq. (5.1) as

$$R(H) = R_0\{\varepsilon_d/[\gamma_d/(1+\alpha H^2) + (1-\gamma_d)(1+\beta^s H^2)] + (1-\varepsilon_d)/(1+\beta^p H^2)\}^{-1} \tag{5.2}$$

where $R_0 = [1/(R_{d0} + R_{c0}^s) + 1/R_{c0}^p]^{-1}$ is the measured zero-field resistance, $\varepsilon_d = R_{c0}^p/(R_{c0}^p + R_{d0} + R_{c0}^s)$ is the ratio of the conductance of the channel with disordered area to

the total value at zero-field and $\gamma_d = R_{d0}/(R_{d0} + R_{c0}^s)$ is the ratio of the zero-field resistance of the disordered area to the corresponding total value of the channel consisting of the disordered and clean areas in series.

I use Eq. (5.2) to account for the experimental $R(H)$ curves as presented in Figure 5.3 as solid curves. I found that all five fitting parameters are necessary to describe $R(H)$ curves with positive MR near zero-field, like those obtained at T = 3 K and 133 K, resulting in large uncertainty in the analysis. Numerical results in Figure 5.12 indicate that R_c^p is the contributor for the positive MR near zero-field (see Figure 5.12 c) and the experimental $R(H)$ curves at $T \geq$ 138 K in Figure 5.3 follow the NLMR behavior modelled with an equivalent circuit with R_d and R_c^s in series (see Figure 5.12b). In this scenario, $\varepsilon_d = 1$, reducing Eq. (5.2) to $R(H) = R_0[\gamma_d/(1 + \alpha H^2) + (1 - \gamma_d)(1 + \beta^s H^2)]$. Using the experimentally determined R_0, this simplification decreases the number of variables to three (γ_d, α, and β^s). This simple serial scenario accounts for the experimental data very well, as demonstrated in Figure 5.3 for T = 138 K, 150 K and 250 K. Figure 5.13 shows the temperature dependence of the derived γ_d, α, and β^s. It is reasonable for α and β^s to increase with decreasing temperature, since they should reflect the temperature behavior of the electron mobility (see Figure 5.7b). The combined effect of γ_d, α, and β^s leads to an enhanced NLMR with decreasing temperature. Between 150 K and 160 K, however, the NLMRs as well as γ_d, α, and β^s change their temperature behavior, resulting in minima in the NLMR versus temperature curves (see Figure 5.4) and peaks in those of the three fitting parameters.

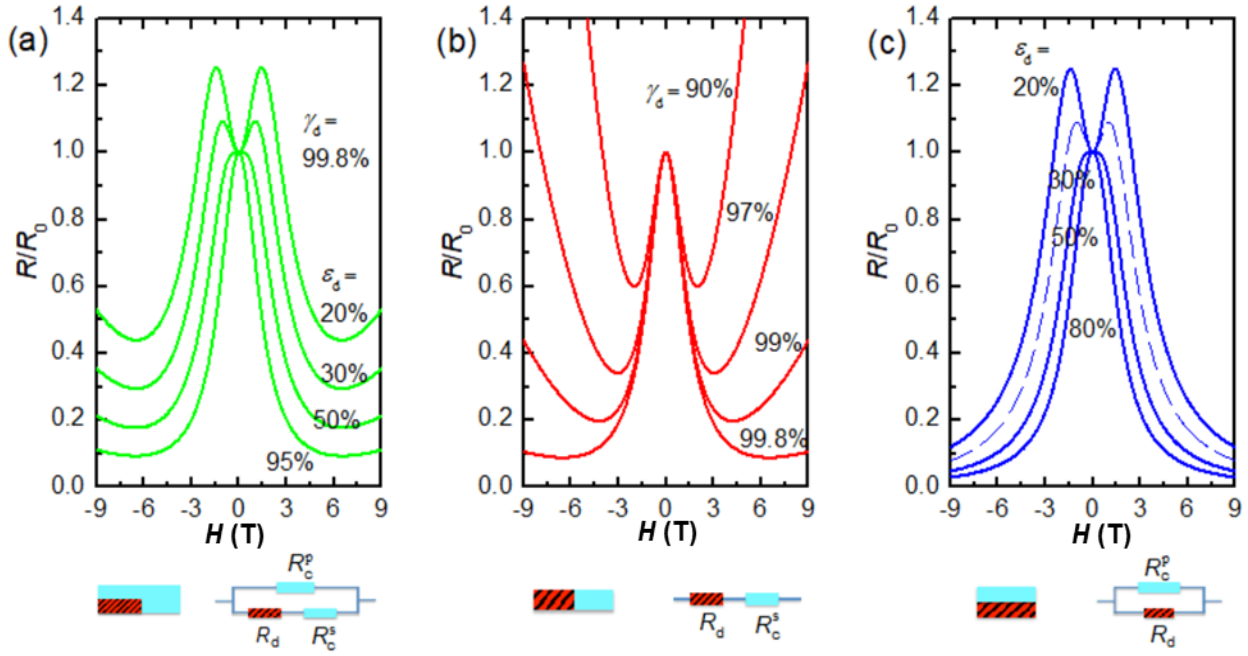

Figure 5.12 | Numerical results from the phenomenological model. Characteristic features of NLMRs in various scenarios of disorder distribution were revealed. **(a)**, the general case that requires all three resistors (R_d, R_c^p and R_c^s) in the equivalent circuit, which describes samples with dispersed distribution of the disordered areas. **(b)**, a simpler scenario that only requires an equivalent circuit of R_d and R_c^s in series, which represents samples with connected disordered areas across the sample in the direction perpendicular to the current. (**c**), a simpler scenario that can be described with R_d and R_c^p in parallel, which represents samples with connected disordered areas across the sample in the direction parallel to the current. The schematics and corresponding equivalent circuits are given at the bottom of each panel.

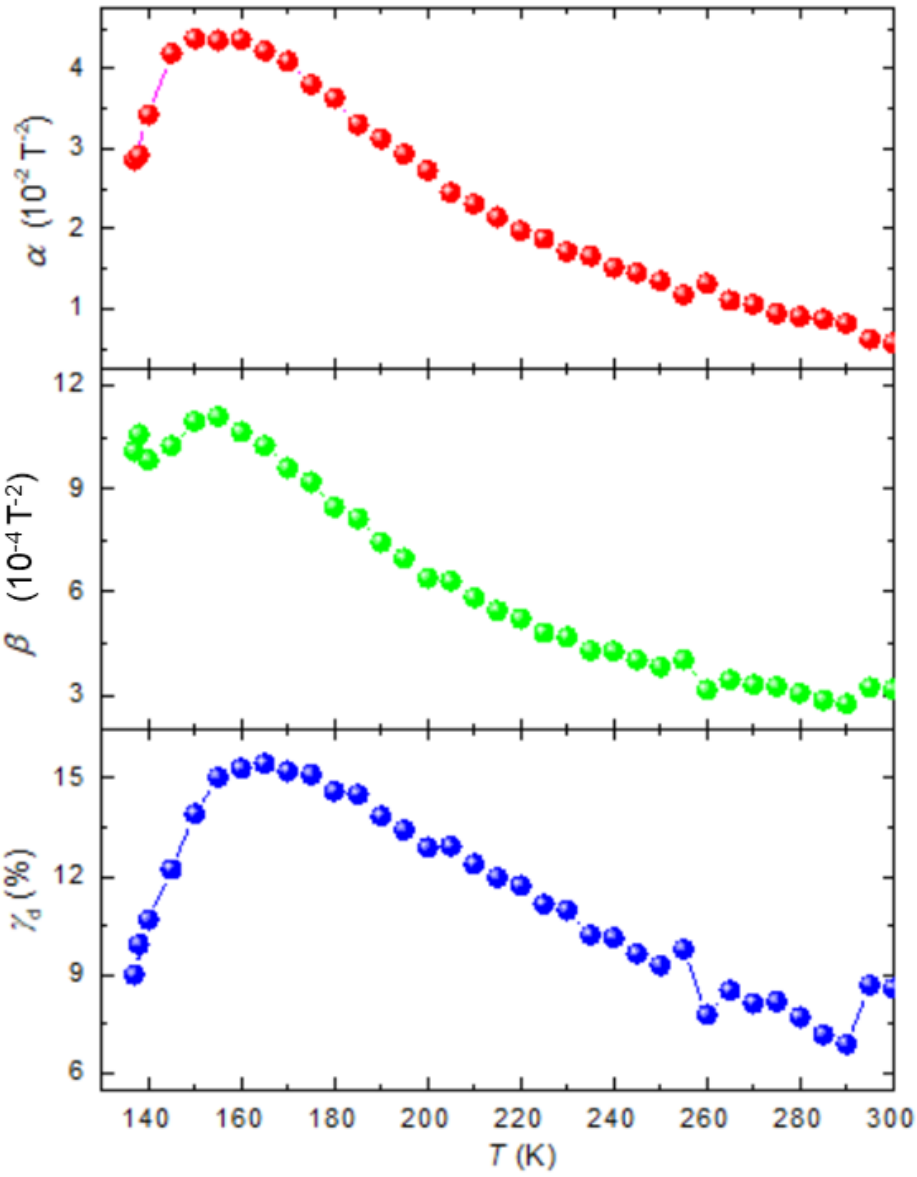

Figure 5.13 | Temperature dependence of the derived parameters. From the fitting result by using Eq. (5.2). α, β^s and γ_d are defined in the text.

I note that the change in the temperature behavior of NLMRs as well as γ_d, α, and β^s coincides with a transition (at $T_p \sim 145$ K) from semiconducting-like to metallic temperature dependence in the zero-field $R_0(T)$ curve and a kink in the R_{xy} curve at $H = 9$ T (see Figure 5.7a). As shown in Figure 5.7b, the temperature dependences of both the electron mobility and density also change significantly at 140 K-150 K. Quantitatively, the temperature dependence of the electron density for Sample 1b at $T > 140$ K can be well described with $n = N_0 \exp(-E_A/k_B T)$, with k_B the Boltzmann constant, $N_0 = 3.05\times10^{12}$ cm^{-2}, and $E_A \approx 34$ meV (see Table 5.1 for $N_0 s$ and E_As of other samples). This value is consistent with the intersubband activation energy ($E_{21} \approx$ 30 meV) for a 40 nm thick GaAs quantum well. On the other hand, the E_A value falls in the range of the Si activation energy of 6-200 meV, depending on the content of Al in the $Al_xGa_{1-x}As$ layer ($x = 0 - 0.33$) [137]. Furthermore, the value of N_0 is close to the total Si density of 5.1×10^{12} cm^{-2}. That is, the transport at high temperatures could be determined by intersubbands of the quantum wells or the Si doped layers.

5.2.3. Potential application of the three-resistor model

The phenomenological three-resistor model and Eq. (5.2) can be readily applied to account for the NLMRs in films of other materials, in which both micro- and macroscopic disorders are present. The longitudinal magnetoconductance σ_{xx} in thin films of topological insulator Bi_2Se_3 [32] is found to follow $\sigma_{xx} \sim H^2$ in magnetic fields up to 30 T, indicating that the entire sample is disordered. The behavior of NLMRs in films of Dirac semimetal Cd_3As_2 is thickness-dependent [33], with various types of $R(B)$ relationship resembling those in Figure 5.12. In the

scenario of Figure 5.12c for a parallel equivalent circuit, Eq. (5.2) can be re-written as $\sigma(H) = \sigma_{d0}(1 + \alpha H^2) + \sigma_{c0}/(1 + \beta^p H^2)$, which is exactly the same equation used in the analysis of the data for the 370 nm thick Cd_3As_2 film [33]. On the other hand, the two thinner samples (with thicknesses of 85 nm and 120 nm) exhibit similar type of NLMRs to the quantum wells (of 40 nm thick) at high temperatures, which can be described with the reduced form of Eq. (5.2) for a series equivalent circuit (see Figure 5.12b). For films of intermediate thicknesses (170 nm and 340 nm), Eq. (5.2) with all three resistors (see Figure 5.12a) is required to account for the observed NLMRs.

Recently reported NLMRs in single crystals were often attributed to chiral anomaly. In quantitative analyses [27,65], possible weak anti-localization conductance σ_{WAL} and conventional Fermi surface contribution σ_N were also included to account for the deviation from quadratic field dependence of the conductance, leading to

$$\sigma(\mathrm{H}) = \sigma_{WAL}(1 + C_W H^2) + \sigma_N \tag{5.3}$$

with the positive constant C_W reflecting the contribution from chiral anomaly and $\sigma_{WAL} = aH^{1/2} + \sigma_0$ with $a < 0$ and $\sigma_N^{-1} = \rho_0 + bH^2$. Such a $\sigma(\mathrm{H})$ expression with five variables could elucidate the experimental data at low magnetic fields [27,65]. Since weak anti-localization may also exist in quantum wells at low temperatures, I applied Eq. (5.3) to analyze the data obtained at 3 K and the result is given in Figure 5.2b. With four fitting parameters ($a = 1.98 \times 10^{-3}$ T^{-2}, $\sigma_0^{wal} = 2.06 \times 10^{-3}$ Ω, $C_W = 59.84$ T^{-2}, $b = 87.21$ T^{-2}) and the measured zero-field resistivity ρ_0 (= 19.81 Ω) (which gives $\rho_0^N = 1/\rho_0 - \sigma_0^{wal} = 4.84 \times 10^{-2}$ Ω), Eq. (5.3) can indeed describe the

results at low magnetic fields (H < 0.5 T) well and also produces a upturn of the MR at high magnetic fields. When I set $C_W = 0$ for the non-Weyl quantum well, however, Eq. (5.3) is reduced to $\sigma(H) = \sigma_{WAL} + \sigma_N$, which produces only positive MR because both σ_{WAL} and σ_N decrease with increasing magnetic field. Thus, Eq. (5.3) is invalid for a non-Weyl system. For an estimate, I also used Eq. (5.3) to reveal possible contribution of weak localization by allowing $a > 0$. However, Eq. (5.3) cannot describe the experimental data even at low magnetic fields if I set $C_W = 0$. Thus, weak localization should not be the dominant contributor to the observed NLMRs at low temperatures.

5.3. Discussion and conclusion

My results revealed that linear MRs and NLMRs can co-exist. Thus, NLMRs can be used to distinguish disorder based origins from other mechanisms [138-141] for linear MRs. On the other hand, (quasi-)linear MRs for $H \perp I$ could be an indicator of the existence of NLMRs, providing a guidance in the search for materials with NLMRs. As demonstrated in disorder-dominated polycrystalline samples [142], my discovery of the role of microscopic disorder on the occurrence of NLMRs and linear MRs will stimulate more work to tune the magnetotransport properties of single crystals through microscopic disorder engineering, e.g., doping [27,31] and irradiations with light charge particles such as protons [143] and electrons [144].

On the other hand, the results of this work suggest that one should be very cautious when associating the origin of experimentally observed NLMR with the chiral anomaly of Weyl materials.

6. Summary

In this dissertation research, I explored various types of intriguing MR behaviors by using magnetotransport measurement. Different from the positive and small MR in metals, I observed an XMR in the rare-earth monopnictides YSb and LaSb, a large saturating MR in Weyl semimetal NbP, and a NLMR in GaAs quantum wells.

I determined the ratio of the electron and hole density in YSb and LaSb through angle-dependent SdH oscillation experiments. From both experimental results and theoretical analysis using a semi-classic isotropic two-band model, I revealed that a nearly perfect compensation of the e-h concentrations is an important factor for the LaSb and YSb to exhibit the XMR.

In the measurements of Weyl semimetal NbP, I observed both non-saturating XMR and saturating large MR behaviors at high and low temperature regions, respectively. Noticing a rapid increase in the Hall resistivity when the saturating XMR behavior occurs, I explored the relation between the Hall effect and the MR behaviors at different temperatures. With the help of an experimentally determinable parameter - the Hall factor, I found that MR can have a saturating behavior in the presence of strong Hall effect. Based on those experimental results, I attributed the origin of the non-saturating XMR behavior to electron-hole compensation and high mobility of the charge carriers as well as diminishing Hall factors.

Furthermore, I explored another exotic MR behavior - the NLMR phenomenon. I observed pronounced negative MRs in GaAs quantum wells when the magnetic field and current are

parallel to each other. The NLMR can have monotonic and non-monotonic magnetic field dependences, depending on the temperature. I attributed the origin of the NLMR in the quantum wells to the current distortion induced by microscopic disorder. Also, I successfully described the various MR behaviors by using a phenomenological three-resistor model.

In summary, this dissertation aimed to uncovering the origin of two types of intriguing MR behaviors – the XMR and NLMR. The rich fundamental physics and potential applications of the studied MR phenomena can stimulate future research.

References

[1] J. Ziman and P. W. Levy, Physics Today **14**, 64 (1961).
[2] P. Ripka and M. Janosek, IEEE Sensors Journal **10**, 1108 (2010).
[3] S. A. Wolf, D. D. Awschalom, R. A. Buhrman, J. M. Daughton, S. von Molnár, M. L. Roukes, A. Y. Chtchelkanova, and D. M. Treger, Science **294**, 1488 (2001).
[4] J. M. Daughton, Journal of Magnetism and Magnetic Materials **192**, 334 (1999).
[5] R. Xu, A. Husmann, T. F. Rosenbaum, M. L. Saboungi, J. E. Enderby, and P. B. Littlewood, Nature **390**, 57 (1997).
[6] F. Y. Yang, K. Liu, K. Hong, D. H. Reich, P. C. Searson, and C. L. Chien, Science **284**, 1335 (1999).
[7] Y. Kopelevich, J. H. S. Torres, R. R. da Silva, F. Mrowka, H. Kempa, and P. Esquinazi, Physical Review Letters **90**, 156402 (2003).
[8] X. Du, S.-W. Tsai, D. L. Maslov, and A. F. Hebard, Physical Review Letters **94**, 166601 (2005).
[9] E. Mun, H. Ko, G. J. Miller, G. D. Samolyuk, S. L. Bud'ko, and P. C. Canfield, Physical Review B **85**, 035135 (2012).
[10] H. Takatsu, J. J. Ishikawa, S. Yonezawa, H. Yoshino, T. Shishidou, T. Oguchi, K. Murata, and Y. Maeno, Physical Review Letters **111**, 056601 (2013).
[11] K. Wang, D. Graf, L. Li, L. Wang, and C. Petrovic, Scientific Reports **4**, 7328 (2014).
[12] M. N. Ali *et al.*, Nature **514**, 205 (2014).
[13] M. N. Ali, L. Schoop, J. Xiong, S. Flynn, Q. Gibson, M. Hirschberger, N. Ong, and R. Cava, EPL (Europhysics Letters) **110**, 67002 (2015).
[14] Y. Zhao *et al.*, Physical Review B **92**, 041104 (2015).
[15] T. Liang, Q. Gibson, M. N. Ali, M. Liu, R. J. Cava, and N. P. Ong, Nature Materials **14**, 280 (2014).
[16] J. Xiong, S. K. Kushwaha, T. Liang, J. W. Krizan, M. Hirschberger, W. Wang, R. J. Cava, and N. P. Ong, Science **350**, 413 (2015).
[17] Y. Zhao *et al.*, Physical Review X **5**, 031037 (2015).
[18] C. Shekhar *et al.*, Nature Physics **11**, 645 (2015).
[19] Z. Wang *et al.*, Physical Review B **93**, 121112 (2016).
[20] N. J. Ghimire, L. Yongkang, M. Neupane, D. J. Williams, E. D. Bauer, and F. Ronning, Journal of Physics: Condensed Matter **27**, 152201 (2015).
[21] X. Huang *et al.*, Physical Review X **5**, 031023 (2015).
[22] Q. Li *et al.*, Nature Physics **12**, 550 (2016).
[23] G. Zheng *et al.*, Physical Review B **93**, 115414 (2016).
[24] C.-L. Zhang *et al.*, Nature Communications **7**, 10735 (2016).
[25] L.-X. Wang, C.-Z. Li, D.-P. Yu, and Z.-M. Liao, Nature Communications **7**, 10769 (2016).
[26] H. Wang *et al.*, Physical Review B **93**, 165127 (2016).
[27] Y.-Y. Lv *et al.*, Physical Review Letters **118**, 096603 (2017).
[28] J. Gooth *et al.*, Nature **547**, 324 (2017).
[29] F. Arnold *et al.*, Nature Communications **7**, 11615 (2016).

[30] P. Li *et al.*, Nature Communications **8**, 2150 (2017).
[31] Z. Wang *et al.*, Nature Communications **9**, 47 (2018).
[32] S. Wiedmann *et al.*, Physical Review B **94**, 081302 (2016).
[33] T. Schumann, M. Goyal, D. A. Kealhofer, and S. Stemmer, Physical Review B **95**, 241113 (2017).
[34] O. Breunig, Z. Wang, A. A. Taskin, J. Lux, A. Rosch, and Y. Ando, Nature Communications **8**, 15545 (2017).
[35] A. P. Ramirez, R. J. Cava, and J. Krajewski, Nature **386**, 156 (1997).
[36] B. A. Bernevig and S.-C. Zhang, Physical review letters **96**, 106802 (2006).
[37] X.-L. Qi and S.-C. Zhang, arXiv preprint arXiv:1001.1602 (2010).
[38] Y. Wu *et al.*, Nature Physics **12**, 667 (2016).
[39] Y. Wu, D. Mou, N. H. Jo, K. Sun, L. Huang, S. L. Bud'ko, P. C. Canfield, and A. Kaminski, Physical Review B **94**, 121113 (2016).
[40] F. F. Tafti, Q. Gibson, S. Kushwaha, J. W. Krizan, N. Haldolaarachchige, and R. J. Cava, Proceedings of the National Academy of Sciences, 201607319 (2016).
[41] F. F. Tafti, Q. D. Gibson, S. K. Kushwaha, N. Haldolaarachchige, and R. J. Cava, Nature Physics **12**, 272 (2015).
[42] P.-J. Guo, H.-C. Yang, B.-J. Zhang, K. Liu, and Z.-Y. Lu, Physical Review B **93**, 235142 (2016).
[43] N. Kumar, C. Shekhar, S.-C. Wu, I. Leermakers, O. Young, U. Zeitler, B. Yan, and C. Felser, Physical Review B **93**, 241106 (2016).
[44] N. Kumar, C. Shekhar, J. Klotz, J. Wosnitza, and C. Felser, Physical Review B **96**, 161103 (2017).
[45] S. Shanshan, W. Qi, G. Peng-Jie, L. Kai, and L. Hechang, New Journal of Physics **18**, 082002 (2016).
[46] X. H. Niu *et al.*, Physical Review B **94**, 165163 (2016).
[47] J. Nayak *et al.*, Nature Communications **8**, 13942 (2017).
[48] Y. Wu *et al.*, Physical Review B **94**, 081108 (2016).
[49] L. K. Zeng *et al.*, Physical Review Letters **117**, 127204 (2016).
[50] N. J. Ghimire, A. S. Botana, D. Phelan, H. Zheng, and J. F. Mitchell, Journal of Physics: Condensed Matter **28**, 235601 (2016).
[51] Y. Qiao-He, W. Yi-Yan, L. Rui, G. Peng-Jie, X. Sheng, L. Kai, W. Shancai, and X. Tian-Long, EPL (Europhysics Letters) **119**, 17002 (2017).
[52] O. Pavlosiuk, P. Swatek, and P. Wiśniewski, Scientific Reports **6**, 38691 (2016).
[53] J. He *et al.*, Physical Review Letters **117**, 267201 (2016).
[54] J. Xu, N. J. Ghimire, J. S. Jiang, Z. L. Xiao, A. S. Botana, Y. L. Wang, Y. Hao, J. E. Pearson, and W. K. Kwok, Physical Review B **96**, 075159 (2017).
[55] N. Wakeham, E. D. Bauer, M. Neupane, and F. Ronning, Physical Review B **93**, 205152 (2016).
[56] C. Guo, C. Cao, M. Smidman, F. Wu, Y. Zhang, F. Steglich, F.-C. Zhang, and H. Yuan, npj Quantum Materials **2**, 39 (2017).
[57] C. Zhang, C. Guo, H. Lu, X. Zhang, Z. Yuan, Z. Lin, J. Wang, and S. Jia, Physical Review B **92**, 041203 (2015).
[58] R. D. dos Reis, S. C. Wu, Y. Sun, M. O. Ajeesh, C. Shekhar, M. Schmidt, C. Felser, B. Yan, and M. Nicklas, Physical Review B **93**, 205102 (2016).

[59] L. Aggarwal, S. Gayen, S. Das, R. Kumar, V. Süß, C. Felser, C. Shekhar, and G. Sheet, Nature Communications **8**, 13974 (2017).
[60] H.-Z. Lu and S.-Q. Shen, Physical Review B **92**, 035203 (2015).
[61] C.-Z. Chen, J. Song, H. Jiang, Q.-f. Sun, Z. Wang, and X. C. Xie, Physical Review Letters **115**, 246603 (2015).
[62] D. T. Son and B. Z. Spivak, Physical Review B **88**, 104412 (2013).
[63] A. A. Burkov, Physical Review B **91**, 245157 (2015).
[64] M. Hirschberger, S. Kushwaha, Z. Wang, Q. Gibson, S. Liang, Carina A. Belvin, B. A. Bernevig, R. J. Cava, and N. P. Ong, Nature Materials **15**, 1161 (2016).
[65] H.-J. Kim, K.-S. Kim, J. F. Wang, M. Sasaki, N. Satoh, A. Ohnishi, M. Kitaura, M. Yang, and L. Li, Physical Review Letters **111**, 246603 (2013).
[66] F. Rullier-Albenque, D. Colson, and A. Forget, Physical Review B **88**, 045105 (2013).
[67] A. Juyal, A. Agarwal, and S. Mukhopadhyay, Physical Review Letters **120**, 096801 (2018).
[68] M. N. Baibich, J. M. Broto, A. Fert, F. N. Van Dau, F. Petroff, P. Etienne, G. Creuzet, A. Friederich, and J. Chazelas, Physical review letters **61**, 2472 (1988).
[69] D. Pesin and L. Balents, Nature Physics **6**, 376 (2010).
[70] H. Zhang, C.-X. Liu, X.-L. Qi, X. Dai, Z. Fang, and S.-C. Zhang, Nature Physics **5**, 438 (2009).
[71] Y. Xia *et al.*, Nature Physics **5**, 398 (2009).
[72] R. V. Gorbachev, F. V. Tikhonenko, A. S. Mayorov, D. W. Horsell, and A. K. Savchenko, Physical Review Letters **98**, 176805 (2007).
[73] Z. Zhu, A. Collaudin, B. Fauqué, W. Kang, and K. Behnia, Nature Physics **8**, 89 (2011).
[74] S.-Y. Xu *et al.*, Science **349**, 613 (2015).
[75] H. Weyl, Proceedings of the National Academy of Sciences of the United States of America **15**, 323 (1929).
[76] H. Weng, C. Fang, Z. Fang, B. A. Bernevig, and X. Dai, Physical Review X **5**, 011029 (2015).
[77] B. Q. Lv *et al.*, Physical Review X **5**, 031013 (2015).
[78] L. X. Yang *et al.*, Nature Physics **11**, 728 (2015).
[79] A. A. Burkov and L. Balents, Physical Review Letters **107**, 127205 (2011).
[80] N. W. Ashcroft and N. D. Mermin, *Solid state physics* 1976).
[81] Q. Shi, P. D. Martin, Q. A. Ebner, M. A. Zudov, L. N. Pfeiffer, and K. W. West, Physical Review B **89**, 201301 (2014).
[82] H. Kitazawa, T. Suzuki, M. Sera, I. Oguro, A. Yanase, A. Hasegawa, and T. Kasuya, Journal of Magnetism and Magnetic Materials **31-34**, 421 (1983).
[83] R. Settai, T. Goto, S. Sakatsume, Y. S. Kwon, T. Suzuki, and T. Kasuya, Physica B: Condensed Matter **186-188**, 176 (1993).
[84] A. Hasegawa, Journal of the Physical Society of Japan **54**, 677 (1985).
[85] L. R. Thoutam, Y. L. Wang, Z. L. Xiao, S. Das, A. Luican-Mayer, R. Divan, G. W. Crabtree, and W. K. Kwok, Physical Review Letters **115**, 046602 (2015).
[86] D. V. Khveshchenko, Physical Review Letters **87**, 206401 (2001).
[87] Y.-Y. Wang, Q.-H. Yu, P.-J. Guo, K. Liu, and T.-L. Xia, Physical Review B **94**, 041103 (2016).

[88] Y. Li, L. Li, J. Wang, T. Wang, X. Xu, C. Xi, C. Cao, and J. Dai, Physical Review B **94**, 121115 (2016).
[89] R. Singha, A. K. Pariari, B. Satpati, and P. Mandal, Proceedings of the National Academy of Sciences **114**, 2468 (2017).
[90] Y. L. Wang *et al.*, Physical Review B **92**, 180402 (2015).
[91] M. Zeng, C. Fang, G. Chang, Y.-A. Chen, T. Hsieh, A. Bansil, H. Lin, and L. Fu, arXiv preprint arXiv:1504.03492 (2015).
[92] F. Chen *et al.*, Physical Review B **91**, 205133 (2015).
[93] Z. J. Yue, X. L. Wang, and S. X. Dou, Applied Physics Letters **101**, 152107 (2012).
[94] A. Collaudin, B. Fauqué, Y. Fuseya, W. Kang, and K. Behnia, Physical Review X **5**, 021022 (2015).
[95] D. E. Soule, J. W. McClure, and L. B. Smith, Physical Review **134**, A453 (1964).
[96] B. Abeles and S. Meiboom, Physical Review **101**, 544 (1956).
[97] J. E. Aubrey, Journal of Physics F: Metal Physics **1**, 493 (1971).
[98] S.-M. Huang *et al.*, Nature Communications **6**, 7373 (2015).
[99] B. Q. Lv *et al.*, Nature Physics **11**, 724 (2015).
[100] S.-Y. Xu *et al.*, Nature Physics **11**, 748 (2015).
[101] H. Inoue, A. Gyenis, Z. Wang, J. Li, S. W. Oh, S. Jiang, N. Ni, B. A. Bernevig, and A. Yazdani, Science **351**, 1184 (2016).
[102] G. Chang *et al.*, Physical Review Letters **116**, 066601 (2016).
[103] S.-Y. Xu *et al.*, Physical Review Letters **116**, 096801 (2016).
[104] V. P. J. Jacobs, P. Betzios, U. Gürsoy, and H. T. C. Stoof, Physical Review B **93**, 195104 (2016).
[105] X. Dai, H.-Z. Lu, S.-Q. Shen, and H. Yao, Physical Review B **93**, 161110 (2016).
[106] Y. Sun, Y. Zhang, C. Felser, and B. Yan, Physical Review Letters **117**, 146403 (2016).
[107] Y. Zhou *et al.*, Physical Review Letters **117**, 146402 (2016).
[108] S. Thomas, D. J. Kim, S. B. Chung, T. Grant, Z. Fisk, and J. Xia, Physical Review B **94**, 205114 (2016).
[109] H.-T. He, G. Wang, T. Zhang, I.-K. Sou, G. K. L. Wong, J.-N. Wang, H.-Z. Lu, S.-Q. Shen, and F.-C. Zhang, Physical Review Letters **106**, 166805 (2011).
[110] H.-Z. Lu, J. Shi, and S.-Q. Shen, Physical Review Letters **107**, 076801 (2011).
[111] A. A. Taskin, S. Sasaki, K. Segawa, and Y. Ando, Physical Review Letters **109**, 066803 (2012).
[112] H. Wang *et al.*, Science Bulletin **62**, 425 (2017).
[113] M. D. Bachmann *et al.*, Science Advances **3**, e1602983 (2017).
[114] E. V. Konenkova, D. Grundler, M. Morgenstern, and R. Wiesendanger, Technical Physics Letters **34**, 30 (2008).
[115] Y. Kopelevich, J. C. M. Pantoja, R. R. da Silva, and S. Moehlecke, Physical Review B **73**, 165128 (2006).
[116] Z. Li, G. Li, N. L. Wang, and J. L. Luo, Journal of Physics: Condensed Matter **20**, 235232 (2008).
[117] Z. J. Yue, X. L. Wang, and S. S. Yan, Applied Physics Letters **107**, 112101 (2015).
[118] C.-L. Zhang, Z. Yuan, Q.-D. Jiang, B. Tong, C. Zhang, X. C. Xie, and S. Jia, Physical Review B **95**, 085202 (2017).
[119] N. Kumar *et al.*, Nature Communications **8**, 1642 (2017).

[120] E. Forgan, Papers in physics **5**, 1 (2013).
[121] A. Sergeev and V. Mitin, Physical Review B **61**, 6041 (2000).
[122] M. Meissner and R. O. Pohl, *Phonon Scattering in Condensed Matter VII: Proceedings of the Seventh International Conference, Cornell University, Ithaca, New York, August 3–7, 1992* (Springer Science & Business Media, 1992), Vol. 112.
[123] Y. Luo, R. D. McDonald, P. F. S. Rosa, B. Scott, N. Wakeham, N. J. Ghimire, E. D. Bauer, J. D. Thompson, and F. Ronning, Scientific Reports **6**, 27294 (2016).
[124] F. Han *et al.*, Physical Review B **96**, 125112 (2017).
[125] J. Hu, T. F. Rosenbaum, and J. B. Betts, Physical Review Letters **95**, 186603 (2005).
[126] J. Hu, M. M. Parish, and T. F. Rosenbaum, Physical Review B **75**, 214203 (2007).
[127] X. Dai, Z. Z. Du, and H.-Z. Lu, Physical Review Letters **119**, 166601 (2017).
[128] A. V. Andreev and B. Z. Spivak, Physical Review Letters **120**, 026601 (2018).
[129] P. Goswami, J. H. Pixley, and S. Das Sarma, Physical Review B **92**, 075205 (2015).
[130] Y. Gao, S. A. Yang, and Q. Niu, Physical Review B **95**, 165135 (2017).
[131] S. Liang, J. Lin, S. Kushwaha, J. Xing, N. Ni, R. J. Cava, and N. P. Ong, Physical Review X **8**, 031002 (2018).
[132] Y. Wang *et al.*, Nature Communications **7**, 13142 (2016).
[133] R. D. d. Reis, M. O. Ajeesh, N. Kumar, F. Arnold, C. Shekhar, M. Naumann, M. Schmidt, M. Nicklas, and E. Hassinger, New Journal of Physics **18**, 085006 (2016).
[134] D. R. Yennie, Reviews of Modern Physics **59**, 781 (1987).
[135] T. Khouri, U. Zeitler, C. Reichl, W. Wegscheider, N. E. Hussey, S. Wiedmann, and J. C. Maan, Physical Review Letters **117**, 256601 (2016).
[136] M. M. Parish and P. B. Littlewood, Nature **426**, 162 (2003).
[137] L. G. Salmon and I. J. D'Haenens, Journal of Vacuum Science & Technology B: Microelectronics Processing and Phenomena **2**, 197 (1984).
[138] A. Narayanan *et al.*, Physical Review Letters **114**, 117201 (2015).
[139] P. S. Alekseev, A. P. Dmitriev, I. V. Gornyi, V. Y. Kachorovskii, B. N. Narozhny, M. Schütt, and M. Titov, Physical Review Letters **114**, 156601 (2015).
[140] J. C. W. Song, G. Refael, and P. A. Lee, Physical Review B **92**, 180204 (2015).
[141] S. Thirupathaiah *et al.*, Physical Review B **97**, 035133 (2018).
[142] J. Hu and T. F. Rosenbaum, Nature Materials **7**, 697 (2008).
[143] L. Fang *et al.*, Physical Review B **84**, 140504 (2011).
[144] R. Prozorov, M. Kończykowski, M. A. Tanatar, A. Thaler, S. L. Bud'ko, P. C. Canfield, V. Mishra, and P. J. Hirschfeld, Physical Review X **4**, 041032 (2014).